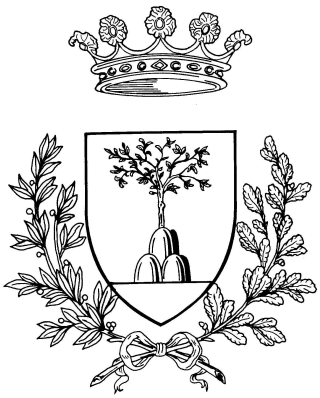

University of Ferrara

Department of Physics and Earth Science

Ph.D. in Physics

Modeling the Heavy-Ion Collisions with ECHO-QGP: a novel resource for the study of the QGP

Co-Advisor

Giuseppe Pagliara

Student

Valentina Rolando

Advisor

Alessandro Drago

2012-2015 – XXVII course

Coord. Prof. V.Guidi – FIS/04

University of Ferrara

Department of Physics and Earth Science

Ph.D. in Physics

Modeling the Heavy-Ion Collisions with ECHO-QGP: a novel resource for the study of the QGP

Co-Advisor

Giuseppe Pagliara

Student

Valentina Rolando

Advisor

Alessandro Drago

2012-2015 – XXVII course

Coord. Prof. V.Guidi – FIS/04

to my beloved family

Contents

Introduction **2**

0.1 Investigating the Quark Gluon Plasma phase 2

0.2 Historical overview and hydrodynamics achievements 4

0.3 ECHO-QGP 6

0.4 Outline 8

1 Relativistic Viscous Hydrodynamics **10**

1.1 Ideal Hydrodynamics 10

1.2 Dissipative Hydrodynamics 13

1.3 Hydrodynamics in ECHO-QGP 17

1.3.1 Formalism in ECHO-QGP 17

1.3.2 Implementation in ECHO-QGP 19

1.4 Validation of the ECHO-QGP 23

1.4.1 Mildly relativistic 1D shear flow 23

1.4.2 2D shock tubes 24

1.4.3 Boost invariant expansion along z-axis 25

1.4.4 2+1D tests with azimuthal symmetry 28

1.4.5 3+1D test in Minkowski 33

2 Numerical Set-Up, Features and results of ECHO-QGP **35**

2.1 Initial conditions 35

2.1.1 MC-Glauber initial conditions: a test case 38

2.2 Equation of State 40

2.3 Decoupling stage 43

2.3.1 Particle spectra in presence of dissipation 46

2.3.2 Particles spectra 47

2.4 Temperature and Eccentricity evolution 53

3 A study of vorticity formation in Heavy-ion collisions 62
3.1 Vorticities in relativistic hydrodynamics 63
3.1.1 The kinematical vorticity 63
3.1.2 The T-vorticity 64
3.1.3 The thermal vorticity 65
3.2 Vorticity in high energy nuclear collisions 67
3.3 Vorticities in ECHO-QGP: novel tests 70
3.3.1 T-vorticity for an ideal fluid 71
3.3.2 T-vorticity for a viscous fluid 72
3.4 Directed flow, angular momentum and thermal vorticity . . 73
3.5 Polarization 78
3.6 Plausibility of the initial conditions for the angular momentum 82

4 A perturbative approach to the hydrodynamics of heavy-ion collisions 84
4.1 Theoretical basis 85
4.2 Single mode 87
4.3 Higher harmonics 91
4.4 Application to realistic initial conditions 93

Conclusions and Outlook 97

Appendices 102

A Initial conditions for the angular momentum 104

Introduction

0.1 Investigating the Quark Gluon Plasma phase

Despite the solid theoretical basis of Quantum Cromo-Dynamics (QCD), the QCD phase diagram (see a sketch of it in fig. 1, and a complete review in ref [1]) is still not fully theoretically understood. This descends from the extreme complexity of the QCD calculations (strong coupling), finding an exact solution is hard enough to push physicists towards approximate methods, each one with a validity window restricted to particular areas of the phase diagram.

QCD features an important property: its coupling constant runs towards

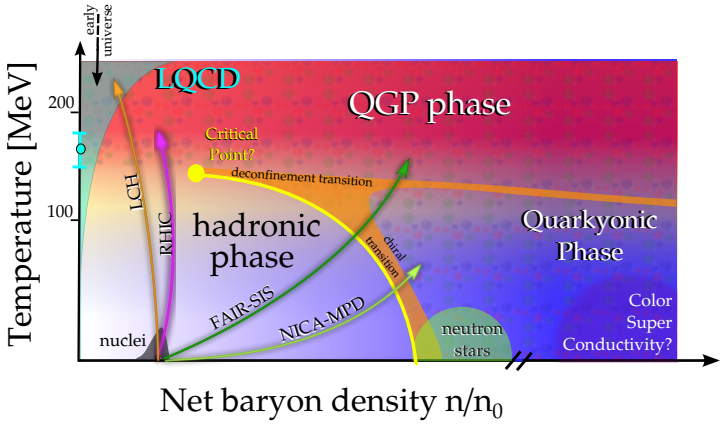

Figure 1: *Cartoon representation the QCD phase diagram. The strongly interacting quark matter is known to have different phases, due to the unique features of QCD. In this work we will mainly focus on the high temperature and low density region.*

smaller values with increasing energy scale, giving rise to what is called asymptotic freedom. This leads to the natural anticipation that QCD matter at high energy densities undergoes a phase transition from the hadronic phase, at low temperature and chemical potential, into a new state of matter with deconfined quarks and gluons. The latter is known as the Quark Gluon Plasma (QGP) phase.

The QGP phase is still experimentally widely unknown, and theoretically firm statements about its properties can be made only in limited cases – at finite temperature with small baryon density ($\mu_B \ll T$) and that at asymptotically high density ($\mu_B \gg \Lambda_{\rm QCD}$). In particular, standard Monte Carlo techniques used in lattice QCD calculations show that at vanishing baryon density, the transition between the hadron phase and the QGP phase is actually a crossover [2]. Due to the the sign problem posed by finite density, standard Monte Carlo techniques used in lattice QCD fail at finite values of the chemical potential, so lattice QCD is less effective to explore the QCD phase diagram moving away from vanishing baryon density (see for instance [3]). In such area of the phase diagram, we can find experimental results descending from ultra-relativistic heavy-ion collisions experiments, which artificially reproduced for the first time the QGP, which is considered to have filled the early universe up to times of $10^{-5} - 10^{-4}$ s (hence the name "little bangs" [4, 5]).

The investigations devoted to the modelization of the heavy-ion collisions, pushed by the experiments started a couple of decades ago and still ongoing, gave birth among other theories to the hydrodynamic modeling of the collision, whose purpose is to dynamically represent the phase transition (see a chronological summary in [6]).

Experiments, started a couple of decades ago and still ongoing, showed evidence of the presence of the QGP phase. Since the plasma evolves on a strong interaction time scale, the community was motivated to develop theoretical schemes to model the dynamics of the phase transition from the QGP to the hadronic phase. One of the most successful framework is the hydrodynamic approach to heavy-ion collisions.

0.2 Historical overview and hydrodynamics achievements

While the very first hint that the collision between heavy particles, like atomic nuclei, can be modeled exploiting collective theories like fluid-dynamics dates back to the 1950s [7], this approach really had a boost in the scientific community at the end of the 1970s. The main sources of the interest toward these models were the ongoing experiments, which covered a range of energy in the center of mass from a few hundred MeV (Berkeley LBNL) up to 5 GeV (AGS at BNL) and 17 GeV (SPS at CERN) per nucleon [8, 9]. Even if it was not obvious that a new state of matter had been obtained, the results of such fixed-target experiments showed the presence of collective behaviour, and in particular that the medium undergoes a collective expansion in the plane perpendicular to the beam [10]. The flat behaviour of the particle spectra around mid-rapidity led Bjorken [11] to propose the simplified model of a ultra-relativistic fluid expanding radially in a boost-invariant space. Even if this model failed to describe the transverse collective behaviour, it cast the basis of the hydrodynamic approach to heavy-ion collisions.

In particular, in the decades from 1980 to 2000, a lot of effort went into the development of codes that solved the equations of motions for a relativistic ideal fluid in one and two transverse directions (*e.g.* [12–14]), motivated by the experimental evidence of transverse flow [15, 16] and in particular of elliptic flow [17], which is an anisotropic emission around the beam direction due to the difference of pressure gradients along the axes of the transverse plane.

Applying a collective theory such as ideal hydrodynamics in a regime of strong coupled interactions was something daring, but it turned out that numerical models could qualitatively predict the behaviour of all low transverse momentum (i.e. *soft*) observables produced in heavy ions collisions. The quantitative comparison among the theory and the data though, showed a sharp discrepancy: although the particle spectrum was correctly reproduced in the low transverse momentum region, the elliptic flow was overestimated by about 50% [18]. In the same years, microscopic approaches based on a kinetic description of systems of scattering hadrons were also developed and correctly predicted the elliptic flow [19]; but the same kinetic approach, taken alone, failed in the subsequent years at higher energies [20, 21].

The turn around in the field was finally given in 2000, by the Relativistic

Heavy Ion Collider (RHIC) at BNL, that allowed to study collisions of gold or lead nuclei up to energies in the center of mass of $\sqrt{s_{\mathrm{NN}}} = 130$ GeV and $\sqrt{s_{\mathrm{NN}}} = 200$ GeV per nucleon. These experiments brought conclusive evidence of the expected new phase state of the matter, called Quark Gluon Plasma (QGP), in which hadrons melt into deconfined colored degrees of freedom, quarks and gluons, predicted by QCD. This evidence also involved a huge drop in the net baryon distribution as a function of the rapidity in the most central collisions (see [22] and figure 3 therein), showing a medium transparent to nuclear collision, which reflects the presence of the hot medium together with the absence of nuclei fragments and indicating the creation of the QGP (this process is also known as baryon stopping). To further corroborate the evidence, the so called *jet quenching* was observed for the first time, a process that involves the suppression of the momentum of mini jets of hadrons passing through the bulk.
For the first time hydrodynamics could be quantitatively compared to experiments [23], and this induced many in the scientific community to claim that the QGP is a "nearly perfect fluid": due to the asymptotic freedom in QCD and the color Debye screening, the QGP was expected to behave like gas and produce no anisotropy in the momentum flow . Instead, given the agreement with hydrodynamics, the idea of a strongly coupled plasma flowing as a perfect liquid spread among the community [24–26].

In the next years the applicability of hydrodynamics was questioned, and in fact it appeared that the initial success of ideal fluid dynamics was in reality tainted by the use of a non-realistic equation of state for the fireball (see [27]) together with a treatment of its chemical composition which did not properly reflects its late hadronic stage [28].

In particular some works [29–32] restricted the region in which hydrodynamics is effective to the (early) QGP phase, in which the fluid has undergone low dissipative effects. Since the late hadronic stage is better represented by microscopic theories, various hybrid approaches were proposed, in which the description switched from hydrodynamic to kinetic. The presence of dissipative effects draw anyway the attention to the possibility of a viscous QGP phase description [31, 33–36]. In fact with experiments giving more and more refined results it became evident the need of a (although small) viscosity even in the most central collisions. Further studies, motivated by the need to give a precise and quantitative description of the QGP phase, brought to the community more and more accurate hydrodynamic numerical codes, testing their ability to handle extreme regimes, extending the model to a full (3+1)-D space and including

viscous corrections to higher orders [37–42].

0.3 ECHO-QGP

In spite of the huge progress due to the new experimental discoveries and theoretical advances made over the past decades, several open questions regarding the nature, structure and origin of the QGP are still debated. It has still to be understood what is the smallest size and density for a system of QCD matter to conserve the liquid behavior [43]; what are the transport properties of the QGP and how they are affected by its chemical composition; how its collective properties emerge from the interactions among the individual quarks and gluons and what is the precise nature of the initial state; how it reaches in such a short time an approximate local thermal equilibrium and all the same undergoes such a rapid expansion, whether the applicability of hydrodynamics in a strongly coupled regime is meaningful ... and the open questions are so many that deserve an entire work just to be discussed [44]. Even though the effort towards the understanding of the QGP phase diagram involves the worldwide physic community, and the hydrodynamics is a very well know approach to investigate it, we are still lacking a reliable and widespread resource, accessible to any scientist wanting to approach the open questions. The ECHO-QGP was firstly formed with the goal to provide an answer to this problem.

ECHO-QGP lies among the most refined numerical hydrodynamic codes to describe the QGP phase. It has been built on top of the *Eulerian Conservative High Order* code for General Relativistic Magneto-Hydro-Dynamics (GRMHD) [45], originally developed and widely used for high-energy astrophysical applications. ECHO-QGP shares with the original code the conservative (shock-capturing) approach, needed to treat shocks and other hydrodynamical discontinuities that invariably arise due to the intrinsic nonlinear nature of the equations, and the high accuracy methods for time integration, and spatial interpolation and reconstruction routines, needed to capture small-scale fluid features and turbulence. With respect to the original hydrodynamical version of the code, where only the ideal case was treated, ECHO-QGP fully embeds second-order dissipative effects, treated within the Israel-Stewart-Müller theory frame (treated in more detail in chapter 1).

The developing team of ECHO-QGP involved several researchers from

three Italian Universities: Florence, Ferrara and Turin. In four years, this team has brought ECHO-QGP to come known in the international community as peer with other accomplished hydrodynamic codes[1] ([37–42,47–66]), creating a state-of-the-art tool in the heavy-ion collisions physics field and it is also suitable for public distribution.
A 3+1D public code is still missing in the physics community. Few public codes are available [13, 14, 34–36], but none of them performs full 3+1D simulations within a viscous theory. We wold like to remark that the viscosity, and in particular its magnitude, is still a matter of debate, while it has been proved to be an essential component of the description. Moreover, the full dimensionality of the simulation is also an essential component: hydrodynamic needs complementary modeling concerning the initial conditions and the particle production, which can be constrained by the use of the experimental observables. For instance, within a 2+1D simulation we could not study the particle rapidity spectra or the odd harmonics of the flow as functions of the rapidity.

Adapting a hydrodynamics code born for astrophysical applications to a code for the modeling of heavy-ion collisions is a demanding task. The working plan was distributed as follows: Florence's group was in charge of the implementation of the Israel-Stewart formalism in the hydrodynamic evolution; Turin's group worked on the initial conditions and the Equation of state; myself with the group of Ferrara were involved in the implementation of the decoupling process, i.e. the only stage of the calculation that produces results to be compared with experiments. The physical observables obviously depend on the initial conditions and on the hydrodynamic fields, therefore I had to actively collaborate with the other two groups during the development and the test of the code. Concerning the applications of ECHO-QGP to physics problems, I calculated the directed flow and the particle polarization in presence of vorticity during the hydrodynamic evolution. Finally, I collaborated with a group of the theoretical division of CERN, for the study of the evolution of initial state fluctuations through a perturbative method.

[1] see [46] for a 2012 review of the features of each hydro code

0.4 Outline

This thesis is structured as follows: in chapter 1 the reader can find an overview of the hydrodynamic description, together with the method used to implement it in ECHO-QGP. In the same chapter there is a collection of tests, proving the suitability of ECHO-QGP to model heavy-ion collisions along with its accuracy. In chapter 2, we describe the setup used for ECHO-QGP and we explain in more detail how to construct the initial state and how the final observables are computed. In chapter 3 ECHO-QGP is exploited to study the vorticity formation in high energy nuclear collisions: we will show how thermal vorticity affects the directed flow and its relation with the final state polarization. In particular, we will discuss the detectability of the polarization of the Λ. In chapter 4 we employ a perturbative approach to the initial state to study the fluid dynamic propagation of fluctuations. In the last chapter we draw conlusions about the work performed with ECHO-QGP and we give an outlook about future perspectives.

1

Relativistic Viscous Hydrodynamics

Hydrodynamics is a theoretical framework which allows the collective description of a strongly interacting many-body system, through thermodynamic variables defined locally, masking all the microscopic details. Provided that the initial expansion timescale is sufficiently long compared to the transport mean free path, we can in fact exploit thermodynamic concepts like temperature and pressure to describe the system. Hydrodynamics applicability has been extensively discussed (see for instance [67, 68]) but this theoretical frame is currently one of the best dynamic tools to reproduce the experimental observables.

As shown in the cartoon in fig. 1.1, the region in which we apply hydrodynamics is after a pre-equilibrium phase ($\sim$ 1 fm/c), in which the medium achieves local thermal equilibrium, and before the dissipative behavior becomes dominant (and hence better described by a kinetic approach).

In this chapter, we will quickly review the hydrodynamic theory before showing how it is implemented and how it performs in ECHO-QGP.

1.1 Ideal Hydrodynamics

The definition of "Ideal Hydrodynamics" is currently accepted as a synonym of non-viscous. It is anyway important to remark that ideal hydrodynamics does not necessarily imply the global thermodynamic equilibrium: when

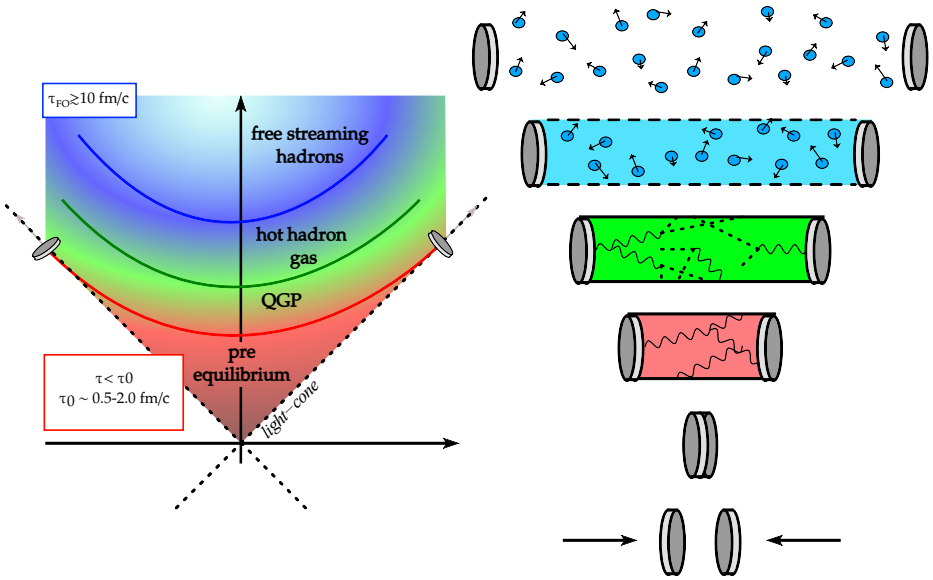

Figure 1.1: *Cartoon representation of a Heavy-ion collision. The origin of the axis represents the instant of the collision, assuming that the nuclei are moving at the speed of light along the light-cone, where the remnants of the shattered nuclei continue to move. The medium is believed to thermalize in a time of the order of 1 fm/c. The average life of the fireball is of about 10 fm/c, and in such interval hydrodynamic is exploited to model its evolution. When the scattering rate of particles is of the order of the expansion rate, hydrodynamics ceases to be applicable.*

all transport coefficients are vanishing, there can still be the presence of thermodynamic force with no entropy production.

The hydrodynamic flow (u^μ) is denoted as a four velocity with its normalizing condition, which defines the fluid Lorentz factor ($\gamma \equiv u^0$)

$$u^\mu \equiv \gamma(1, v^i) \quad u_\mu u^\mu = -1 \quad \gamma = (1 - g_{ij} v^i v^j)^{-1/2} \quad v^i \equiv u^i/\gamma \tag{1.1}$$

In ideal hydrodynamics, the system is well and fully described by its energy momentum tensor and the conserved charge current

$$N_0^\mu = n_0 u^\mu \tag{1.2}$$
$$T_0^{\mu\nu} = e_0 u^\mu u^\nu + \Delta^{\mu\nu} P_0 \tag{1.3}$$

where the orthogonal projector operator has been introduced, written as:

$$\Delta^{\mu\nu} \equiv g^{\mu\nu} + u^\mu u^\nu, \tag{1.4}$$

and it respects the orthogonality relation: $\Delta^{\mu\nu} u_\mu = 0$. The local equilibrium thermodynamic quantities are defined by the relations

$$e_0 = u_\mu u_\nu T_0^{\mu\nu} \qquad \text{energy density} \tag{1.5}$$
$$P_0 = \frac{1}{3} \Delta_{\mu\nu} T_0^{\mu\nu} \qquad \text{hydrostatic pressure} \tag{1.6}$$
$$n_0 = -u_\mu N_0^\mu \qquad \text{conserved charge density} \tag{1.7}$$

In case of multiple conserved charges the equation 1.2 must be valid for each conserved charge n_0^i.

The conservation of the energy-momentum tensor and conserved current are written as:

$$d_\mu N_0^\mu = 0, \tag{1.8}$$
$$d_\mu T_0^{\mu\nu} = 0. \tag{1.9}$$

where the covariant derivative (d_μ) could be decomposed along its temporal direction $D \equiv u^\alpha d_\alpha$, and along its spatial direction $\nabla_\mu \equiv \Delta_\mu^\alpha d_\alpha$.

$$d_\mu = -u_\mu D + \nabla_\mu, \tag{1.10}$$

Equations 1.8-1.9 provide a set of 4+1 independent equations (or 4+N for N multiple conserved currents) with 5+1 (5+N) independent variables namely: n_0, e_0, P_0, u^μ. The set given by the conservation laws alone does

not give a complete description, for this reason an Equation of State (EoS) is usually adopted to close the system, i.e. a relation $P_0 = \mathcal{P}(e_0, n_0)$.

1.2 Dissipative Hydrodynamics

The parabolic character of the equation of heat has been recognized as a fallacy due to the unsuitability of conventional thermodynamics in describing transient regimes. In fact, in the Navier-Stokes approach the dissipative quantities react instantaneously to the thermodynamic forces, but the instantaneous propagation implies acausality, for which reason a consistent generalization of the Navier Stokes equations in a relativistic frame is forbidden. Along with the causality violation, the first-order theory has stability problems, having exponentially growing modes when the perturbation from global equilibrium is infinitesimally small (see for instance [69]).

Relaxing the instantaneous propagation assumption by introducing characteristic time scales, which regulate the response of the dissipative quantities to the corresponding thermodynamic forces, causality and stability issues are removed and the theory becomes stable and causal. While the value and the importance of the higher order transport coefficients is still a hot topic ([70, 71]) historically, the first second-order theory approach for viscous hydrodynamics was proposed by Israel and Stewart [72].

In 1949 Grad proposes a new theoretical approach in the framework of the classical kinetic theory, appliyng a method of moments (now known as Grad-14 moments approximation) and obtaining the set of classical dissipative fluid-dynamics equations [73]. In 1967 [74] Müller presents a phenomenological derivation of the non relativistic thermodynamics, including second order terms in heat flow and viscosity conventionally neglected, which is consisitent with Grad's kinetic approach. In 1970 Stewart [75] elaborates the relativistic extension of the Grad's approximation, along with others (Anderson and Stewart [76], Marle [77], Kranys [78–81]). In 1976 Israel extends the phenomenological approach to the relativistic case. In 1987 the comprehensive work of Israel and Stewart [72] draws together the collection of all kinetic and phenomenological approaches, providing the explicit form of the transport coefficients in the generalized transport equations for a relativistic quantum gas.

In this work a second-order Israel-Stewart treatment has been used and implemented in ECHO-QGP. The energy-momentum tensor and the conserved currents are decomposed as

$$N^{\mu} = nu^{\mu} + V^{\mu}, \tag{1.11}$$

$$T^{\mu\nu} = eu^{\mu}u^{\nu} + (P + \Pi)\Delta^{\mu\nu} + \pi^{\mu\nu} + w^{\mu}u^{\nu} + w^{\nu}u^{\mu}, \tag{1.12}$$

where the viscous contributions to the energy momentum tensor are respectively the shear ($\pi^{\mu\nu}$) and bulk part Π of the viscous stress tensor. The following definitions do apply:

$$\text{conserved charge density} \qquad n = u_{\mu}N^{\mu} \tag{1.13}$$

$$\text{particle diffusion flux} \qquad V^{\mu} = \Delta^{\mu}_{\alpha}N^{\alpha} \tag{1.14}$$

$$\text{energy density} \qquad e = u_{\mu}u_{\nu}T^{\mu\nu} \tag{1.15}$$

$$\text{isotropic pressure} \qquad P + \Pi = \frac{1}{3}\Delta_{\mu\nu}T^{\mu\nu} \tag{1.16}$$

$$\text{energy-momentum flow orthogonal to } u^{\mu} \qquad w^{\mu} = -\Delta^{\mu}_{\alpha}T^{\alpha\beta}u_{\beta} \tag{1.17}$$

where the shear component of the stress tensor is defined as

$$\pi^{\mu\nu} = [\tfrac{1}{2}(\Delta^{\mu}_{\alpha}\Delta^{\nu}_{\beta} + \Delta^{\mu}_{\beta}\Delta^{\nu}_{\alpha}) - \tfrac{1}{3}\Delta^{\mu\nu}\Delta_{\alpha\beta}]T^{\alpha\beta} \tag{1.18}$$

and satisfies the orthogonality and traceless requirements:

$$\pi^{\mu\nu}u_{\nu} = 0 \tag{1.19}$$

$$\pi^{\mu}_{\mu} = 0. \tag{1.20}$$

When the dissipative quantities vanish ($V^{\mu} = w^{\mu} = \pi^{\mu\nu} = \Pi = 0$), we recover the ideal decompositions $N^{\mu}_0 = n_0u^{\mu}$ and $T^{\mu\nu}_0 = e_0u^{\mu}u^{\nu} + P_0\Delta^{\mu\nu}$. To guarantee the thermodynamic stability of the system, in the local rest frame of the fluid (LRF), the quantities n and e are fixed to their equilibrium values by utilizing the Landau matching conditions ($n = n_0$, $e = e_0$). The pressure is recovered using an appropriate equation of state (EoS) as $P = \mathcal{P}(e, n) = \frac{1}{3}\Delta_{\mu\nu}T^{\mu\nu}_0$.

When treating the theory up to orders higher than the first, one loses the equivalence between the four-velocity parallel to N^{μ} and the normalized timelike eigenvector of $T^{\mu\nu}$, which were equivalent in the first order theory. In principle any frame that arbitrarily deviates from the equilibrium frame is a valid choice for the hydrodynamic flow, since the only condition that has to be fulfilled is that the dissipative components of the conserved

quantities are small compared to the equilibrium ones. The two most common possibilities for the selection of the frame are the Landau frame in which there is no net energy-momentum flow ($w^\mu = 0$); or the Eckart frame in which the charge dissipative flow vanishes ($V^\mu = 0$). The former choice is the one we adopted in our works, for several reasons. The QGP in High Energy collisions (RHIC, LHC) is created with an extremely small baryon density, letting the equation of state assume the form $P = \mathcal{P}(e)$. That is the very case of many hydrodynamic studies and the Landau frame is preferred because the particle frame cannot be defined for the systems with vanishing conserved currents, while the energy frame is always definable. The same argument applies when there are multiple conserved currents: there is no further simplification if other currents are still present, when choosing one of them to vanish.

For vanishing baryon densities we have only one quantity left to describe the dynamics of the fluid and the equation for N^μ becomes redundant in the conservation laws:

$$d_\mu N^\mu = 0, \tag{1.21}$$

$$d_\mu T^{\mu\nu} = 0. \tag{1.22}$$

It is now convenient to decompose the conservation law of eq.(1.22) along u^μ and orthogonal to u^μ, in order to derive the energy and momentum equations, respectively. In order to do so, one can take advantage of some useful kinematic quantities. The covariant derivative of the fluid velocity can be decomposed in its *irreducible tensorial parts*, respectively the **transverse**, **traceless**, and **symmetric** component $\sigma_{\mu\nu}$, the **transverse**, **traceless**, and **anti-symmetric** component $\omega_{\mu\nu}$ and the **scalar** component θ:

$$d_\mu u_\nu = \sigma_{\mu\nu} + \omega_{\mu\nu} - u_\mu D u_\nu + \tfrac{1}{3}\Delta_{\mu\nu}\theta, \tag{1.23}$$

where the following definitions apply:

$$\text{shear tensor} \quad \sigma_{\mu\nu} = \tfrac{1}{2}(\nabla_\mu u_\nu + \nabla_\nu u_\mu) - \tfrac{1}{3}\Delta_{\mu\nu}\theta, \tag{1.24}$$

$$= \tfrac{1}{2}(d_\mu u_\nu + d_\nu u_\mu) + \tfrac{1}{2}(u_\mu D u_\nu + u_\nu D u_\mu) - \tfrac{1}{3}\Delta_{\mu\nu}\theta,$$

$$\text{vorticity tensor} \quad \omega_{\mu\nu} = \tfrac{1}{2}(\nabla_\mu u_\nu - \nabla_\nu u_\mu) \tag{1.25}$$

$$= \tfrac{1}{2}(d_\mu u_\nu - d_\nu u_\mu) + \tfrac{1}{2}(u_\mu D u_\nu - u_\nu D u_\mu),$$

$$\text{expansion scalar} \quad \theta = \nabla_\mu u^\mu = d_\mu u^\mu. \tag{1.26}$$

With the above decompositions, the relativistic energy and momentum equations in 1.22 can be written as

$$De + (e + P + \Pi)\theta + \pi^{\mu\nu}\sigma_{\mu\nu} = 0, \tag{1.27}$$

$$(e + P + \Pi)Du_\nu + \nabla_\nu(P + \Pi) + \Delta^\beta_\nu \nabla_\alpha \pi^\alpha_\beta + Du^\mu \pi_{\mu\nu} = 0, \tag{1.28}$$

where the latter is clearly orthogonal to u_ν.

Matching fluid dynamics to the underlying microscopic theory (i.e. in the case of dilute gases the Boltzmann equation) is done in the Israel Stewart formalism, through Grad's method of moments, truncating the expansion at second order in momentum. The coefficients of the truncated expansion can then be uniquely related to the fluid dynamic fields using a matching procedure. The bulk and shear viscous parts of stress tensor, including terms up to second-order in the velocity gradients, satisfy the following evolution equations:

$$D\Pi = -\tfrac{1}{\tau_\Pi}(\Pi + \zeta\theta) - \tfrac{4}{3}\Pi\theta, \tag{1.29}$$

$$\Delta^\mu_\alpha \Delta^\nu_\beta D\pi^{\alpha\beta} = -\tfrac{1}{\tau_\pi}(\pi^{\mu\nu} + 2\eta\sigma^{\mu\nu}) - \tfrac{4}{3}\pi^{\mu\nu}\theta - \lambda(\pi^{\mu\lambda}\omega^\nu_\lambda + \pi^{\nu\lambda}\omega^\mu_\lambda) \tag{1.30}$$

(for derivation see for instance [82]). In this analysis, terms that are quadratic in Π, $\pi^{\mu\nu}$ and $\omega^{\mu\nu}$ are neglected. To obtain the solution of the above evolution equations we shall need to specify the transport coefficients η, ζ, the shear and bulk relaxation times τ_π, τ_Π, and the other second-order transport parameter, $\lambda \equiv \lambda_2/\eta$ [82]. The parameter λ_2 is known for the weakly coupled, as well strongly coupled $\mathcal{N} = 4$, Super Yang Mills theories [82], but not for the strongly coupled QCD. The vorticity contribution in Eq. (1.30), which contains λ, for the purposes of this chapter will be mostly ignored by letting $\lambda = 0$, whereas in specific runs it will be chosen to be 1 as in [83].

Writing explicitly the orthogonal projector as in (1.4) and using orthogonality condition $u_\mu \pi^{\mu\nu} = 0$, we can rewrite Eq. (1.30) as

$$D\pi^{\mu\nu} = -\tfrac{1}{\tau_\pi}(\pi^{\mu\nu} + 2\eta\sigma^{\mu\nu}) - \tfrac{4}{3}\pi^{\mu\nu}\theta + \mathcal{I}_1^{\mu\nu} + \mathcal{I}_2^{\mu\nu}, \tag{1.31}$$

where the contributions deriving from the orthogonal projection ($\mathcal{I}_1^{\mu\nu}$) have been kept apart from the vorticity contribution term ($\mathcal{I}_2^{\mu\nu}$). They are defined as follows:

$$\mathcal{I}_1^{\mu\nu} = (\pi^{\lambda\mu}u^\nu + \pi^{\lambda\nu}u^\mu)Du_\lambda, \tag{1.32}$$

$$\mathcal{I}_2^{\mu\nu} = -\lambda(\pi^{\mu\lambda}\omega^\nu_\lambda + \pi^{\nu\lambda}\omega^\mu_\lambda). \tag{1.33}$$

1.3 Hydrodynamics in ECHO-QGP

In this section the reader can find a quick summary on how the implementation of the conservation laws (1.21, 1.22) within the ECHO-QGP code.

1.3.1 Formalism in ECHO-QGP

The conservation laws and the evolution equations for the components of Π and $\pi^{\mu\nu}$ must be rewritten in a form suitable for numerical computations: a conservative balance law; in which conserved quantities ($\mathbf{U}$), fluxes ($\mathbf{F}_i$) and source terms ($\mathbf{S}$) are present:

$$\partial_0 \mathbf{U} + \nabla_i \mathbf{F}^i = \mathbf{S} \tag{1.34}$$

In the dissipative case, the system is comprehensive of 13 scalar equations (with the addistion of the equation of state).

Even if the formal setup emplys the Landau frame, it is numerically convenient to evolve the continuity equation in the limit $V^\mu = 0$, in order to improve the stability. Equation 1.21 is rewritten as:

$$Dn + n\theta = 0, \tag{1.35}$$

where the charge density n must be interpreted just as a tracer responding to the evolution of the fluid velocity through the expansion scalar θ. We manipulate the equation to obtain the desired form (1.34)

$$d_\mu N^\mu = |g|^{-\frac{1}{2}} \partial_\mu (|g|^{\frac{1}{2}} N^\mu) = 0, \tag{1.36}$$

or also

$$\partial_0 (|g|^{\frac{1}{2}} N^0) + \partial_k (|g|^{\frac{1}{2}} N^k) = 0. \tag{1.37}$$

Again, it is necessary to repeat the same procedure to the conservation of the energy-momentum tensor components 1.22

$$d_\mu T^\mu_\nu = |g|^{-\frac{1}{2}} \partial_\mu (|g|^{\frac{1}{2}} T^\mu_\nu) - \Gamma^\mu_{\nu\lambda} T^\lambda_\mu = 0, \tag{1.38}$$

where the relation $\Gamma^\mu_{\mu\lambda} = |g|^{-\frac{1}{2}} \partial_\lambda |g|^{\frac{1}{2}}$, has been employed, in which g is the determinant of the metric tensor. It is possible to further rewrite this equation making use of the symmetry properties of the energy-momentum

tensor, to obtain:

$$\partial_0(|g|^{\frac{1}{2}}T^0_\nu) + \partial_k(|g|^{\frac{1}{2}}T^k_\nu) = |g|^{\frac{1}{2}}\Gamma^\mu_{\nu\lambda}T^\lambda_\mu = |g|^{\frac{1}{2}}\frac{1}{2}T^{\lambda\mu}\partial_\nu g_{\lambda\mu}, \tag{1.39}$$

The adjustment of the evolution laws for the stress tensor component is also needed, to obtain the desired form of balance laws. The previous $d_\mu N^\mu = 0$ relation is now useful in order to rewrite the timelike components of the comoving derivative ($D \equiv u^\mu d_\mu$), multiplying the equations for the evolution of $\pi^{\mu\nu}$ and Π (1.29 and 1.30) by the tracer n, one obtains:

$$\partial_0(|g|^{\frac{1}{2}}N^0\Pi) + \partial_k(|g|^{\frac{1}{2}}N^k\Pi) = |g|^{\frac{1}{2}}n\left[-\tfrac{1}{\tau_\Pi}(\Pi + \zeta\theta) - \tfrac{4}{3}\Pi\theta\right] \tag{1.40}$$

for the evolution of the bulk component of the stress tensor; and

$$\begin{aligned}&\partial_0(|g|^{\frac{1}{2}}N^0\pi^{\mu\nu}) + \partial_k(|g|^{\frac{1}{2}}N^k\pi^{\mu\nu}) = \\ &|g|^{\frac{1}{2}}n\left[-\tfrac{1}{\tau_\pi}(\pi^{\mu\nu} + 2\eta\sigma^{\mu\nu}) - \tfrac{4}{3}\pi^{\mu\nu}\theta + \mathcal{I}_0^{\mu\nu} + \mathcal{I}_1^{\mu\nu} + \mathcal{I}_2^{\mu\nu}\right],\end{aligned} \tag{1.41}$$

for the evolution of the shear components of the stress tensor. The source terms have been kept non explicit, since they are different for different coordinates systems, but the term $\mathcal{I}_0$ has been isolated, since it clearly vanishes in Minkowski coordinates:

$$\mathcal{I}_0^{\mu\nu} = -u^\alpha(\Gamma^\mu_{\lambda\alpha}\pi^{\lambda\nu} + \Gamma^\nu_{\lambda\alpha}\pi^{\mu\lambda}) \tag{1.42}$$

On the other side, in Bjorken coordinates the non-vanishing $\mathcal{I}_0^{\mu\nu}$ terms are

$$\mathcal{I}_0^{x\eta} = -(u^\tau\pi^{x\eta} + u^\eta\pi^{\tau x})/\tau, \tag{1.43}$$
$$\mathcal{I}_0^{y\eta} = -(u^\tau\pi^{y\eta} + u^\eta\pi^{\tau y})/\tau, \tag{1.44}$$
$$\mathcal{I}_0^{\eta\eta} = -2(u^\tau\pi^{\eta\eta} + u^\eta\pi^{\tau\eta})/\tau, \tag{1.45}$$

while $\mathcal{I}_1^{\mu\nu}$ and $\mathcal{I}_2^{\mu\nu}$ are defined in the usual way.

The technique of introducing the conserved number current as a tracer is exploited in a similar way within a recent code for (2+1)-D Lagrangian hydrodynamics [84] to solve the evolution equation of the bulk viscous pressure Π.

Due to the orthogonality condition, only 6 out of 10 components of the viscous stress tensor are independent. ECHO-QGP can evolve the 5 spatial component π^{ij}, or evolve all and only its 6 spatial independent components. The latter choice is the one adopted in the present work, and it generates a system which can be arranged in matrix form to reflect the structure of

1.34, with:
conservative variables

$$\mathbf{U} = |g|^{\frac{1}{2}} \begin{pmatrix} N \equiv N^0 \\ S_i \equiv T^0_i \\ E \equiv -T^0_0 \\ N\Pi \\ N\pi^{ij} \end{pmatrix}, \tag{1.46}$$

fluxes

$$\mathbf{F}^k = |g|^{\frac{1}{2}} \begin{pmatrix} N^k \\ T^k_i \\ -T^k_0 \\ N^k\Pi \\ N^k\pi^{ij} \end{pmatrix}, \tag{1.47}$$

sources

$$\mathbf{S} = |g|^{\frac{1}{2}} \begin{pmatrix} 0 \\ \frac{1}{2}T^{\mu\nu}\partial_i g_{\mu\nu} \\ -\frac{1}{2}T^{\mu\nu}\partial_0 g_{\mu\nu} \\ n[-\frac{1}{\tau_\pi}(\Pi + \zeta\theta) - \frac{4}{3}\Pi\theta] \\ n[-\frac{1}{\tau_\pi}(\pi^{ij} + 2\eta\sigma^{ij}) - \frac{4}{3}\pi^{ij}\theta + \mathcal{I}^{ij}_0 + \mathcal{I}^{ij}_1 + \mathcal{I}^{ij}_2] \end{pmatrix} \tag{1.48}$$

The above Eqs. 1.46-1.47 together with the eq. 1.34 represent the set of ECHO-QGP equations in the most general form, since ECHO-QGP can work both in Minkowski and Bjorken coordinates.

1.3.2 Implementation in ECHO-QGP

In this section, the reader can find a very brief summary of the numerical techniques used in ECHO-QGP. The name *conserved variables* is intended for the set of quantities $\mathbf{U}$, explicit in 1.46 entering the equation 1.34, while the expression *primitive variables* is used to refer to the corresponding physically meaningful quantities, namely: the fluid velocity, the local energy density, the independent components of the shear stress tensor and the charge density ($\mathbf{P} = \{n, v^i, P, \Pi, \pi^{ij}\}$).

The ECHO-QGP [85] code has been built upon the original ECHO scheme [86] which was, and still is, devoted to relativistic hydrodynamics and MHD (in any GR metric, even time dependent like for Bjorken coor-

dinates) for astrophysics purposes. Therefore, ECHO-QGP shares with ECHO the finite-difference discretization, the conservative approach, and the shock-capturing techniques.

- The spatial grid is discretized along all the directions of interest as a $N_x \times N_y \times N_z$ set of cells (N_η in Bjorken coordinates). Lower dimensionality runs are always admitted, for example, 2-D tests with boost invariance in Bjorken coordinates are performed by choosing $N_\eta = 1$.

- The physical *primitive variables* set ($\mathbf{P} = \{n, v^i, P, \Pi, \pi^{ij}\}$) is initialized for $t = 0$ (or for a chosen $\tau = \tau_0$ in Bjorken coordinates) defining the value of each variable at every cell center.

- During the hydrodynamic evolution, the conservative variables $\mathbf{U}$ and fluxes $\mathbf{F}$ are calculated at cell interfaces. At first, the corresponding values of the primitive variables are calculated at cell interfaces too. For each "spatial direction", the primitive variables calculated at the interfaces (*i.e. left*: $\mathbf{P}_L$ and *right*: $\mathbf{P}_R$) are used to retrieve the value at the cell centre.

- For each component and at each intercell, upwind fluxes $\hat{F}^k$ (along direction k) are worked out using the so-called HLL two-state formula [87] as

$$\hat{F}^k = \frac{a_+^k F^k(\mathbf{P}_L) + a_-^k F^k(\mathbf{P}_R) - a_+^k a_-^k [U(\mathbf{P}_R) - U(\mathbf{P}_L)]}{a_+^k + a_-^k}, \quad (1.49)$$

  where the coefficients $a_\pm^k$ are calculated as:

$$a_\pm^k = \max\{0, \pm\lambda_\pm^k(\mathbf{P}_L), \pm\lambda_\pm^k(\mathbf{P}_R)\}, \quad (1.50)$$

  and the local fastest characteristic speeds associated to the Jacobian $\partial\mathbf{F}^k/\partial\mathbf{U}$, relative to the direction k is calculated as:

$$\lambda_\pm^k = \frac{(1-c_s^2)v^k \pm \sqrt{c_s^2(1-v^2)[(1-v^2c_s^2)g^{kk} - (1-c_s^2){v^k}^2]}}{1-v^2c_s^2}. \quad (1.51)$$

  Notice that eq. (1.51), provides an approximated solution to the local Riemann problem. The sound speed is extracted from the Equation

of State:

$$c_s^2 = \frac{\partial \mathcal{P}}{\partial e} + \frac{n}{e+P}\frac{\partial \mathcal{P}}{\partial n}. \tag{1.52}$$

- High order derivatives of fluxes are calculated for each direction (corresponding to $\nabla_i \mathbf{F}^i$ in eq. 1.34), and then the source terms ($\mathbf{S}$) are added, leaving the conserved variables ($\mathbf{U}$) be the only unknown. The time derivatives contained in some of the source terms (like in the expansion scalar) are calculated by using their values at the previous timestep.

- The evolution equations are updated in time via a second or third order Runge-Kutta time-stepping routine.

- At each temporal sub-step, the set of *primitive variables* ($\mathbf{P} = \{n, v^i, P, \Pi, \pi^{ij}\}$) is calculated starting from the updated set of corresponding conservative variables. In order to do so two different methods are exploited: an iterative relaxation method or the more refined multidimensional Newton-Raphson root-finding method, which performes the cycle on the v^i components. The latter one is the most employed, and it is summarized as follows.
  Exploiting the orthogonality conditions $\pi^{\mu\nu}u_\nu = 0$, one can express the shear stress tensor components as:

$$\pi^{0i} = \pi^{ij}v_j, \quad \pi^{00} = \pi^{0i}v_i = \pi^{ij}v_i v_j, \tag{1.53}$$

  Substituting $S^i = g^{ij}S_j$ and $\pi^{00} = -\pi^0_0$, the *conserved* variables in 1.46 can be rewritten as

$$N = n\gamma, \tag{1.54}$$
$$S^i = (e + P + \Pi)\gamma^2 v^i + \pi^{0i}, \tag{1.55}$$
$$E = (e + P + \Pi)\gamma^2 - (P + \Pi) + \pi^{00}. \tag{1.56}$$

  The components π^{ij} are by all means conserved variables, entitled by the conservation of the charge density, despite its lack of physical meaning in this frame.
  Once one has the v^i in the Local Rest Frame (LRF), the charge and energy density would be given by:

$$e = E - g_{ij}S^i v^j, \quad n = N/\gamma. \tag{1.57}$$

At this point, the secondary thermodynamic variables can be retrieved through the Equation of State. The best performing technique that was found to calculate the primitive variables is based on an iteration of the method employed in the ideal case, which takes place as an external loop over the v^i components and it is closed when a given tolerance in $|v^i_{\rm new} - v^i|$ terms is reached. The v^i are initialized with their values at the previous time-step. The cycle performs the following steps:

1. The new quantities $\tilde{E}$ and $\tilde{S}^i$ are calculated as:

$$\tilde{E} = E - \pi^{00}, \quad \tilde{S}^i = S^i - \pi^{0i};$$

   (notice that in the ideal case $\tilde{E} \equiv E$, $\tilde{S}^i \equiv S^i$, $\tilde{P} \equiv P$ so the external iteration is unnecessary).

2. An inner cycle to retrieve P is performed, which is reiterated until $|P_{\rm new} - P|$ reaches the desired tolerance.

   (a) In the inner cycle the temporary pressure is calculated, together with the associated primitive variables:

$$\tilde{P}(P) = P + \Pi, \quad v^2(P) = \tilde{S}^2/(\tilde{E} + \tilde{P})^2$$

   and

$$e(P) = (\tilde{E} + \tilde{P})(1 - v^2) - \tilde{P}, \quad n(P) = N\sqrt{1 - v^2}.$$

   (b) The cycle is iterated via a Newton-Raphson procedure, minimizing the quantity

$$f(P) = \mathcal{P}[e(P), n(P)] - P,$$

   where

$$f'(P) = \frac{\partial \mathcal{P}}{\partial e}\frac{de}{dP} + \frac{\partial \mathcal{P}}{\partial n}\frac{dn}{dP} - 1.$$

   The updated value of the pressure becomes:

$$P_{\rm new} = P - f(P)/f'(P),$$

3. Once retrieved the pressure corresponding to the v^i components, their updated value is provided by:

$$v^i_{\rm new} = \tilde{S}^i/(\tilde{E} + \tilde{P}).$$

The same procedure can be applied when also the π^{00} and π^{0i} viscous terms were evolved. Thanks to the conservative nature of N, they represent conservative variables, avoiding the necessity of applying the orthogonality condition to extract them.

- The output of primitive variables and other diagnostic quantities are provided for selected output times.

1.4 Validation of the ECHO-QGP

ECHO-QGP has undergone several numerical test, devoted to the evaluation of its response against shocks, of its accuracy in solving equations and its reliability in treating the plasma in extreme conditions. In this section a summary of its performances can be found.

1.4.1 Mildly relativistic 1D shear flow

Assuming a flow that is only mildly relativistic, the diffusion of a shear flow profile in (1+1)D is known analytically. A similar case has already been studied for testing numerical algorithms for relativistic viscosity [88] and also resistive magnetohydrodynamics [45]. This test has been performed in Minkowski coordinates, choosing a velocity profile $v^y = v^y(x)$. For sub-relativistic speeds and a uniform background state in terms of energy density and pressure, at any time t of the evolution, only v^y will change due to shear viscosity (the bulk viscosity does not play a role since $\theta \equiv 0$), always preserving $\gamma \approx 1$. In such Navier-Stokes limit, the momentum equation along y reads

$$(e+P)\partial_t v^y + \partial_x \pi^{xy} = 0, \quad \pi^{xy} = -2\eta\sigma^{xy} = -\eta\partial_x v^y,$$

which leads, for a constant η coefficient, to the classical 1D diffusion equation

$$\partial_t v^y = D_\eta \partial_x^2 v^y, \quad D_\eta = \eta/(e+P),$$

with (constant) diffusion coefficient D_η. Assuming a step function for the $v^y(x)$ profile at $t = 0$, with constant values $-v_0$ for $x < 0$ and v_0 for $x > 0$, it is possible to express the exact solution at any time t as:

$$v^y = v_0 \,\mathrm{erf}\left[\frac{1}{2}\sqrt{\frac{x^2}{D_\eta t}}\right].$$

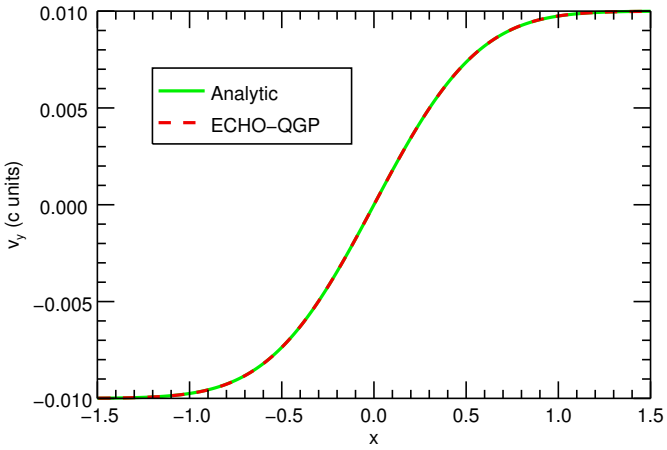

Figure 1.2: *Comparison between the ECHO-QGP evolution output and the analytic solution at $t = 10$ fm/c for the dependence of the velocity, in the case of mildly relativistic 1D shear flow. The numerical setup is shown in table 1.1*

v_0	η GeV/fm^3	D_η fm	N_x	$[x_{\min}; x_{\max}]$ fm
0.01	0.01	0.01	301	[-1.5,1.5]

Table 1.1: *Setup for the mildly relativistic 1D shear flow test. The chosen EoS is $e + P = 4P = 1 GeV/fm^3$. The comparison with the analytical result is shown in fig. 1.2*

In order to proceed to the numerical test, the above profile has been used at the initial time $t = 1$ fm/c instead of the discountinuous step function, letting ECHO-QGP evolve it up to late times ($t = 10$ fm/c). The result of such evolution (with the setup described in table 1.1) has then been compared to the analytical solution for the corresponding time (see fig. 1.2), showing perfect agreement.

1.4.2 2D shock tubes

Shock-capturing numerical schemes, as in the classical hydrodynamical case, are designed to handle and evolve discontinuous quantities inevitably arising due to the nonlinear nature of the fluid equations. In order to validate these codes, typical tests are the so-called shock-tube 1D problems.

N_x	N_y	$[x_{\min}; x_{\max}]$ fm	$[y_{\min}; y_{\max}]$ fm	t_{end} fm/c
201	201	$[-4; 4]$	$[-4; 4]$	4

T^L GeV	P^L GeV/fm^3	T^R GeV	P^R GeV/fm^3	η/s
0.4	5.4	0.2	0.34	0/0.01/0.1

Table 1.2: *Setup for the shock tube test, performed with EOS-I (see sec. 2.2) and different values for η/s. The comparison with the analytical result is shown in fig. 1.3*

Two uniform states are taken on the left and on the right with respect of an imaginary diaphragm, which is supposed to be initially present and then removed at $t = 0$. Typical patterns seen in the subsequent evolution are shocks and rarefaction waves. In performing this test, a relativistic blast wave explosion problem is considered, which is characterized by an initial static state with temperature and pressure much higher in the region on the left, namely $T^L = 0.4$ GeV ($P^L = 5.40$ GeV/fm^3) and $T^R = 0.2$ GeV ($P = 0.34$ GeV/fm^3). In order to make a more stringent test, the shock-tube test has been performed by placing the initial diaphragm along the diagonal of a square box adopting Minkowskian coordinates 2+1D, and by letting the system evolve in a higher-dimensionality frame from $t = 0$ up to $t = 4$ fm/c. The same test has been repeated for the ideal case and for different values of the shear viscosity η/s (0.1 and 0.01). Some of the results of this test, performed within the setup described in table 1.2 are shown in in fig. 1.3, in particular one can find the velocity profile v_x, the expansion scalar θ, the energy density e, and the component of the shear stress tensor $-2\pi^{zz}$, as a function of x and along the axis $y = 0$. As in [71], at the final time ($t_{\text{end}} = 4$ fm/c), ECHO-QGP shows to be free fom numerical spurious oscillations near the shock front even in the ideal (stiffer) case. When introducing the viscosity, profiles are smoother for increasing values of η/s. Small oscillations can be seen in θ (mainly due to the low accuracy in the time derivative) for the largest value of the viscosity.

1.4.3 Boost invariant expansion along z-axis

As a first validation of ECHO-QGP in Bjorken coordinates it was considered a test with no dependence on the transverse coordinates (x, y), implying a vanishing vorticity. For this test, a boost invariance along the z-direction is

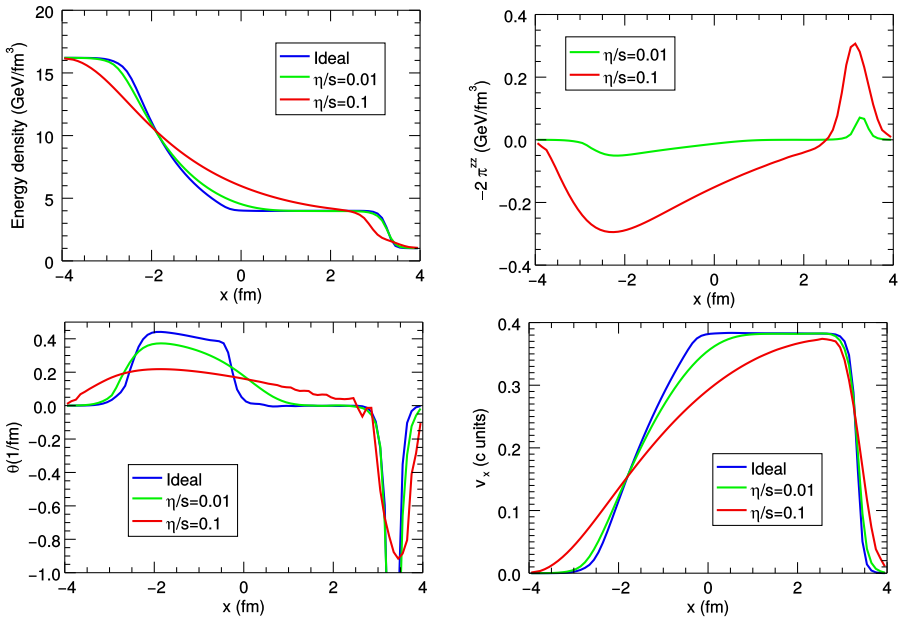

Figure 1.3: *Hydrodynamic quantities in a relativistic blast wave explosion problem. In this panel there are respectively the energy density e, the component $-2\pi^{zz}$ of the shear stress tensor, the expansion rate θ, and the velocity component v_x, as a function of x for $\eta/s = 0, 0.01, 0.1$ at $t_{\rm end} = 4$ fm/c. The numerical setup is shown in table 1.2*

assumed, thus the involved quantities do not depend on η_s either, reducing the dependence of the system to the time coordinate (0+1D test). The evolution of uniform quantities will be then just due to the τ dependence of the $g_{\eta\eta}$ term in the metric tensor, in the absence of velocities. The energy-momentum tensor simplifies to:

$$T^{\mu\nu} \equiv \mathrm{diag}\{e,\ P+\Pi+\pi^{xx},\ P+\Pi+\pi^{yy},\ (P+\Pi)/\tau^2+\pi^{\eta\eta}\}$$

where π^{xx}, π^{yy}, and $\pi^{\eta\eta}$ are the only non-vanishing components of the shear stress tensor. Applying to the latter its tracelessness property and exploiting the assumed simmetries, it is possible to write those components as:

$$2\pi^{xx} = 2\pi^{yy} = -\tau^2\pi^{\eta\eta} \equiv \phi,$$

so only one independent component of $\pi^{\mu\nu}$ is sufficient to describe the system. Despite this simplification and in order to guarantee the reliability of the code, in this test ECHO-QGP evolves all 6 spatial components

τ_0 fm/c	η/s	ζ GeV/fm^2	τ_π fm/c
1	0.08	0.01	1

Table 1.3: *Parameters setup for the boost invariant expansion along z-axis. The comparison with the analytical results is shown in fig. 1.5.*

starting at $\tau = 1$ fm/c from a constant initial energy density profile, and never imposing tracelessness. The system as described admits an analytical solution, provided that first-order theory applies. The energy equation is then enough to describe the overall evolution

$$\frac{\partial e}{\partial \tau} = -\frac{e + P + \Pi - \phi}{\tau}. \tag{1.58}$$

Within the first-order theory, Π and ϕ can be obtained from their Navier-Stokes (NS) values

$$\Pi = -\frac{\zeta}{\tau}, \qquad \phi = \frac{4\eta}{3\tau}.$$

Employing the ultrarelativistic gas EoS and assuming constant values for η/s and for ζ/s, eq. (1.58) admits the following analytic solution [89–91] for the temperature as a function of the proper time:

$$T(\tau) = T_0 \left(\frac{\tau_0}{\tau}\right)^{\frac{1}{3}} \left[1 + \frac{4\eta/3s + \zeta/s}{2\tau_0 T_0}\left(1 - \left(\frac{\tau_0}{\tau}\right)^{\frac{2}{3}}\right)\right],$$

where T_0 is the temperature at the initial proper time τ_0. This last analytic form is compared with the outcome of ECHO-QGP, set up to reproduce the Navier-Stokes limit. Such comparison can be seen in fig. 1.4 (where ζ/s has been set to 0).

On the other hand, an analytic solution for the evolution equations extracted within the second-order theory has never been derived. However, assuming that the evolution of Π and ϕ is simply governed by the relaxation part of the source terms one can write ($\tau_\pi = \tau_\Pi$):

$$\frac{\partial \Pi}{\partial \tau} = -\frac{1}{\tau_\Pi}\left(\Pi + \frac{\zeta}{\tau}\right) - \frac{4\Pi}{3\tau} \quad \rightarrow \quad \frac{\partial \Pi}{\partial \tau} = -\frac{1}{\tau_\pi}\left(\Pi + \frac{\zeta}{\tau}\right) \tag{1.59}$$

$$\frac{\partial \phi}{\partial \tau} = -\frac{1}{\tau_\pi}\left(\phi - \frac{4\eta}{3\tau}\right) - \frac{4\phi}{3\tau} - \tau^2 \mathcal{I}_1^{\eta\eta} \quad \rightarrow \quad \frac{\partial \phi}{\partial \tau} = -\frac{1}{\tau_\pi}\left(\phi - \frac{4\eta}{3\tau}\right). \tag{1.60}$$

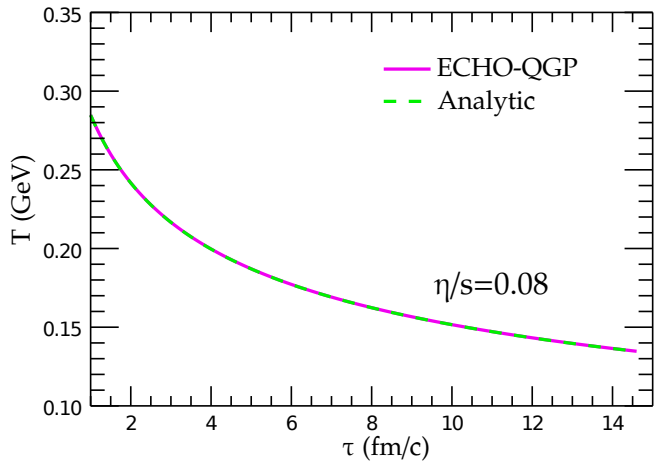

Figure 1.4: *Comparison between the analytic solution and the same quantity computed numerically by ECHO-QGP of the evolution of the temperature $T(\tau)$ derived in the context of the first-order Navier-Stokes theory (eq. 1.58). Here $\zeta/s = 0$*

Assuming η, ζ and τ_π to be independent of the temperature, eqs. (1.59,1.60) admit the following semi-analytic solution for Π and ϕ:

$$\Pi(\tau) = \Pi(\tau_0)\, \mathrm{e}^{-\frac{\tau-\tau_0}{\tau_\pi}} + \frac{\zeta}{\tau_\pi}\, \mathrm{e}^{-\frac{\tau}{\tau_\pi}} \left[\mathrm{Ei}\left(\frac{\tau_0}{\tau_\pi}\right) - \mathrm{Ei}\left(\frac{\tau}{\tau_\pi}\right) \right], \tag{1.61}$$

$$\phi(\tau) = \phi(\tau_0)\, \mathrm{e}^{-\frac{\tau-\tau_0}{\tau_\pi}} - \frac{4\eta}{3\tau_\pi} \mathrm{e}^{-\frac{\tau}{\tau_\pi}} \left[\mathrm{Ei}\left(\frac{\tau_0}{\tau_\pi}\right) - \mathrm{Ei}\left(\frac{\tau}{\tau_\pi}\right) \right], \tag{1.62}$$

where, $\mathrm{Ei}(x)$ denotes the exponential integral function.

The above solutions are obtained from ECHO-QGP under the same assumptions. The comparison between the ECHO-QGP output and the semi-analytic solution for the evolution of Π is shown in fig. 1.5, showing perfect agreement.

1.4.4 2+1D tests with azimuthal symmetry

The study that naturally follows the 0+1D test in Bjorken coordinates, is the boost-invariant case (still $\partial_\eta \equiv 0$) where one also considers the evolution in the transverse plane. When the initial state (at τ_0) is azimuthally invariant, the 2+1D evolution with ECHO-QGP can be compared with analytic results in 1+1D.
Three different solutions have been derived that apply to this situation:

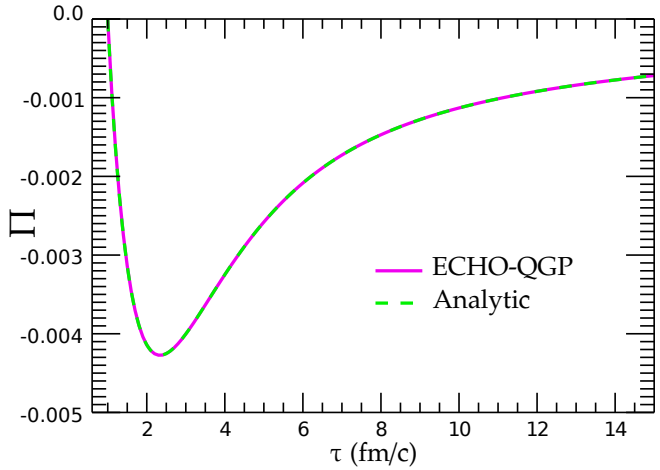

Figure 1.5: *Comparison between the analytic solution and the same quantity computed numerically by ECHO-QGP of the evolution of the bulk viscosity $\Pi(\tau)$ for the second-order derivation (see eq. 1.61). The numerical parameters setup can be found in tab. 1.3.*

the first one assumes a Woods-Saxon initial profile for the energy density and a viscous free evolution [12]; the second and the third ones are an analytical solution (under the assumption of cold plasma) [92] and a semi-analytical solution (less stringent assumptions) of the viscous equations of motions starting from an azhimuthally symmetric initial profile created ad-hoc [68, 93, 94].

Baym's solution for a Woods-Saxon profile initialization

For the first case, it is assumed a Woods-Saxon profile for the initial energy density, as appropriate for central nucleus-nucleus collisions:

$$e(r, \tau_0) = \frac{e_0}{1 + \exp\left[(r - R)/\sigma\right]},$$

where τ_0 is the initial time, $r = (x^2 + y^2)^{1/2}$ is the radius in the transverse plane, and R can be thought of as the radius of the nuclei. The analytical solution for the subsequent evolution, as a function of τ and r, was found in ref. [12] and it has been be compared with ECHO-QGP numerical results, with the setup described in table 1.4. As shown in Fig. 1.6, there is a perfect agreement between the analytic solution and ECHO-QGP, at any proper time τ during the evolution.

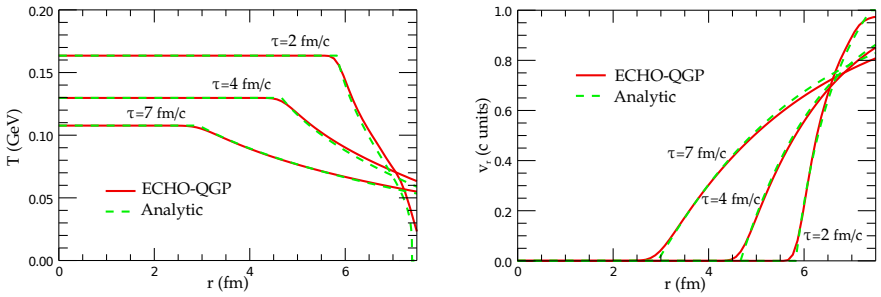

Figure 1.6: *Spatial dependence of the temperature and of the radial velocity at different times along with the analytic solution in the case of a Woods-Saxon initial condition with cylindrical symmetry. Results obtained with ECHO-QGP in 2+1D agree very well with the analytical solution by Baym et al. [12].*

R	r	σ	T_0
fm	fm	fm	GeV
6.4	0	0.02	0.2

Table 1.4: *Setup for the 2+1D test (see sec. 1.4.4) with azimuthal symmetry and boost invariance, performed with a Woods-Saxon initial condition for the energy density profile. Results are shown in fig. 1.6*

Gubser flow

A very useful test for a numerical code of relativistic dissipative hydrodynamics is the extension of the ideal solution found by Gubser and Yarom [92, 95], in the case of a Bjorken flow with an azimuthally symmetric radial expansion, to the viscous case [68, 94]. Indeed, this solution provides a highly non-trivial theoretical benchmark.

For the sake of clarity, the main steps leading to the analytical solution are briefly summarized below, ad then a comparison with the numerical computation is shown in fig. 1.7.

In the case of a conformal fluid, with $P = e/3$ EoS, the invariance for scale transformations constrains the terms entering the second-order viscous hydrodynamic equations. The additional requests of azimuthal and longitudinal-boost invariance, constrain the solution of the hydrodynamic equations, which has to be invariant under $SO(3)_q \otimes SO(1,1) \otimes Z_2$ transformations. To start with, one defines a modified space-time metric as

Δx fm	Δy fm	$\Delta\eta_s$	$\Delta\tau$ fm/c	η/s	τ_R	q fm^{-1}
0.025	0.025	0.025	0.001	0.2	$5\eta/(e+P)$	1

Table 1.5: *Parameters setup for the Gubser test. 1.7*

follows (with usual Bjorken coordinates, η_s being the spacetime rapidity):

$$ds^2 = \tau^2\left(\frac{d\tau^2 - dr^2 - r^2 d\phi^2}{\tau^2} - d\eta_s^2\right),$$

which can be viewed as a rescaling of the metric tensor:

$$ds^2 \longrightarrow d\hat{s}^2 \equiv ds^2/\tau^2 \quad \Longleftrightarrow \quad g_{\mu\nu} \longrightarrow \hat{g}_{\mu\nu} \equiv g_{\mu\nu}/\tau^2.$$

It can be shown that $d\hat{s}^2$ is the invariant spacetime interval of $dS_3 \otimes R$, where dS_3 is the three-dimensional de Sitter space and R refers to the rapidity coordinate. It is then convenient to perform a coordinate transformation (q is an arbitrary parameter setting an energy scale for the solution once one goes back to physical dimensionful coordinates)

$$\sinh\rho \equiv -\frac{1-q^2(\tau^2-r^2)}{2q\tau}, \quad \tan\theta \equiv \frac{2qr}{1+q^2(\tau^2-r^2)}, \tag{1.63}$$

after which the rescaled spacetime element $d\hat{s}^2$ reads

$$d\hat{s}^2 = d\rho^2 - \cosh^2\rho\,(d\theta^2 + \sin^2\theta\, d\phi^2) - d\eta_s^2. \tag{1.64}$$

The full symmetry of the problem is now manifest. $SO(1,1)$ and Z_2 refer to the usual invariance for longitudinal boosts and $\eta_s \to -\eta_s$ inversion, while $SO(3)_q$ reflects the spherical symmetry of the rescaled metric tensor in the new coordinates. In Gubser coordinates the fluid is at rest:

$$\hat{u}_\rho = 1, \quad \hat{u}_\theta = \hat{u}_\phi = \hat{u}_\eta = 0. \tag{1.65}$$

As shown in [92–95], an analytical solution for Israel-Stewart theory can be found in the cold plasma limit, (i.e. extremely large viscosity or extremely small temperatures), solving eq. 1.66b where the term $\pi^{\mu\nu}$ is removed from the Israel-Stewart theory. This solution no longer relaxes to Navies-Stokes theory, but it has been used as a test to guarantee the behavior of ECHO-QGP under any circumnstace. Such comparison is shown in fig. 1.8. The corresponding flow in Minkowski space can be obtained taking into account

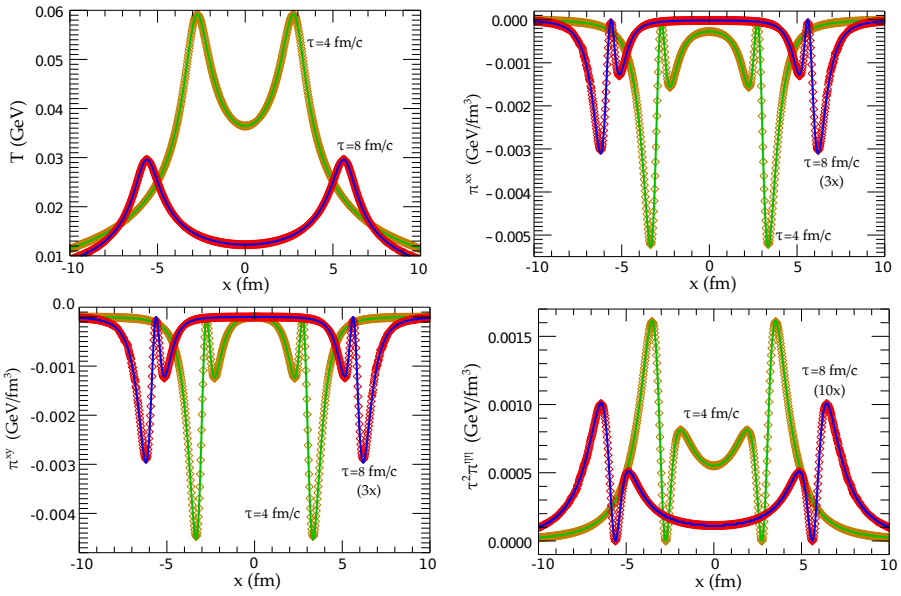

Figure 1.7: *Comparison between the semi-analytic solution of the Gubser viscous flow and a computation carried out with the ECHO-QGP code.*

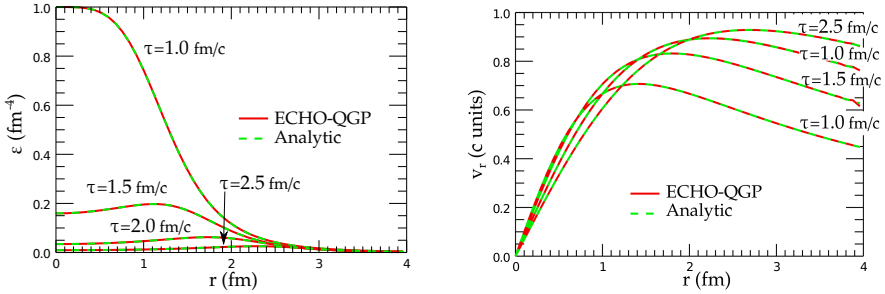

Figure 1.8: *Comparison of the radial dependence of the energy density e (left panel) and of the radial velocity v_r (right panel) with the Gubser flow [92] at $\tau = 1.0,\ 1.5,\ 2.0,\ 2.5$ fm/c. ECHO-QGP outcomes show a perfect matching with the analytical results.*

both the rescaling of the metric and the change of coordinates

$$u_\mu = \tau \frac{\partial \hat{x}^\nu}{\partial x^\mu} \hat{u}_\nu,$$

where $\hat{x}^\mu = (\rho, \theta, \phi, \eta_s)$ and $x^\mu = (\tau, r, \phi, \eta_s)$. Other quantities such as the temperature or the viscous tensors require the solution of the following set of hydrodynamic equations (their most general form actually admits further terms that were derived for a system of massless particles in refs. [96, 97]),

valid for the case of a conformal fluid with $e = 3P \sim T^4$:

$$\frac{DT}{T} + \frac{\theta}{3} - \frac{\pi_{\mu\nu}\sigma^{\mu\nu}}{3sT} = 0 \tag{1.66a}$$

$$\tau_\pi \left(\Delta^\mu_\alpha \Delta^\nu_\beta D\pi^{\alpha\beta} + \frac{4}{3}\pi^{\mu\nu}\theta \right) + \pi^{\mu\nu} = 2\eta\sigma^{\mu\nu}. \tag{1.66b}$$

In the case of the Gubser flow in Eq. (1.65), due to the traceless and transverse conditions $\hat{\pi}^\mu_\mu = 0$ and $\hat{u}_\mu \hat{\pi}^\mu_\nu = 0$, one has simply to solve the two equations ($\bar{\pi}^{\eta\eta} \equiv \hat{\pi}^{\eta\eta}/\hat{s}\hat{T}$)

$$\frac{1}{\hat{T}}\frac{d\hat{T}}{d\rho} + \frac{2}{3}\tanh\rho = \frac{1}{3}\bar{\pi}^{\eta\eta}\tanh\rho \tag{1.67}$$

and

$$\hat{\tau}_R \left[\frac{d\bar{\pi}^{\eta\eta}}{d\rho} + \frac{4}{3}\left(\bar{\pi}^{\eta\eta}\right)^2 \tanh\rho \right] + \bar{\pi}^{\eta\eta} = \frac{4}{3}\frac{\hat{\eta}}{\hat{s}\hat{T}}\tanh\rho. \tag{1.68}$$

The solution can be then mapped back to Minkowski space through the formulae:

$$T = \hat{T}/\tau, \qquad \pi_{\mu\nu} = \frac{1}{\tau^2}\frac{\partial \hat{x}^\alpha}{\partial x^\mu}\frac{\partial \hat{x}^\beta}{\partial x^\nu}\hat{\pi}_{\alpha\beta}. \tag{1.69}$$

The figures in the panel 1.7 show the comparison between the Gubser flow analytical and semi-analytical solutions and ECHO-QGP numerical computation for temperature and the components π^{xx}, π^{xy} and $\pi^{\eta\eta}$ of the viscous stress tensor respectively, at different times. The initial energy density profile is taken from the exact Gubser solution at the time $\tau = 1$ fm/c. The simulation is performed with a grid of 0.025 fm in space and 0.001 fm/c in time. The shear viscosity to entropy density ratio is set to $\eta/s = 0.2$, while the shear relaxation time is $\tau_R = 5\eta/(\varepsilon + p)$. The energy scale is set to $q = 1fm^{-1}$.

As it can be seen, the agreement is excellent up to late times.

1.4.5 3+1D test in Minkowski

As last test, it has been considered the 3+1D case in the presence of a spherically symmetric initial pressure or energy-density profile. This test is essential to check the accuracy of the viscous implementation by verifying that the symmetries are preserved by the spatial velocity components during the whole fireball evolution. Due to the spherical symmetry of the system it is expected a pure radial dependence of the fluid velocity $\vec{v} = v(r,t)\vec{r}/r$ throughout all the medium evolution, for both inviscid and viscous fluids. To perform this test, the initial pressure profile is chosen to

σ fm	R fm	P_0 GeV/fm^3	T_0 GeV	η/s
0.5	6.4	4	0.307	0.16

N_x	N_y	N_z	range fm	t_{stop} fm/c
101	101	101	$[-20:20]$	10

Table 1.6: *Parameters setup for (3+1)-D Minkowski test referring to the results shown in fig. 1.9*

be of Woods-Saxon type as in Eq. (*1.4.4*), with P and P_0 replacing e and e_0, now in flat Cartesian coordinates with $r = (x^2 + y^2 + z^2)^{1/2}$. With the parameters shown in table 1.6, we perform the tests with either EOS-LS and EOS-PCE (see section *2.2*), precisely to investigate the behavior of different EOS's in a realistic 3D case. The fluid 4-velocity is initialized through the Bjorken condition (at the initial time is $u^\mu = (1, 0, 0, 0)$), and in the viscous case the shear stress tensor is initialized to 0 ($\pi^{\mu\nu} \equiv 0$ and $\zeta/s = \Pi = 0$), since boosting effects are not present in Minkowski. v_x, v_y, v_z are plotted along their respective axes in Fig. 1.9, perfectly lying on top of each other, both for the inviscid and the viscous cases. Shear viscous effects play the usual role of smoothing the velocity profiles, as expected.

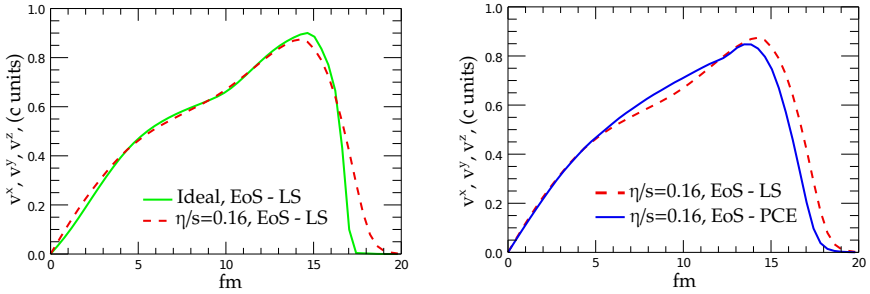

Figure 1.9: *Comparison at $t = 10$ fm/c of the spatial components of fluid velocity in a 3D run in Minkowski coordinates (setup described in table 1.6).*

2

Numerical Set-Up, Features and results of ECHO-QGP

In order to apply the hydrodynamic description to heavy-ion collisions, one necessarily needs other, complementay, models to fix the unknown parameters. In this chapter, we show how the initial and the final stages of the evolution are modeled in ECHO-QGP, as well as the Equation of State used.

2.1 Initial conditions

Various choices of initial conditions are implemented in the ECHO-QGP and are selectable by the user, including the test problems used for the numerical validation of the code showed in section *1.4*.

Initialization is done by setting either the energy density or the entropy density distribution at the initial time τ_0. In the 2D case, these quantities receive both a soft (proportional to the density of participant nucleons n_{part}) and a hard (proportional to the density of binary collisions n_{coll}) contribution, with relative weight given by the coefficient $\alpha \in [0, 1]$ (see, e. g. [98]):

$$e(\tau_0, \mathbf{x}; b) = e_0 \left[(1-\alpha) \frac{n_{\text{part}}(\mathbf{x}; b)}{n_{\text{part}}(\mathbf{0}; 0)} + \alpha \frac{n_{\text{coll}}(\mathbf{x}; b)}{n_{\text{coll}}(\mathbf{0}; 0)} \right],$$

where $e(\tau_0, \mathbf{x}; b)$ stands for either the energy or the entropy-density and e_0 is the corresponding value at $\mathbf{x}=\mathbf{0}$ and $b=0$, $\mathbf{x}$ and b being the coordinates

in the transverse plane and the impact parameter respectively. In the optical Glauber model, for two colliding nuclei of mass numbers A and B, the global density of participants ($n_{\rm part}$) and of binary collisions ($n_{\rm coll}$) in the transverse plane are respectively given by

$$n_{\rm part}(\mathbf{x};b) \equiv n^A_{\rm part}(\mathbf{x};b) + n^B_{\rm part}(\mathbf{x};b), \tag{2.1}$$

with

$$n^A_{\rm part}(\mathbf{x};b) = T_A\left(\mathbf{x}+\frac{\mathbf{b}}{2}\right)\left\{1-\left[1-\frac{\sigma^{NN}}{B}T_B\left(\mathbf{x}-\frac{\mathbf{b}}{2}\right)\right]^B\right\},$$
$$n^B_{\rm part}(\mathbf{x};b) = T_B\left(\mathbf{x}-\frac{\mathbf{b}}{2}\right)\left\{1-\left[1-\frac{\sigma^{NN}}{A}T_A\left(\mathbf{x}+\frac{\mathbf{b}}{2}\right)\right]^A\right\},$$

and

$$n_{\rm coll}(\mathbf{x};b) = \sigma^{NN}\, T_A\left(\mathbf{x}+\frac{\mathbf{b}}{2}\right) T_B\left(\mathbf{x}-\frac{\mathbf{b}}{2}\right). \tag{2.2}$$

σ^{NN} is the inelastic nucleon-nucleon cross-section, and $T_{A/B}$ is the nuclear thickness function (respectively for the nucleus A or B):

$$T(\mathbf{x}) \equiv \int_{-\infty}^{\infty} dz\, \rho(\mathbf{x},z) = \int_{-\infty}^{\infty} dz\, \frac{\rho_0}{1+{\rm e}^{(\sqrt{\mathbf{x}^2+z^2}-R)/\delta}} \tag{2.3}$$

In Eq. (2.3) ρ is a Fermi parameterization of the nuclear density distribution (ρ_0, δ and R are respectively the nuclear density, the width and the radius of the nuclear Fermi distribution) [99]. The tunable parameters are the maximum initial energy density in central collisions e_0 and the hardness fraction α.

In the 3D case the initialization is performed using a model for the density distribution similar to the one of refs. [31, 100], charachterized by an energy density (or equivalently entropy density) profile that vanishes at space-time rapidity η_s larger than the beam-rapidity $Y_b \approx \ln(\sqrt{s_{\rm NN}}/m_p)$:

$$e(\tau_0,\mathbf{x},\eta_s;b) = \tilde{e}_0\, \theta(Y_b-|\eta_s|)\, f^{\rm pp}(\eta_s)\, [\alpha n_{\rm coll}(\mathbf{x};b) + (1-\alpha)\tilde{n}_{\rm part}] \tag{2.4}$$
$$\tilde{n}_{\rm part} = \left(\frac{Y_b-\eta_s}{Y_b} n^A_{\rm part}(\mathbf{x};b) + \frac{Y_b+\eta_s}{Y_b} n^B_{\rm part}(\mathbf{x};b)\right) \tag{2.5}$$

Notice that here $\tilde{e}_0$ does not represent the energy or entropy-density at $\mathbf{x}=\mathbf{0}$ and $b=0$, but it is simply an overall normalization factor. The particles produced by the participants of nucleus A/B tend to follow the

rapidity of their respective source: this effect is parametrized by the factors $(Y_b \pm \eta_s)/Y_b$. The function $f^{\rm pp}(\eta_s)$ describes the rapidity profile in p-p collisions (see sketch in fig. 2.1):

$$f^{\rm pp}(\eta_s) = \exp\left[-\theta(|\eta_s| - \Delta\eta)\frac{(|\eta_s| - \Delta\eta)^2}{\sigma_\eta^2}\right].$$

This is a flat profile for $|\eta_s| \leq \Delta\eta$ and displays a gaussian damping at forward/backward rapidities. The extension of the rapidity plateau $\Delta\eta$ and the width σ_η of the gaussian falloff are the two further parameters describing the rapidity dependence in the 3D case. Any other functional form can be implemented by the user.

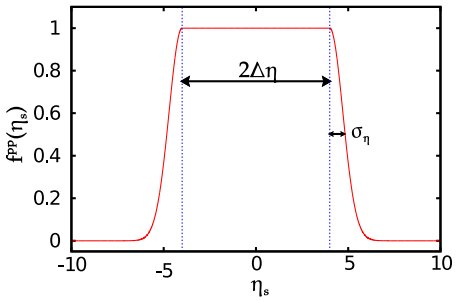

Figure 2.1: *sketch of the shape of the rapidity profile in p-p collisions*

ECHO-QGP includes also the possibility of performing event-by-event hydro calculations with fluctuating initial conditions. A simple Glauber Monte Carlo routine is provided with the code:

- A sample of $N_{\rm conf}$ nuclear configurations is generated, extracting randomly the positions of the nucleons of the A and B nuclei from a Woods-Saxon distribution. The transverse positions of the nucleons in each nucleus is then reshuffled into the respective center-of-mass frame.

- For a given configuration a random impact parameter $b \in [0, b_{\rm max}]$ is extracted from the distribution $dP = 2\pi b db$. Nucleons i (from nucleus A) and j (from nucleus B) collide if $(x_i - x_j)^2 + (y_i - y_j)^2 < \sigma_{\rm NN}/\pi$. If at least a binary nucleon-nucleon collision occurred the event is kept and the information ($\mathbf{x}^A_{\rm part}$, $\mathbf{x}^B_{\rm part}$ and $\mathbf{x}_{\rm coll}$) is stored, otherwise not. The procedure is repeated $N_{\rm trials}$ times for each configuration of the incoming nuclei.

- Each participant nucleon and collision, with a gaussian smearing of variance σ, is a source of energy density (with the parameter α

setting the hardness fraction):

$$e(\tau_0, \mathbf{x}) = \frac{K}{2\pi\sigma}\left\{(1-\alpha)\sum_{i=1}^{N_{\rm part}}\exp\left[-\frac{(\mathbf{x}-\mathbf{x}_i^{\rm part})^2}{2\sigma^2}\right] + \alpha\sum_{i=1}^{N_{\rm coll}}\exp\left[-\frac{(\mathbf{x}-\mathbf{x}_i^{\rm coll})^2}{2\sigma^2}\right]\right\}. \quad (2.6)$$

The model has been employed in ref. [101] and tuned, with a pure dependence on participants ($\alpha = 0$), to Au-Au data at RHIC (see Fig. (2.2)). The rapidity dependence in the 3D case can be inserted *a posteriori* as in the optical-Glauber initialization of Eq. (2.5). Storing information both on $\mathbf{x}^A_{\rm part}$ and on $\mathbf{x}^B_{\rm part}$ it is even possible to account for the different rapidity dependence of the contributions of the participants from the two nuclei (leading to a direct flow v_1 far from mid-rapidity).

Initial conditions for the flow are chosen in both the 2D and 3D cases in order to have, at $\tau = \tau_0$, zero transverse flow velocities and a longitudinal flow given by the Bjorken's solution ($Y = \eta_s$). Other choices can be easily implemented.

2.1.1 MC-Glauber initial conditions: a test case

Here, we demonstrate the capability of running 2+1D ideal and viscous Relativistic Hydro-Dynamics (RHD) simulations with ECHO-QGP in the case of fluctuating Glauber-MC initial conditions. The local temperature profile is set at the initial time $\tau = 1$ fm/c for one particular nuclear configuration generated through the Glauber-MC routine implemented in ECHO-QGP (we assume Au-Au collisions with $b_{\rm max} = 20$, $\sigma = 0.6$ fm, $K = 37.8$ GeV/fm^2, and $\alpha = 0.2$); then the subsequent evolution is followed both in the ideal and in the viscous case. In Fig. 2.3 the initial and later stages of the evolution at $\tau = 5$ and 10 fm/c are shown, where the upper row refers to the ideal run and the lower one to the viscous run. Here we assume a square numerical box ranging from -15 to 15 fm and made up by 151 grid points in both directions. The equation of state applied here is the one computed by ref. [102] (see next subsection), while in the viscous run we set $\eta/s = 0.08$.

Clearly, the dynamical effects of shear viscosity are reflected in the smoother spatial profiles: the surfaces of discontinuity arising from the transverse expansion of the initial peaks of energy (shock fronts) are clearly

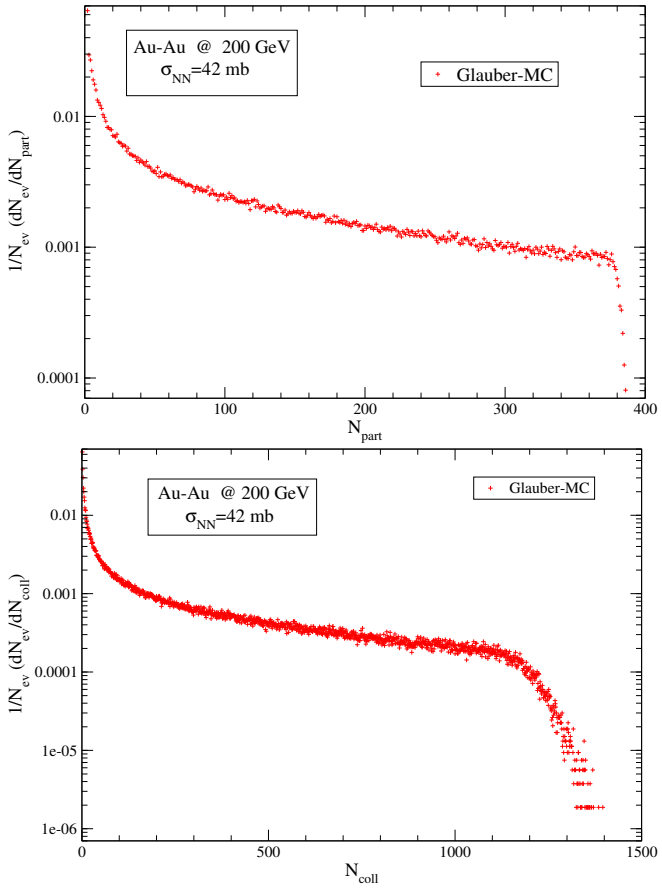

Figure 2.2: *The participant and binary-collision distribution from the Glauber-MC simulations of Au-Au events at* $\sqrt{s_{NN}} = 200$ *GeV.*

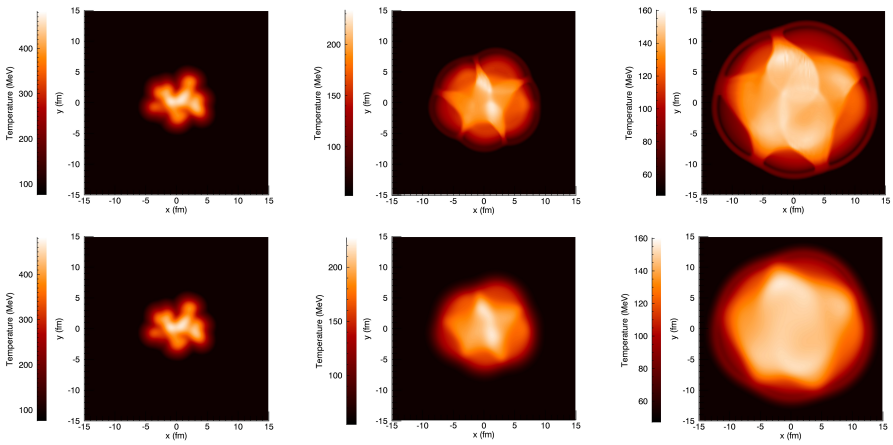

Figure 2.3: *Temperature scans at various times – at $\tau = 1$, 5, and 10 fm/c – obtained from inviscid (upper panel) and viscous (lower panel) ECHO-QGP simulations with Glauber-MC initial conditions. The differences between the two cases are clearly visible. The effect of shear viscosity can be seen in the smoothening of the profiles.*

visible only in the inviscid case. These results demonstrate the capability of ECHO-QGP to handle also complex initial conditions with events displaying sizable fluctuations. The full analysis including the study of higher-order flow harmonics, of the impact on the freeze-out stage and of the final particle spectra is beyond the scope of the present investigation and is left for future work.

2.2 Equation of State

Solving hydrodynamics equations requires the knowledge of the Equation of State (EoS) of the system. Although the code is already designed to handle any form of $P = \mathcal{P}(e, n)$, in the present work we just consider the case $P = \mathcal{P}(e)$, i.e. the case of a barotropic fluid. ECHO-QGP allows the use of any tabulated EoS of this kind, if provided by the user in the format $(T, e/T^4, P/T^4, c_s^2)$, with $c_s^2 \equiv dP/de$, the square of the speed of sound.

However, some choices are already implemented in the code and are offered to the user. Test runs can be performed with the ideal ultrarelativistic

EoS $P = e/3$. More precisely, we set in these cases

$$P = e/3 = \frac{g\pi^2}{90} T^4, \quad c_s^2 = \frac{1}{3},$$

where $g = 37$ for a non-interacting QGP with 3 light flavors.

More realistic QCD EoS's are included in the package, in the tabulated form mentioned above, and can be selected by the user such as the EoS of ref. [102], arising from a weak-coupling QCD calculation with realistic quark masses and employed in the code by Romatschke [35].

ECHO-QGP includes also two tabulated EoS's obtained by matching a Hadron-Resonance-Gas EoS (HRG EoS) at low temperature with the continuum-extrapolated lattice-QCD results by the Budapest-Wuppertal collaboration [103]. The HRG EoS was obtained by summing the contributions of all hadrons and resonances in the PDG up to a mass of 2 GeV: $P = \sum_r P_r$. In the classical limit $T \ll m_r$ (quantum corrections are included for pions, kaons and η's) one has simply, for the pressure of the resonance r:

$$P_r = g_r \frac{T^2 m_r^2}{2\pi^2} e^{\mu_r/T} K_2\left(\frac{m_r}{T}\right), \tag{2.7}$$

and the density of resonance r in the cocktail is given by

$$n_r \equiv \left(\frac{\partial P}{\partial \mu_r}\right)_T = g_r \frac{T m_r^2}{2\pi^2} e^{\mu_r/T} K_2\left(\frac{m_r}{T}\right). \tag{2.8}$$

In the Chemical Equilibrium case (CE) in the hadronic phase all the chemical potentials vanish ($\{\mu_r = 0\}$) and the multiplicity of any resonance r is simply determined by the temperature through the ratio m_r/T. On the other hand experimental data provide evidence that the chemical freeze-out – in which particle ratios are fixed – occurs earlier than the kinetic one, in which particle spectra gets frozen. A realistic EoS should in principle contain the correct chemical composition in the hadronic phase. This can be enforced in the following way. At the chemical freeze-out temperature T_c the abundances n_r of all the resonances are determined by Eq. (2.8) with $\mu_r = 0$. Afterwards, the fireball evolves maintaining Partial Chemical Equilibrium (PCE): elastic interactions mediated by resonances ($\pi\pi \to \rho \to \pi\pi$, $K\pi \to K^* \to K\pi$, $p\pi \to \Delta \to p\pi$...) are allowed, changing the abundance of the single resonances r, but conserving the "effective

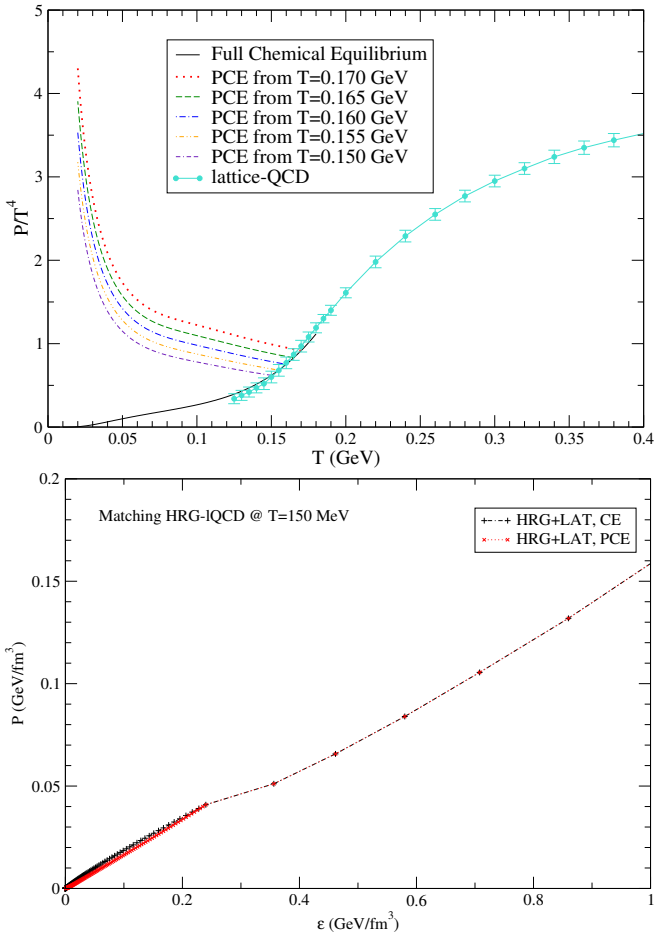

Figure 2.4: *Upper panel: HRG EoS, with chemical (CE, black continuous line) and partial chemical equilibrium (PCE, colored dotted/dashed lines), vs the lattice-QCD results of Ref. [103] (turquoise points). Lower panel: the EoS $P(e)$ resulting from the matching of HRG with lattice-QCD results, in the CE (in black) and PCE (in red) cases. The matching has been performed at the temperature $T = 150$ MeV.*

multiplicity" of stable hadrons h ($\pi, K, \eta, N, \Lambda, \Sigma, \Xi$ and Ω)

$$\overline{n}_h = n_h + \sum_{r \neq h} n_r \langle N_h^r \rangle, \tag{2.9}$$

where $\langle N_h^r \rangle$ represents the average number of hadrons h coming from the decay of resonance r. Furthermore the multiplicity of resonance r is fixed by the chemical potential $\mu_r \equiv \sum_h \langle N_h^r \rangle \mu_h$. Assuming an isoentropic expansion of the fireball, PCE is set fixing at each temperature the chemical potentials μ_h in order to to satisfy the relation

$$\frac{\overline{n}_h(T, \{\mu_{h'}\})}{s(T, \{\mu_{h'}\})} = \frac{\overline{n}_h(T_c, \{\mu_{h'} = 0\})}{s(T_c, \{\mu_{h'} = 0\})}, \tag{2.10}$$

which amounts to the conservation of the entropy per (effective) particle throughout the medium evolution. Both in the CE and in the PCE case the transition from the lattice-QCD to the HRG description is performed at the temperature $T = 150$ MeV where the matching looks sufficiently smooth: results for the EoS are displayed in Fig. 2.4. A tabulation of the HRG+lQCD EoS in the PCE case is also part of the ECHO-QGP code.

Finally, we set the acronyms for the different equations of state currently implemented in ECHO-QGP. The ideal ultrarelativistic $P = e/3$ EoS will be labeled henceforth as EoS-I, and will be used mainly for testing purposes. The EoS computed by Laine and Schröder [102] will be termed as EoS-LS. The one with HRG+Lattice with CE (HRG+LAT+CE) will be termed as EoS-CE, while the analogue one with partial chemical equilibrium will be labeled as EoS-PCE.

2.3 Decoupling stage

Before illustrating results from ECHO-QGP of physical interest for heavy-ion collisions, it is mandatory to implement a routine accounting for the transition from the fluid description to the final hadronic observables to compare with the data and other authors' results.

The process of decoupling of hadrons from the fireball and their subsequent propagation in space-time is very complex and there are different recipes to model it. The most used scheme is based on the notion of freeze-out. Since the particle mean free paths strongly depend on the temperature of the medium one can assume that below a certain temperature T_{freeze}

particles stop interacting within the fireball and they propagate as free streaming particles. This is the so called kinetic freeze out and corresponds to the end of the hydrodynamical evolution of the system. In this scheme the hadron spectra are calculated using the Cooper-Frye prescription [104]: from the temperature profiles obtained within the hydrodynamic simulation one first determines the hypersurface Σ of constant temperature $T = T_{\rm freeze}$ and the total emission of primary particles is then calculated as a sum of the thermal emission of cells lying on the freeze out hypersurface. Corrections to the particle spectra related to the decay of unstable particles have been shown to be significant and they must be included to reproduce the experimental data [29, 105, 106].

In the last years, hybrid approaches have been proposed in which the decoupling is treated as a switch, at a certain temperature T_{switch}, from a hydrodynamical description of the fireball to a particle transport description [30, 31, 58, 107–112]. In this procedure one does not need to introduce a freeze out hypersurface but a particlization algorithm is anyway required which maps the hydrodynamic simulation output into initial conditions for the transport code. For the sake of simplicity and for performing our first tests of ECHO-QGP, we adopt here the freeze out scheme and retain the hybrid approach as an important outlook of our work. Let us now briefly review the formalism used for calculating the particle spectra within the Cooper-Frye scheme. The momentum spectrum of hadrons of species i is written as (consistently with the [-,+,+,+] metric):

$$E\frac{d^3N_i}{dp^3} = \frac{d^3N_i}{dy p_T dp_T d\phi} = \frac{g_i}{(2\pi)^3}\int_\Sigma \frac{-p^\mu d^3\Sigma_\mu}{\exp\left[-\frac{u^\mu p_\mu + \mu_i}{T_{\rm freeze}}\right] \pm 1} \tag{2.11}$$

The index i refers to the hadron species such as pions, kaons, protons etc; g_i and μ_i are the corresponding degeneracy and chemical potential and finally p_μ is the four momentum of the particle.

An improvement to the pure kinetic freeze-out distinguishes between the temperature at which elastic interactions between particles cease, $T_{\rm freeze}$, and the chemical freeze out temperature $T_{\rm c}$ at which just the inelastic interactions cease. As explained before, below $T_{\rm c}$ a PCE equation of state is computed which allows to determine the chemical potentials μ_i of each "frozen particle" at decoupling. In fixing the yields of the individual hadrons we will employ the chemical potentials arising from such a procedure. In this work we will use the PCE equation of state and also the one presented in Ref. [14].

The use of Eq. (2.11) requires to evaluate the hypersurface Σ of constant

temperature. In 3+1D, determining such a surface is computationally quite demanding because of the many different possibilities in which the 3D hypersurface can intersect the 4D hypercubes of the hydrodynamical simulation grid [112]. Here we follow a simpler method also used in [58]: we can imagine the hypersurface to be the collection of the hypercubes' faces of those neighbours cells which are respectively above and below the threshold $T_{\rm freeze}$. In this case the $d^3\Sigma^\mu$ is composed by the sum (in Bjorken coordinates):

$$d^3\Sigma^\mu = \begin{pmatrix} dV_{\perp\tau} \\ dV_{\perp x} \\ dV_{\perp y} \\ dV_{\perp\eta} \end{pmatrix} = \begin{pmatrix} \tau\Delta x\Delta y\Delta\eta s^\tau \\ \tau\Delta y\Delta\eta\Delta\tau s^x \\ \tau\Delta\eta\Delta\tau\Delta x s^y \\ \frac{1}{\tau}\Delta\tau\Delta x\Delta y s^\eta \end{pmatrix} \tag{2.12}$$

where each volume element of the hypersurface is oriented by the vector

$$s^\mu = -\text{sign}\left(\frac{\partial T}{\partial x^\mu}\right) \tag{2.13}$$

In this way, we associate to each of these cells a normal unitary vector oriented toward the direction of negative temperature gradient.

In most cases only one of the components of $d^3\Sigma^\mu$ is different from zero, since the $dV^{\perp\mu}$ is added only if the freeze out condition is fulfilled. Let us label with T_A the temperature in an arbitrary cell, and T_B the temperature of its neighbour in the positive μ (with μ running over the four dimensions). As a first approximation, if

$$(T_A - T_{\rm freeze})(T_{\rm freeze} - T_B) > 0$$

then the hypersurface contains the element $dV^{\perp\mu}$ relative to those cells and direction μ. A more refined procedure that we here adopt is to construct a cell with values of temperature and four velocity interpolated between the cells A and B. This construction allows to compute the scalar product in the numerator of 2.11 at each hypersurface cell and could give a positive or negative contribution to the total spectrum depending on the orientation of the cell and the orientation of the four momentum of the particle.

Once the hypersurface is determined, one can calculate the spectra as functions of the four momentum p^μ which, in the Bjorken coordinates, reads

$$p^\mu = \left(m_{\rm T}\cosh\left(\mathrm{y} - \eta_s\right), p_{\rm T}\cos\phi, p_{\rm T}\sin\phi, \frac{m_{\rm T}}{\tau}\sinh\left(\mathrm{y} - \eta_s\right)\right), \tag{2.14}$$

where y is the particle rapidity, p_{T} is its transverse momentum and $m_{\mathrm{T}} = (p_{\mathrm{T}}^2 + m^2)^{1/2}$ is its transverse mass. Whithin this formalism, we can replace in formula 2.11:

$$\begin{aligned} -u^\mu p_\mu = u^\tau m_{\mathrm{T}} \cosh(\mathrm{y} - \eta_s) - u^x p_{\mathrm{T}} \cos\phi \\ - u^y p_{\mathrm{T}} \sin\phi - \tau^2 u^\eta \frac{m_{\mathrm{T}}}{\tau} \sinh(\mathrm{y} - \eta_s) \end{aligned} \tag{2.15}$$

and

$$\begin{aligned} -d^3\Sigma_\mu p^\mu = \Big[m_{\mathrm{T}} \cosh(\mathrm{y} - \eta_s)\, s^\tau \tau dx dy d\eta_s - p_{\mathrm{T}} \cos\phi\, s^x \tau d\tau dy d\eta_s \\ - p_{\mathrm{T}} \sin\phi\, s^y \tau d\tau dx d\eta_s - m_{\mathrm{T}} \sinh(\mathrm{y} - \eta_s)\, s^\eta d\tau dx dy \Big] \end{aligned} \tag{2.16}$$

The observables that will be considered in this work are the following: the transverse spectrum at midrapidity ($\mathrm{y} = 0$) averaged over ϕ

$$\frac{1}{2\pi} \int_0^{2\pi} \frac{d^3N_i}{p_{\mathrm{T}} dp_{\mathrm{T}} d\mathrm{y} d\phi}(\mathrm{y} = 0, p_{\mathrm{T}}, \phi) d\phi, \tag{2.17}$$

the elliptic flow coefficient v_2

$$v_{2(i)}(p_{\mathrm{T}}, \mathrm{y}) = \frac{\int_0^{2\pi} \frac{dN_i}{p_{\mathrm{T}} dp_{\mathrm{T}} d\phi d\mathrm{y}}(\mathrm{y}, p_{\mathrm{T}}, \phi)\, \cos(2\phi) d\phi}{\int_0^{2\pi} \frac{dN_i}{p_{\mathrm{T}} dp_{\mathrm{T}} d\phi d\mathrm{y}}(\mathrm{y}, p_{\mathrm{T}}, \phi)\, d\phi} \tag{2.18}$$

the rapidity spectrum

$$\frac{dN_i}{d\mathrm{y}} = \int_0^{2\pi} \int_0^{+\infty} \frac{d^3N_i}{p_{\mathrm{T}} dp_{\mathrm{T}} d\mathrm{y} d\phi}(\mathrm{y}, p_{\mathrm{T}}, \phi) d\phi\, p_{\mathrm{T}} dp_{\mathrm{T}} \tag{2.19}$$

and directed flow coefficient v_1 as a function of the particle rapidity

$$v_{1(i)}(\mathrm{y}) = \frac{\int_0^{2\pi} \int_0^{+\infty} \frac{dN_i}{p_{\mathrm{T}} dp_{\mathrm{T}} d\phi d\mathrm{y}}(\mathrm{y}, p_{\mathrm{T}}, \phi)\, \cos(\phi) d\phi\, p_{\mathrm{T}} dp_{\mathrm{T}}}{\frac{dN_i}{d\mathrm{y}}}. \tag{2.20}$$

2.3.1 Particle spectra in presence of dissipation

In the presence of finite viscosity coefficients η, and ζ, the thermal distribution functions for fermions and bosons employed in the Cooper-Frye formula is modified. Indicating with f_0 the ideal particle distribution employed in

the previous section, the modified distribution can be written as $f = f_0 + \delta f$, δf being the viscous correction. The deviation from equilibrium owing to the stress corrections from η, and ζ are taken in the following form [34,113],

$$\delta f = \frac{f_0(1 \mp f_0)}{2T^2(e+P)} \left[p_\mu p_\nu \pi^{\mu\nu} \right], \tag{2.21}$$

which are based on the relaxation time approximation[1].

Therefore, obtaining particle spectra in the presence of viscosities, we not only need the freezeout temperature, entropy density, and fluid four velocity at the freezeout, but also the components of viscous stress $\pi^{\mu\nu}$, and Π along the freeze-out surface. The results obtained for the elliptic flow, and spectra shall be presented and discussed in the next section.

2.3.2 Particles spectra

Since our procedure to determine the freeze-out surface is somehow simpler compared to the algorithms used within other 3+1D codes (see *e.g.* MUSIC's routine or CORNELIUS [49, 112]), it is essential to compare our results for the particles spectra with the results obtained using other codes. For the 2+1D case there are several available codes such as AZHYDRO [13, 14] (ideal RHD) and UVH2+1 [114] (viscous RHD). We present here comparisons with results obtained using AZHYDRO, in which a triangular mesh is determined to approximate the hypersurface. In particular, we have simulated the hydrodynamical stage of heavy-ion collisions with AZHYDRO and for the calculation of the spectra of primary particles at decoupling we have used the routines for the freeze-out included in AZHYDRO and the freeze-out routine of ECHO-QGP described above. Note that within AZHYDRO the particle distribution function is assumed to be a Maxwell distribution and the boost invariance allows to compute analytically the integral on the η variable in the Cooper Frye formula. Following this procedure, the integral on the η variable of Eq. (2.11) leads to modified Bessel functions. The parameter set used for AZHYDRO can be found in Tab. 2.1. In Figs. 2.5-2.6 we compare results for primary pions transverse momentum spectra and v_2 at several impact parameters. The agreement between our results and the ones obtained within AZHYDRO is quite satisfying for values of b which are relevant from the experimental point of view ($b \lesssim 6 - 7$ fm). For larger values, deviations of the order of

[1] the bulk viscosity contribution is still not implemented

σ_{nn} mb	τ_0 fm	e_0 Gev fm^{-3}	α	b fm	$T_{\rm freeze}$ GeV	μ_π GeV
40	0.6	24.5	1	0,3,6,9,12	0.0622	0.120

Table 2.1: *Parameter set used within AZHYDRO while testing the ECHO-QGP freeze out routine. The pion chemical potential is taken from [14]). The grid spacing here used is:*$\Delta x = \Delta y = 0.4fm$ $\Delta\tau = 0.16$ *fm.*

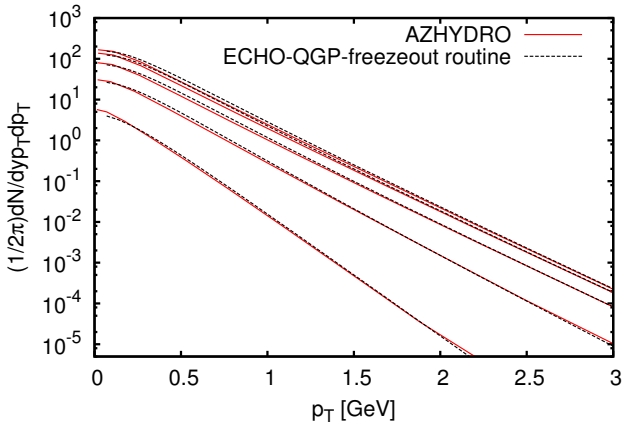

Figure 2.5: *Transverse momentum pion spectra at different values of impact parameters. From the top:* $b = 0, 3, 6, 9, 12$ *fm.*

20% are present in the v_2 spectra at low transverse momenta, $p_{\rm T} \sim 0.1$ GeV. Also in [49, 58] it has been remarked that, in spite of its simplicity, this method is sufficiently accurate for computing particle spectra and v_2.

The comparison between the ECHO-QGP and the AZHYDRO results for particle spectra in 2+1D presented earlier is a crucial test before extending our calculations to 3+1D. Having a good agreement with AZHYDRO, we can now use the ECHO-QGP 2+1D results as a benchmark for the 3+1D calculations. In order to perform this test we have used the initial conditions specified in Sec. II, for which the energy profile along the η direction is flat up to Δ_η and has then a smooth gaussian drop for larger values of η. In the transverse direction, the energy profile is the same for the 2+1D and the 3+1D simulations. The lack of boost invariance in 3+1D implies that the hydrodynamical quantities in Eq. (2.11) (temperature and four-velocity) depend on η and thus the integral on this variable must be calculated numerically. Also, the hypersurface depends now on η. The parameter set used for these tests of consistence between 3+1D and 2+1D

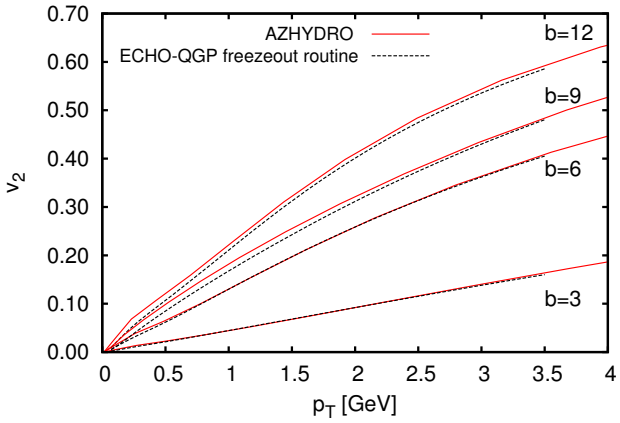

Figure 2.6: *Comparison of the p_T and b dependence of the pion elliptic flow coefficient v_2 computed within ECHO-QGP and AZHYDRO.*

descriptions, fully performed with ECHO-QGP, can be found in Table 2.2.

σ_{nn} mb	τ_0 fm	e_0 Gev fm^{-3}	α	b fm	T_{freeze} GeV	μ_π GeV
40	0.6	24.5	1	0	0.0622	0.120

Table 2.2: *Parameter set used in the comparison between 2+1D and 3+1D ECHO-QGP output, with different values of Δ_η and σ_η (see Fig. 2.7).*

As one can notice in Fig. 2.7, for $\Delta_\eta = 1$, $\sigma_\eta = 3$, $\Delta_\eta = 3$, $\sigma_\eta = 1$ the 3+1D results lie on top of the 2+1D ones apart from the region at low p_T, where in the last case the thermal distributions are approximated by Maxwell distributions in order to analytically perform the integral over η. The 2+1D spectrum is thus underestimated. For $\Delta_\eta = 1$ and $\sigma_\eta = 1$, on the other hand, the 3+1D curve is lower than the 2+1D one due to the lower extension of the flat region in the initial η_s-distribution.

In 3+1D, another interesting observable is the rapidity spectrum that we show in Fig. 2.8. Although we do not present here a comparison with experimental data, the dependence on y is qualitatively very similar to the one obtained, for instance, in [112], see their Fig. 21. At y = 0 these spectra represent just the integral of p_T of the transverse momentum spectra of Fig. 2.8, and we have obtained, consistently, that the $\Delta_\eta = 1$ and $\sigma_\eta = 3$ and $\Delta_\eta = 3$ and $\sigma_\eta = 1$ cases provide the same result while for $\Delta_\eta = 1$ and $\sigma_\eta = 1$ a lower value of the spectrum is obtained. As y is shifted, one

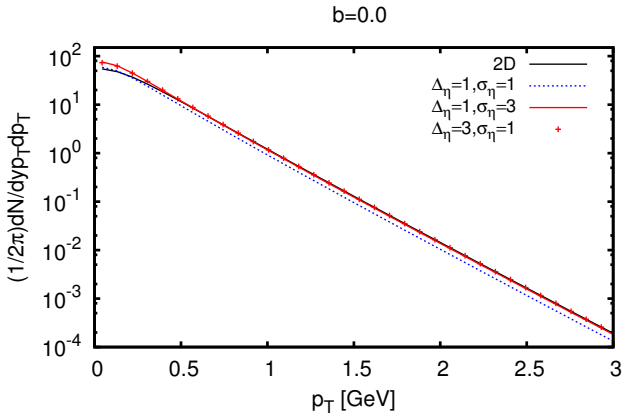

Figure 2.7: *Comparison of the pion transverse momentum spectra obtained by ECHO-QGP in 2+1D and 3+1D for different parametrizations of the initial energy density profile in space-time rapidity.*

probes the tails of the freeze-out hypersurface along the η direction. Thus the larger the value of σ_η the harder is the spectrum (see the curves corresponding to $\Delta_\eta = 3$, $\sigma_\eta = 1$ and $\Delta_\eta = 1$ and $\sigma_\eta = 3$). For a comparison with the experimental data, such as the ones of the PHOBOS collaboration, we need to include the contribution of unstable particles on the final pion spectra.

σ_{nn} mb	τ_0 fm	e_0 Gev fm^{-3}	α	b fm	μ_π GeV	T_{freeze} GeV
40	1.0	30.0	0.15	3,5,7	0.03217	0.130

Table 2.3: *Parameter set used in the 2+1D ideal and viscous ($\eta/s = 0.08$) simulations (see Fig. 2.11a)*

In this work such contributions are not implemented. In fig. 2.9a we display the transverse momentum spectra of (direct) pions, kaons and protons. For large values of p_T our results are compatible with results obtained in the 3+1D code developed in [49] (see their Fig. 1) where also a fit of the experimental data is presented. A value of the pion spectrum of about 0.1 GeV^{-2} at $p_\mathrm{T} \sim 2$ GeV. The agreement with [49] is lost at low p_T due to lack of resonance feed-down in our scheme. Indeed in [106] an enhancement of a factor of 4 is obtained for the pion spectra at $p_\mathrm{T} = 0$. We are thus confident that including the resonances decays will allow to

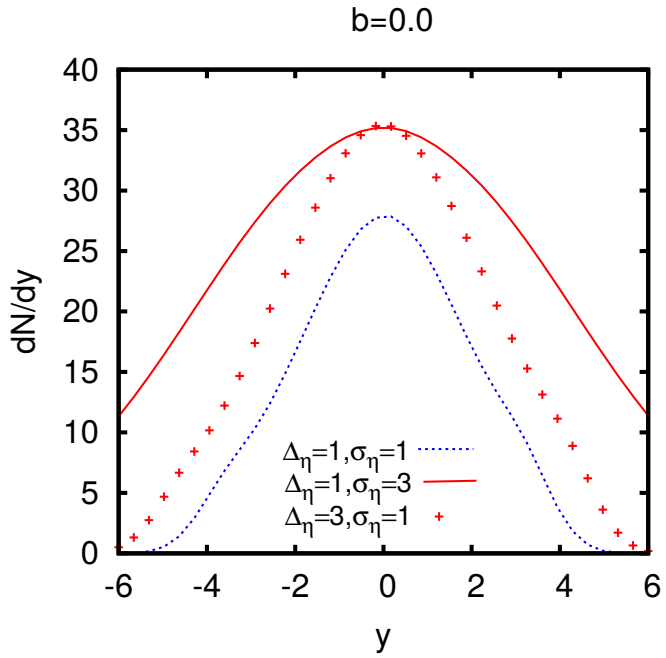

Figure 2.8: *Pion rapidity spectra with different parametrizations of the initial energy density profile in space-time rapidity.*

correctly reproduce the experimental data. On the other hand, the elliptic flow results are not so much affected by the resonance feed-down because it is a ratio of spectra. Considering for instance the pion v_2 , we obtain a value of ~ 0.19 at $p_{\mathrm{T}} = 1.5$ GeV and $b = 7$ fm from Fig. 2.8, which is consistent with results obtained in [49] (see Fig. 7 therein). In 2.10, we show the rapidity spectra of pions, kaons and protons. This observable will be important for future developments of ECHO-QGP when comparing with the experimental data. In particular, it will allow one to better constrain the initial conditions of the hydrodynamical evolution.

Viscosity provides important corrections to the particle spectra particularly evident in the p_{T} and b dependence of the elliptic flow coefficient v_2. As first approach, we limited our discussion to 2+1D simulations with the parameters of Table 2.3, neglecting viscous corrections to the particle distributions in the Cooper-Frye algorithm; after this stage we included the contribution to the particle distribution function given by the shear stress tensor (see Eq. 2.21). As shown in Fig. 2.11, we obtain the standard result of a suppression of the v_2 when including viscosity. At $p_{\mathrm{T}} = 1.5$ GeV, $\eta/s = 0.08$ and $b = 7.0$ fm, the suppression is of the v_2 of the order

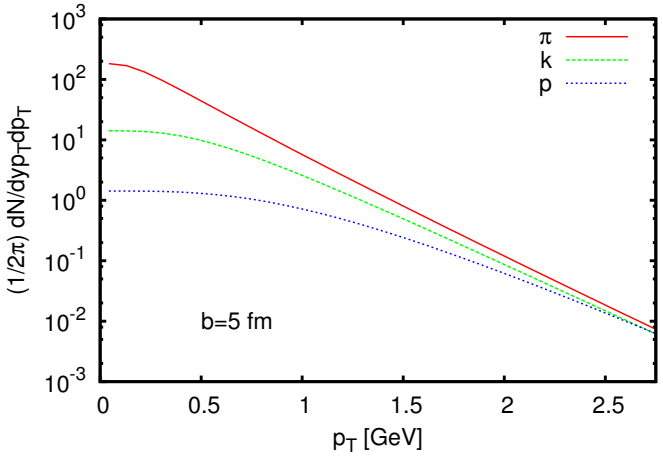

(a)

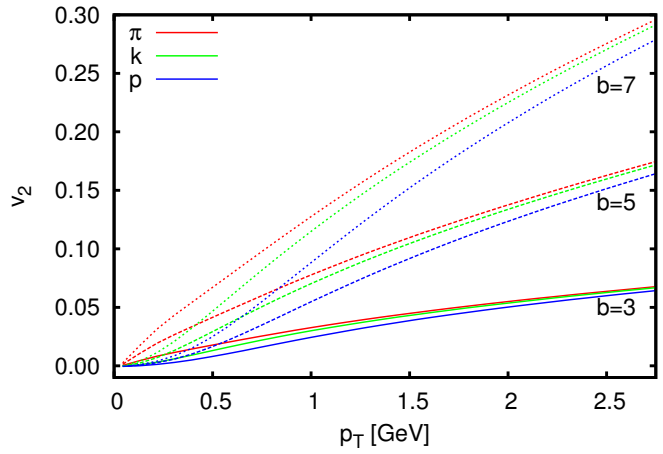

(b)

Figure 2.9: *Panel (a) p_{T} spectra of pions, kaons and protons as obtained in 3+1D ideal hydrodynamics. Panel (b) p_{T} and b dependence of the elliptic flow v_2 as obtained in 3+1D ideal hydrodynamics.*
Parameters are specified in Tab. 2.2. The grid steps are $\Delta x = \Delta y = 0.2$ fm $\Delta\eta_s = 0.2, \Delta\tau = 0.1$ fm/c.

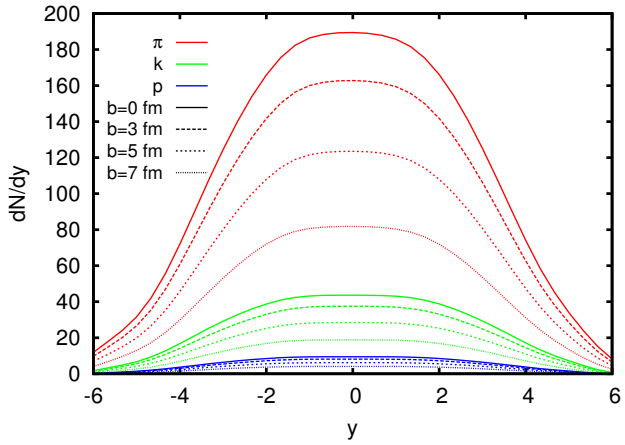

Figure 2.10: *Rapidity spectra of pions, kaons and protons as obtained in 3+1D ideal hydrodynamics.*

of 10%, which is in agreement with [69] (see Fig. 10) and [35, 113, 115, 116], and when including also the corrections to the distribution function a suppression of about 15% is reached. Finally, in Fig. 2.12 we display results for the transverse momentum spectra of pions kaons and protons with $b = 5$ fm. The effect of the viscosity is qualitatively consistent with previous results [117]: up to $p_{\rm T} \sim 1$ GeV spectra are slightly suppressed with respect to the ideal case and at larger $p_{\rm T}$ are instead enhanced (almost doubled at $p_{\rm T} \sim 2$ GeV). This enhancement with large $p_{\rm T}$ is due to the growth of the transverse expansion in presence of viscosity compared to the ideal case.

2.4 Temperature and Eccentricity evolution

We start considering the time evolution of the central temperature $T(\tau)$ (obtained from the local energy density through the EOS) both for central ($b = 0$) and non-central ($b \neq 0$) Au-Au collisions with RHIC-type initial conditions. We assume 2+1D evolution. Simulations are performed in Bjorken coordinates with a grid size in the transverse $(x - y)$ plane of 201×201 cells and physical dimensions ranging from -20 fm to 20 fm. For 3+1D runs we use 101×101 cells ranging from -20 fm to 20 fm in the transverse plane, and 151 point along η_s, going from -11 to 11 fm.

The dependence of $T(\tau)$ on the EOS, on the impact parameter and on the shear viscosity is displayed in Fig. 2.13. The temperature is sensitive to the equations of the state chosen throughout the evolution. As

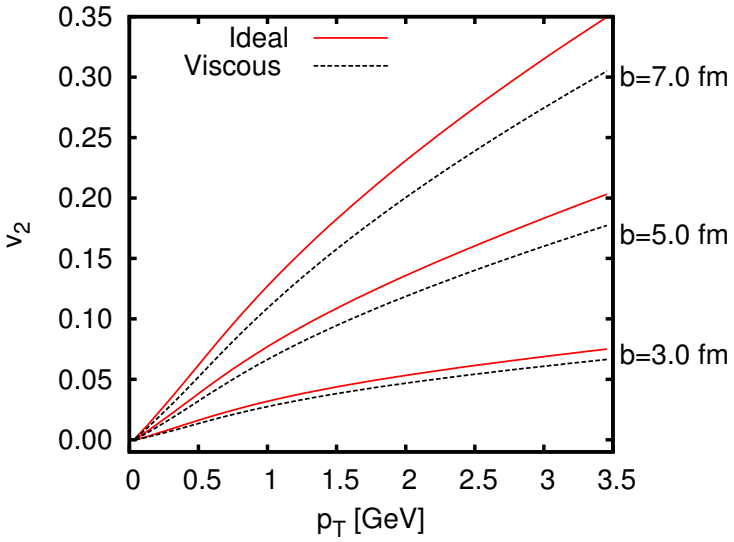

(a)

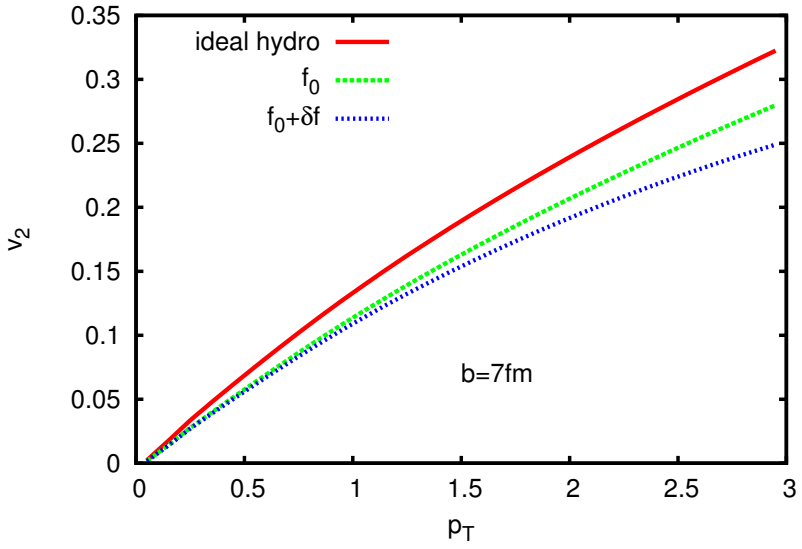

(b)

Figure 2.11: *Panel (a): p_{T} and b dependence of the pion elliptic flow coefficient v_2 within 2+1D ideal and viscous hydrodynamics. Panel (b): p_{T} dependence of the pion elliptic flow coefficient v_2, within 3+1D ideal (red solid line) and viscous hydrodynamics, with the explicit contribution given by the viscous correction in the hydrodynamic phase (green dashed line), and addition of the correction δf to the distribution function (blue dotted line)*

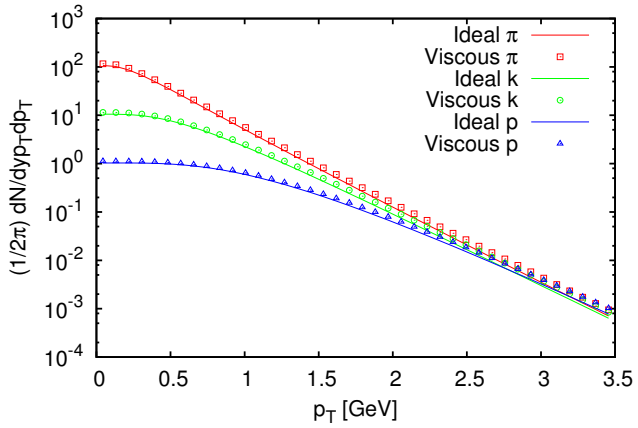

Figure 2.12: *$p_{\rm T}$ spectra for pions, kaons and protons. Comparison between results obtained in 2+1D ideal (sold lines) and viscous (dotted lines) hydrodynamics. Here $b = 5$ fm.*

expected, the differences are more pronounced in the later stages, when the temperature drops below $T = 150$ MeV and the effects of the partial chemical equilibration plays crucial role. Concerning the dependence on the shear viscosity, we notice that its effect is very limited in the central region, where the fluid velocity is small. More important is the dependence on the impact parameter. It is clear that the larger the value of b, the earlier the occurrence of freeze-out. This is mainly guided by the impact parameter dependence of the initial energy density profile.

We then move to consider the evolution of the eccentricity in non-central collisions. Hydrodynamics translates the initial spatial eccentricity of the system – arising essentially from the non-vanishing impact parameter of the A-A collision and giving rise to asymmetric pressure gradients – into a final anisotropy in the momentum spectra of the produced hadrons. The spatial anisotropy in the transverse plane is usually quantified, in the case of smooth initial conditions, in terms of the coefficient [118]

$$e_x = \frac{\langle y^2 - x^2 \rangle_e}{\langle y^2 + x^2 \rangle_e} \tag{2.22}$$

where $\langle \dots \rangle_e$ denotes a spatial average over the transverse plane, with the local energy-density e (or entropy density s, depending on the choice done in the initialization stage) as a weight. The momentum anisotropy is

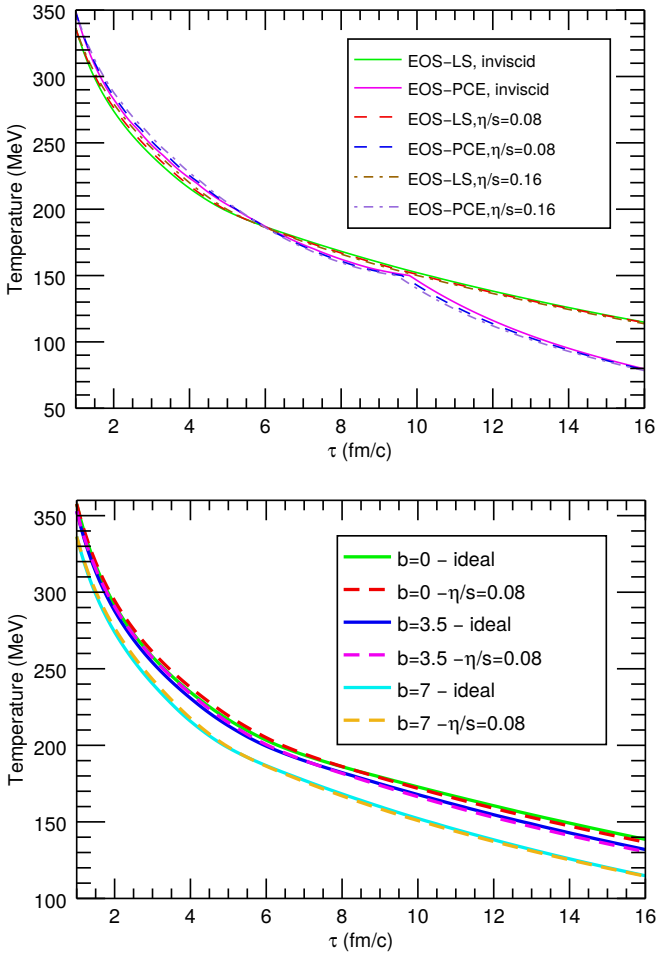

Figure 2.13: *Temperature as a function of τ at the center of the fireball with RHIC-type initial conditions.*
Upper Panel: we compare EOS-LS against EOS-PCE, and ideal RHD against viscous runs with $\eta/s = 0.08$, or 0.16 for $b = 7$ fm.
Lower panel: we study the influence of shear viscosity (η/s =0.08) against ideal RHD for $b = 0$, $b = 3.5$ fm, and b $b =$ fm.

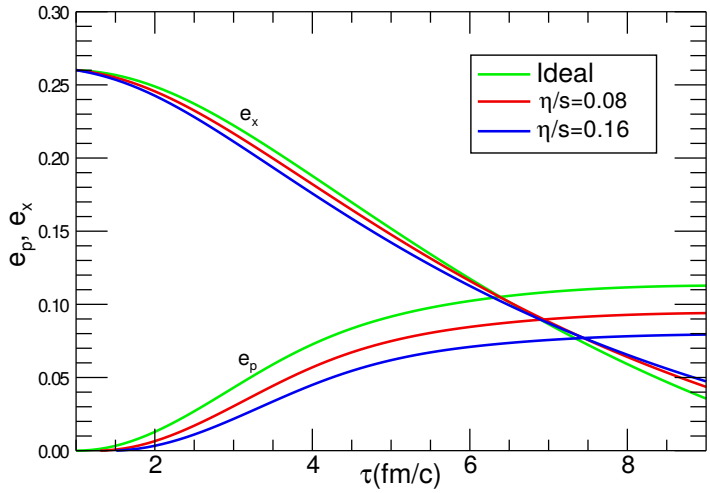

Figure 2.14: *Spatial anisotropy ex and momentum anisotropy e_p as a function of τ in RHIC-type 2+1D simulations with ECHO-QGP, using EOS-LS. We compare runs with $b = 7$ fm and for $\eta/s = 0$, 0.08, 0.16*

estimated, following [119], in terms of the components of T , as

$$e_p = \frac{\langle T^{xx} - T^{yy} \rangle_e}{\langle T^{xx} + T^{yy} \rangle_e} \tag{2.23}$$

where $\langle \dots \rangle$ denotes a spatial averaging (over the transverse plane) with weight factor unity.

Because of the larger pressure gradients along the reaction-plane, during the hydrodynamic evolution of the system the momentum anisotropy e_p is expected to increase at the expense of the spatial eccentricity e_x. The temporal evolution of e_x and e_p at RHIC, along with their sensitivity to the EOS and the magnitude of the viscous effects, are shown in Fig. 2.14 for $b = 7$ fm in 2+1D. We can observe that, with higher values of η/s, the growth of the momentum anisotropy is lower throughout the time evolution, reflecting the role of dissipative effects in taming the collective response of the system to the pressure gradients. Next, we consider the sensitivity of e_x and e_p to the EOSs employed and the impact parameter. The time evolution of the spatial and momentum anisotropies is shown, for $b = 3$ fm and $b = 7$ fm, with EOS-I, EOS-LS and EOS-PCE, with and without shear viscosity (here we have switched off the bulk viscous effects), in Fig. 2.15. Both the spatial and momentum anisotropies are quite sensitive to the EOS employed in the simulations. The differences among the various setups can be observed at the later stages of the collisions both at $b = 3$ fm

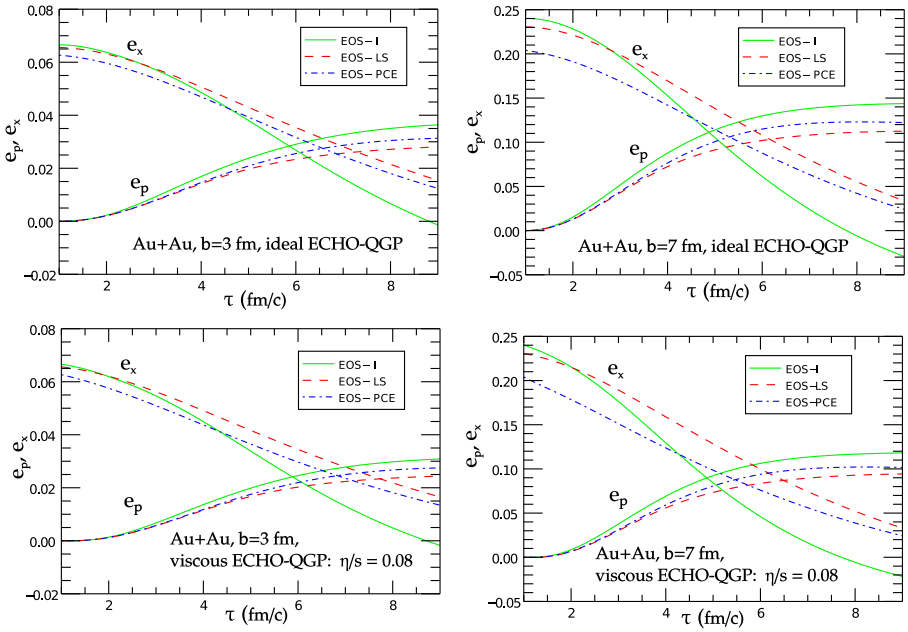

Figure 2.15: *Spatial and momentum anisotropies for different EOSs and impact parameters employed in 2+1D simulations. The ideal case (the viscous case with $\eta/s = 0.08$) is shown in top (bottom) panels.*

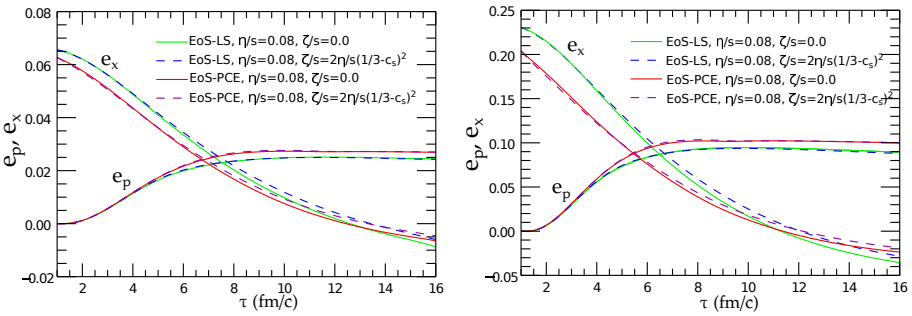

Figure 2.16: *Spatial and momentum anisotropies for different values of the η/s and ζ/s parameters, for $b = 3$ and $b = 7$ fm, and with EOS-LS or EOS-PCE.*

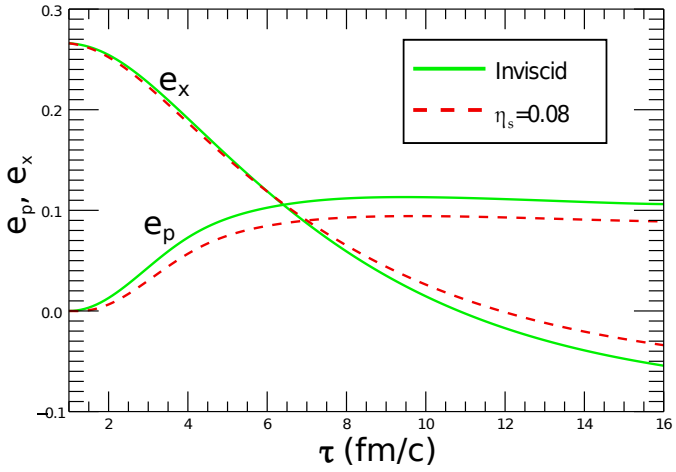

Figure 2.17: *Spatial anisotropy e_x and momentum anisotropy e_p as a function of τ in RHIC-type 3+1D simulations, using EOS-LS. We compare runs with $b = 7$ fm and for $\eta/s = 0$ 0 and 0.08 in the plane with $\eta_s = 0$ space-time rapidity.*

and at $b = 7$ fm. Differences are more pronounced for the more peripheral collisions. All these observations still hold in the presence of viscosity.

We now investigate the role of bulk viscosity as far as the time evolutions of e_p and e_x is concerned. We have plotted e_x and e_p at $b = 3$ fm and $b = 7$ fm with and without ζ/s for two of the tabulated equations of state, EOS-LS and EOS-PCE in Fig. 2.16. In both cases, we set $\eta/s = 0.08$. The value of ζ/s is set to $2\eta/s(1/3 - c_s^2)$. We observe that the non-vanishing ζ/s has a negligible impact at the initial times as compared to role played by η/s. There are some mild effects seen at lower temperatures (later stages of the evolution). This is not surprising, since the temperature behavior ζ/s is governed by the factor $1/3 - c_s^2$. All the above observations are valid for both EOS-LS and EOS-PCE.

Finally, also 3+1D simulations, with the same set up (RHIC-type initialization with $b = 7$ fm, EOS-LS, Bjorken coordinates), have been performed. Expansion now occurs also in the η_s direction, as expected, and in Fig. 2.17 we show the time evolution of the e_x and e_p quantities calculated at $\eta_s = 0$, for both the ideal case and the viscous one, with $\eta/s = 0.08$. The behavior is similar to the corresponding 2+1D case, and different cuts in the space-time rapidity η_s also produce similar results. We have found that in some cases the expanding front along η_s shows instabilities in 3+1D viscous runs (only for Bjorken coordinates). To cure this problem, we adopt a similar strategy as in [39], where viscous tensor

components (and the bulk viscous pressure) are decreased proportionally to P/P_{cut} when $P < P_{cut}$, where the assumed threshold corresponds to a temperature $T \simeq 45$ MeV (for the chosen EOS-LS), well below the freeze-out limit.

3

A study of vorticity formation in Heavy-ion collisions

An interesting issue to be studied in heavy-ion collisions at ultrarelativistic energies, is the possible formation of vorticity in peripheral collisions [120–122]. Hydrodynamics is a theoretical frame in which vorticity is easily treated and indeed, its presence may provide information about the (mean) initial state of the hydrodynamical evolution which cannot be achieved otherwise. Vorticity is also related to the onset of interesting new physics in the plasma at high temperature, such as the chiral vortical effect [123]. Furthermore, it has been shown that vorticity gives rise to polarization of particles in the final state, so that e.g. Λ baryon polarization - if measurable - can be used to detect it [124, 125]. Finally, as shown in [126], numerical calculations of vorticity can be used to make stringent tests of numerical codes, as the T-vorticity (see sect. *3.1* for the definition) which is expected to vanish throughout under special initial conditions in the ideal case.

Vorticity has been recently the subject of investigations in refs. [121, 122] with specific initial conditions in cartesian coordinates, ideal fluid approximation and isochronous freeze-out. Instead, in [126], different kinds of vorticity have been calculated with ECHO-QGP [85] including dissipative relativistic hydrodynamics in the Israel-Stewart formulation with Bjorken initial conditions, henceforth denoted as BIC. It should be pointed out from the very beginning that the purpose of this chapter is to make a general assessment of vorticity at top RHIC energy and not to provide a precision fit to all the available data. Therefore, the calculations do not take into

account effects such as initial state fluctuations, viscous corrections to particle distribution at the freezeout and resonance feed-down.

3.1 Vorticities in relativistic hydrodynamics

Unlike in classical hydrodynamics, where vorticity is the curl of the velocity field $\mathbf{v}$, several vorticities can be defined in relativistic hydrodynamics which can be useful in different applications (see also the review [127]).

3.1.1 The kinematical vorticity

This is defined as[1]:

$$\omega_{\mu\nu} = \frac{1}{2}(d_\nu u_\mu - d_\mu u_\nu) = \frac{1}{2}(\partial_\nu u_\mu - \partial_\mu u_\nu)$$

where u is the four-velocity field. This tensor includes both the acceleration A_μ and the relativistic extension of the angular velocity pseudo-vector ω_μ in the usual decomposition of an antisymmetric tensor field into a polar and pseudo-vector fields:

$$\begin{aligned} \omega_{\mu\nu} &= \epsilon_{\mu\nu\rho\sigma}\omega^\rho u^\sigma + \frac{1}{2}(A_\mu u_\nu - A_\nu u_\mu) \\ A_\mu &= 2\omega_{\mu\nu}u^\nu = u^\nu d_\nu u_\mu = Du_\mu \\ \omega_\mu &= -\frac{1}{2}\epsilon_{\mu\rho\sigma\tau}\omega^{\rho\sigma}u^\tau \end{aligned} \tag{3.1}$$

Using of the transverse (to u) projector 1.4 and the usual definition of the orthogonal derivative (see 1.10):

$$\nabla_\mu = \Delta^\alpha_\mu d_\alpha = d_\mu + u_\mu D.$$

It is convenient to define also a **transverse kinematical vorticity** as:

$$\omega^\Delta_{\mu\nu} = \Delta_{\mu\rho}\Delta_{\nu\sigma}\omega^{\rho\sigma} = \frac{1}{2}(\nabla_\nu u_\mu - \nabla_\mu u_\nu) \tag{3.2}$$

Using the above definition in the decomposition (3.1) it can be shown that:

$$\omega^\Delta_{\mu\nu} = \epsilon_{\mu\nu\rho\sigma}\omega^\rho u^\sigma$$

[1] notice that this is still true in Milne coordinates

that is ω^{Δ} is the tensor formed with the angular velocity vector only. As shown in the next subsection, only ω^{Δ} shares the "conservation" property of the classical vorticity for an ideal barotropic fluid.

3.1.2 The T-vorticity

This is defined as:

$$\Omega_{\mu\nu} = \frac{1}{2}\left[\partial_\nu(Tu_\mu) - \partial_\mu(Tu_\nu)\right] \tag{3.3}$$

and it is particularly useful for a relativistic uncharged fluid, such as the QCD plasma formed in nuclear collisions at very high energy. This is because from the basic thermodynamic relations when the temperature is the only independent thermodynamic variable, the relativistic equation of motion $(\varepsilon + p)A_\mu = \nabla_\mu p$ can be recast in the simple form (see e.g. [128] and references therein):

$$u^\mu \Omega_{\mu\nu} = \frac{1}{2}(TA_\nu - \nabla_\nu T) = 0 \tag{3.4}$$

The above (3.4) is also known as Carter-Lichnerowicz equation [127] for an uncharged fluid and it entails conservation properties which do not hold for the kinematical vorticity.

We are gong to show that the T-vorticity has the same property as the classical vorticity for an ideal barotropic fluid.

This can be better seen in the the language of differential forms, rewriting the definition of the T-vorticity as the **exterior derivative** of the 1-form Tu, that is:

$$\Omega = \mathbf{d}(Tu) \tag{3.5}$$

We know from the *Cartan identity* that the Lie derivative along the vector field u of Ω can be written as

$$\mathcal{L}_u(\Omega) = u \cdot \mathbf{d}\Omega + \mathbf{d}(u \cdot \Omega). \tag{3.6}$$

By using eq. (3.4) and the fact that the exterior derivative is nilpotent $(\mathbf{dd}(Tu) = 0)$, we derive

$$\mathcal{L}_u(\Omega) = 0 \tag{3.7}$$

Eq. (3.7) establishes that the *T-vorticity is conserved along the flow* and, thus, if it vanishes at an initial time it will remain null at all times. This

can be made better explained by expanding the Lie derivative definition in components:

$$(\mathcal{L}_u\Omega)^{\mu\nu} = D\Omega^{\mu\nu} - \partial_\sigma u^\mu \Omega^{\sigma\nu} - \partial_\sigma u^\nu \Omega^{\sigma\mu} = 0 \tag{3.8}$$

The above equation is in fact a differential equation for Ω precisely showing that if $\Omega = 0$ at the initial time then $\Omega \equiv 0$ always. Thereby, the T-vorticity has the same property as the classical vorticity for an ideal barotropic fluid (Kelvin circulation theorem).

The relation between T-vorticity and kinematical vorticity can be retrieved by expanding the definition (3.3):

$$\Omega_{\mu\nu} = \frac{1}{2}\left[(\partial_\nu T)\, u_\mu - (\partial_\mu T)\, u_\nu\right] + T\omega_{\mu\nu}$$

implying that the double-transverse projection of Ω:

$$\Delta_{\mu\rho}\Delta_{\nu\sigma}\Omega^{\rho\sigma} \equiv \Omega^\Delta_{\mu\nu} = T\omega^\Delta_{\mu\nu}$$

Hence, the tensor ω^Δ shares the same conservation properties of Ω^Δ, namely it vanishes at all times if it is vanishing at the initial time. Conversely, the mixed projection of the kinematical vorticity:

$$u^\rho \omega_{\rho\sigma}\Delta^{\sigma\nu} = \frac{1}{2}A_\sigma$$

does not. It then follows that for an ideal uncharged fluid with $\omega^\Delta = 0$ at the initial time, the kinematical vorticity is simply:

$$\omega_{\mu\nu} = \frac{1}{2}(A_\mu u_\nu - A_\nu u_\mu) \tag{3.9}$$

3.1.3 The thermal vorticity

This is defined as [125]:

$$\varpi_{\mu\nu} = \frac{1}{2}(\partial_\nu \beta_\mu - \partial_\mu \beta_\nu) \tag{3.10}$$

where $\beta_\mu = (1/T)u_\mu$ is the temperature four vector. This vector is defined as $(1/T)u$ once a four-velocity u, i.e. a hydrodynamical description, is introduced, but it can also be taken as a primordial quantity which allows to define a velocity through $u \equiv \beta/\sqrt{\beta^2}$ [129].

The thermal vorticity features two important properties: it is dimen-

sionless in natural units[2] and it is the actual constant vorticity at the global equilibrium with rotation [130] for a relativistic system, where β is a Killing vector field whose expression in Minkowski spacetime is

$$\beta_\mu = b_\mu + \varpi_{\mu\nu} x^\nu$$

being b and ϖ constant. In this case the magnitude of thermal vorticity is - with the natural constants restored - simply $\hbar\omega/KT$ where ω is a constant angular velocity. In general, (replacing ω with the classical vorticity defined as the curl of a proper velocity field) it can be readily realized that the thermal vorticity is a tiny number for most hydrodynamical systems, though it can be significant for the plasma formed in relativistic nuclear collisions.

Furthermore, the thermal vorticity is responsible for the local polarization of particles in the fluid according to the formula [124]:

$$\Pi_\mu(x,p) = -\frac{1}{8}\epsilon_{\mu\rho\sigma\tau}(1-n_F)\ \varpi^{\rho\sigma}\frac{p^\tau}{m} \tag{3.11}$$

which applies to spin 1/2 fermions, n_F being the Fermi-Dirac-Juttner distribution function.

$$n_F = \frac{1}{\mathrm{e}^{-(\beta(x)\cdot p+\mu)/T}+1} \tag{3.12}$$

Similarly to the previous subsection, the relation between T-vorticity and thermal vorticity can be written as:

$$\varpi_{\mu\nu} = \frac{1}{2T^2}\left[(\partial_\mu T)\,u_\nu - (\partial_\nu T)\,u_\mu\right] + \frac{1}{T^2}\Omega_{\mu\nu} \tag{3.13}$$

Again, the double transverse projection of ϖ is proportional to the one of Ω:

$$\Delta_{\mu\rho}\Delta_{\nu\sigma}\varpi^{\rho\sigma} \equiv \varpi^\Delta_{\mu\nu} = \frac{1}{T^2}\Omega^\Delta_{\mu\nu} = \frac{1}{T}\omega^\Delta$$

whereas the mixed projection turns out to be, by using the relation (3.13)

$$u^\rho \varpi_{\rho\sigma}\Delta^{\sigma\nu} = \frac{1}{2T^2}\nabla^\nu T + \frac{A^\nu}{2T}$$

Again, for an ideal uncharged fluid with $\omega^\Delta = 0$ at the initial time, by using the equations of motion (3.4), one has the above projection is just

[2] in Minkowskian Coordinates

A^ν/T and that the thermal vorticity is simply:

$$\varpi_{\mu\nu} = \frac{1}{T}(A_\mu u_\nu - A_\nu u_\mu) \tag{3.14}$$

A common feature of the kinematical and thermal vorticity is that their purely spacial components can be non-vanishing if the acceleration and velocity field are non-parallel, even though velocity is vanishing at the beginning.

3.2 Vorticity in high energy nuclear collisions

In nuclear collisions at very large energy, the QCD plasma is an almost uncharged fluid. Therefore, according to previous section's arguments, in the ideal fluid approximation, if the transversely projected vorticity tensor ω^Δ initially vanishes, so will the transverse projection Ω^Δ and ϖ^Δ and the kinematical and thermal vorticities will be given by the formulae (3.9) and (3.14) respectively. Indeed, the T-vorticity Ω will vanish throughout because also its longitudinal projection vanishes according to eq. (3.4). This is precisely what happens for the usually assumed BIC for the flow at τ_0, that is $u^x = u^y = u^\eta = 0$, where one has $\omega^\Delta = 0$ at the beginning as it can be readily realized from the definition (*3.1.1*). On the other hand, for a viscous uncharged fluid, transverse vorticities can develop even if they are zero at the beginning.

It should be noted though, that even if the space-space components (x, y, η indices) of the kinematical vorticity tensor vanish at the initial Bjorken time τ_0, they can develop at later times, even for an ideal fluid, if the spatial components of the acceleration and velocity fields are not parallel, according to eq. (3.9). The equation makes it clear that the onset of spatial components of the vorticity is indeed a relativistic effect as, with the proper dimensions, it goes like $(\mathbf{a} \times \mathbf{v})/c^2$.

Let us consider the full longitudinally boost invariant Bjorken picture, that is $u^\eta = 0$ throughout the fluid evolution. In the ideal case, as $\omega^\Delta = 0$, the only non-vanishing components of the kinematical vorticity are $\omega^{\tau x}, \omega^{\tau y}$ and ω^{xy}. At $\eta = 0$ the latter can be different from zero; but, because of the reflection symmetry in both the x and y axes (see fig. 3.1), it ought to change sign by moving clockwise (or counterclockwise) to the neighbouring

quadrant of the $x-y$ plane. For central collisions instead, it simply vanishes.

However, in the viscous case, more components of the vorticities can be non-vanishing. Furthermore, in more realistic 3+1 D hydrodynamical calculations, a non-vanishing u^η can develop because of the asymmetries of the initial energy density in the $x-\eta$ and $y-\eta$ planes at finite impact parameter. The asymmetry is essential to reproduce the observed directed flow coefficient $v_1(y)$ in a 3+1D ideal hydrodynamic calculation with BIC, as shown by Bozek [131], and gives the plasma a total angular momentum, as it will be discussed later on.

In this chapter, we calculate the vorticities, and especially the thermal vorticity ϖ by using basically the same parametrization of the initial conditions in ref. [131]. Those initial conditions are a modification of the BIC to take into account that the plasma, in peripheral collisions, has a relatively large angular momentum (see Appendix A). They are a minimal modifications of the BIC in that the initial flow velocity Bjorken components are still zero, but the energy density longitudinal profile is changed and no longer symmetric by the reflection $\eta \to -\eta$. They are summarized hereinafter. Given the usual thickness function expression (see equation 2.3) we set for this calculation $\rho_0 = 0.1693\,\mathrm{fm}^{-3}$, $\delta = 0.535\,\mathrm{fm}$ and $R = 6.38\,\mathrm{fm}$ [3]. Since we are dealing with colliding nuclei of the same kind, it is convenient to define the following functions:

$$n_1(\mathbf{x};b) = T_+\left(1-\left(1-\frac{\sigma^{NN}}{A}T_-\right)^A\right) \tag{3.15}$$

$$n_2(\mathbf{x};b) = T_-\left(1-\left(1-\frac{\sigma^{NN}}{A}T_+\right)^A\right) \tag{3.16}$$

(again σ^{NN} is the inelastic nucleon-nucleon cross section, A the mass number of the colliding nuclei), and:

$$T_+(\mathbf{x};b) = T\left(\mathbf{x}+\frac{\mathbf{b}}{2}\right) \qquad T_-(\mathbf{x};b) = T\left(\mathbf{x}-\frac{\mathbf{b}}{2}\right) \tag{3.17}$$

where, as in chapter 2, $\mathbf{x}$ is the vector of the transverse plane coordinates and $\mathbf{b}$ is the impact parameter vector, connecting the centers of the two nuclei.

In our conventional cartesian reference frame, the $\mathbf{b}$ vector is oriented along the positive x axis and the two nuclei have initial momentum along the

[3] the nuclear density, the width and the radius of the nuclear Fermi distribution respectively

z axis (whence the reaction plane is the xz plane) and their momenta are directed so as to make the initial total angular momentum oriented along the negative y axis (see fig. 3.1).

We recall also the definition of the mean number of binary collisions (see eq. 2.2):

$$n_{\text{coll}}(\mathbf{x};b) = \sigma^{NN} T_+(\mathbf{x};b)\, T_-(\mathbf{x};b) \quad (3.18)$$

For the purposes of this study we will change the definition of the wounded nucleons weight function given in 2.1, adding into it a dependence from the space-time rapidity, and we will call it W_N:

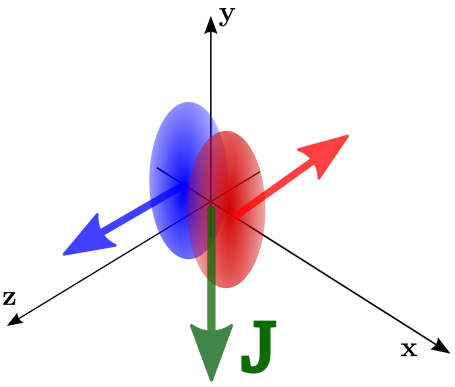

Figure 3.1: *Colliding nuclei and conventional cartesian reference frame. Also shown the initial angular momentum vector.*

$$W_N(\mathbf{x},\eta;b) = 2\ (n_1(\mathbf{x};b) f_-(\eta) + n_2(\mathbf{x};b) f_+(\eta_s)) \quad (3.19)$$

where:

$$f_-(\eta_s) = \begin{cases} 1 & \eta_s < -\eta_m \\ \dfrac{-\eta_s + \eta_m}{2\eta_m} & -\eta_m \le \eta_s \le \eta_m \\ 0 & \eta_s > \eta_m \end{cases}$$

and

$$f_+(\eta_s) = \begin{cases} 0 & \eta_s < -\eta_m \\ \dfrac{\eta_s + \eta_m}{2\eta_m} & -\eta_m \le \eta_s \le \eta_m \\ 1 & \eta_s > \eta_m \end{cases}$$

Finally, the initial proper energy density distribution is assumed to be:

$$\varepsilon = \varepsilon_0 \frac{\alpha\, n_{\text{coll}}(\mathbf{x};\mathbf{b}) H(\eta_s) + 2(1-\alpha) W_N(\mathbf{x},\eta_s;b)}{\alpha n_{\text{coll}}(\mathbf{0};0) + (1-\alpha) W_N(\mathbf{0},0;0)} \quad (3.20)$$

where we define:

$$H(\eta_s) = \exp\left(-\frac{\tilde{\eta}^2}{2\sigma_\eta^2}\theta(\eta_1)\right) \qquad \tilde{\eta} = |\eta_s| - \eta_{flat}/2 \quad (3.21)$$

We recall that α is the collision hardness parameter, which can vary between 0 and 1. Notice that in the denominator, the dependence from η_s of W_N is just formal: when we set $\eta_s = 0$ the function W_N assumes the value of n_{part} of equation 2.1. The parametrization (3.20) essentially respects

the causality constraint that the plasma cannot extend beyond $\eta = y_{\rm beam}$. Indeed, at $\sqrt{s}_{\rm NN} = 200$ GeV $y_{\rm beam} \simeq 5.36$ while the 3 σ point in the gaussian profile in Eq. (3.21) lies at $\eta = \eta_{\rm flat}/2 + 3\sigma_\eta \simeq 4.4$.

The free parameters have been chosen following ref. [132], where they were adjusted to reproduce the data in Au-Au collisions at $\sqrt{s}_{\rm NN} = 200$ GeV. We performed simulations within ECHO-QGP for both the ideal and

Parameter	Value
$\sqrt{s_{NN}}$	200 GeV
α	0.
ϵ_0	30 GeV/fm^3
σ_{in}	40 mb
τ_0	0.6 fm/c
η_{flat}	1
σ_η	1.3
T_{fo}	130 MeV
b	11.57fm
η_m ideal	3.36
η_m viscous	2.86
η/s	0.16

Table 3.1: *Parameters defining the initial configuration of the fluid in the Bjorken coordinates. The last two parameter values have been fixed for the last physical run.*

viscous modes with the parameters reported in table 3.1 and the equation of state reported in ref. [102]. The impact parameter value $b = 11.57$ was chosen as, in the optical Glauber model, it corresponds to the mean value of the 40-80% centrality class ($9.49 < b < 13.42$ fm [133]) used by the STAR experiment for the directed flow measurement [134]. The initial flow velocities u^x, u^y, u^η were set to zero, according to BIC. The freezeout hypersurface - isothermal at $T_{\rm FO} = 130$ MeV - is determined with the methods described in section *2.3* (and also in refs. [85, 135, 136]).

3.3 Vorticities in ECHO-QGP: novel tests

While in section *1.4* we showed that ECHO-QGP is well suited to model the evolution of the matter produced in heavy-ion collisions exploiting "canonical" tests, we must demonstrate the extension of its suitability to carry out the study on the development of vorticity. In such an environment,

we have performed two calculations, referring to an ideal and viscous scenario respectively, providing a very stringent numerical test.

Before describing these tests, it should be pointed out that the vorticities components must to be calculated in Bjorken coordinates, whose metric tensor is $g_{\mu\nu} = \mathrm{diag}(-1, 1, 1, \tau^2)$, hence they do not all have the same dimension nor they are adimensional as it is desirable (except the thermal vorticity, as it has been emphasized in Sect. *3.1*). For a proper comparison it is better to use the orthonormal basis, which involves a factor τ when the η components are considered. Moreover, the cumulative contribution of all components is well described by the invariant modulus, which, for a generic antisymmetric tensor $A_{\mu\nu}$ is:

$$A^2 = A_{\mu\nu}A^{\mu\nu} = 2[A_{xy}^2 - A_{\tau x}^2 - A_{\tau y}^2 + (A_{\eta x}^2 + A_{\eta y}^2 - A_{\eta\tau}^2)/\tau^2]. \quad (3.22)$$

Furthermore, we have always rescaled the T-vorticity by $1/T^2$ in order to have an adimensional number. Since the T-vorticity has always been determined at the isothermal freezeout, in order to get its actual magnitude, one just needs to multiply it by T_{FO}^2.

3.3.1 T-vorticity for an ideal fluid

Since the fluid is assumed to be uncharged and the initial T-vorticity Ω is vanishing with the BIC, it should be vanishing throughout, according to the

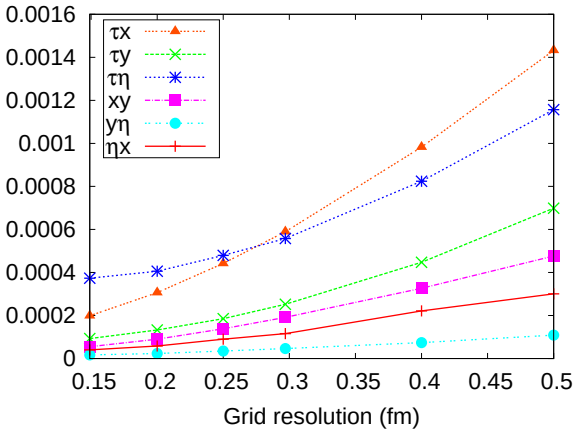

Figure 3.2: *Mean of the absolute value of T-vorticity components, divided by τT^2, at the freeze-out as a function of the grid resolution.*

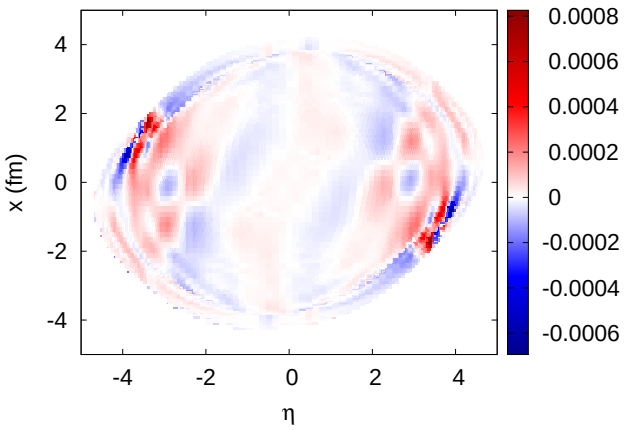

Figure 3.3: *Contour plot of $\Omega_{x\eta}/\tau T^2$ at the freeze-out hypersurface at $y = 0$.*

discussion in sect. *3.1*). However, the discretization of the hydrodynamical equations entails a numerical error, thus the smallness of Ω in an ideal run is a gauge of the quality of the computing method. In fig. 3.2 we show the mean of the absolute values of the six independent components, in Bjorken coordinates, of the T-vorticity divided by T^2 to make it adimensional, as a function of the grid resolution (the boundaries in x, y, η being fixed). It should be pointed out that, throughout this work, by mean values of the vorticities we mean simple averages of the (possibly rescaled by $1/\tau$) Bjorken components over the freezeout hypersurface without geometrical cell weighting. Therefore, the plotted mean values have no physical meaning and they should be taken as descriptive numbers which are related to the global features of vorticity components at the freeze-out. Nonetheless, when referring to Bjorken coordinates this quantity (whose we show a component in 3.3) is the one that can give us a hint of what is the path to walk. As it is expected, the normalized T-vorticity decreases as the resolution improves.

Because of the relation (3.13), the residual value at our best resolution of 0.15 fm can be taken as a numerical error for later calculations of the thermal vorticity.

3.3.2 T-vorticity for a viscous fluid

Unlike the case of an ideal uncharged fluid, T-vorticity can be generated in a viscous fluid even if it vanishes at the initial time. Thus, the T-vorticity

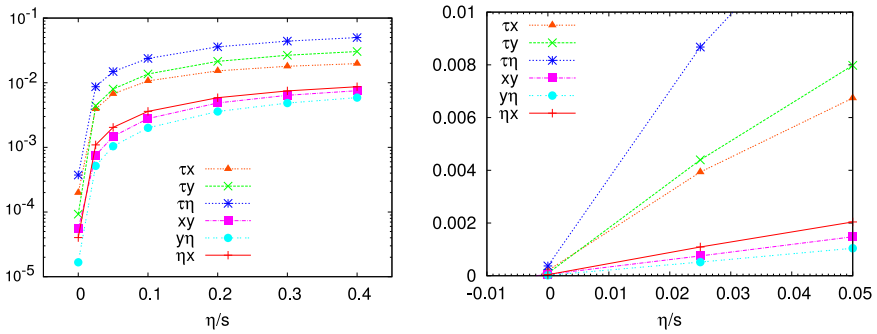

Figure 3.4: *Mean of the absolute values of $\Omega_{\mu\nu}/T^2$ components at the freeze-out as a function of η/s. Note that the $\Omega_{x\eta}, \Omega_{y\eta}, \Omega_{\tau\eta}$ have been multiplied by $1/\tau$. Upper panel: log scale. Lower panel: zoom on the zero region.*

can be used as a tool to estimate the *numerical viscosity* of the code in the ideal mode by extrapolating the viscous runs.

In general, in addition to standard truncation errors due to finite-difference interpolations, all shock-capturing upwind schemes are known to introduce numerical approximations that behave roughly as a diffusive effect, especially in the simplified solution to the Riemann problems at cell interfaces [137]. It is therefore important to check whether the code is not introducing, for a given resolution, numerical errors which are larger than the effects induced by the physics. In the following we will refer to the global numerical errors generically as numerical viscosity.

We have thus calculated the T-vorticity for different physical viscosities (in fact η/s ratios), in order to provide an upper bound for the numerical viscosity of ECHO-QGP in the ideal mode. The mean value of the T-vorticity is shown in fig. 3.4 and its extrapolation to zero occurs when $|\eta/s| < 0.002$ which is a very satisfactory value. The good performance is due to the use of high-order reconstruction methods that are able to compensate for the highly diffusive two-wave Riemann solver employed [85].

3.4 Directed flow, angular momentum and thermal vorticity

With the initial conditions reported at the end of the Sect. *3.2* we have calculated the directed flow of pions (both charged states) at the freezeout and compared it with the STAR data for charged particles collected in the

centrality interval 40-80% [134]. Directed flow is an important observable for several reasons and it has been calculated with an ideal 3+1D hydro code first by Bozek [131]; here, we extend that calculation to the viscous regime.

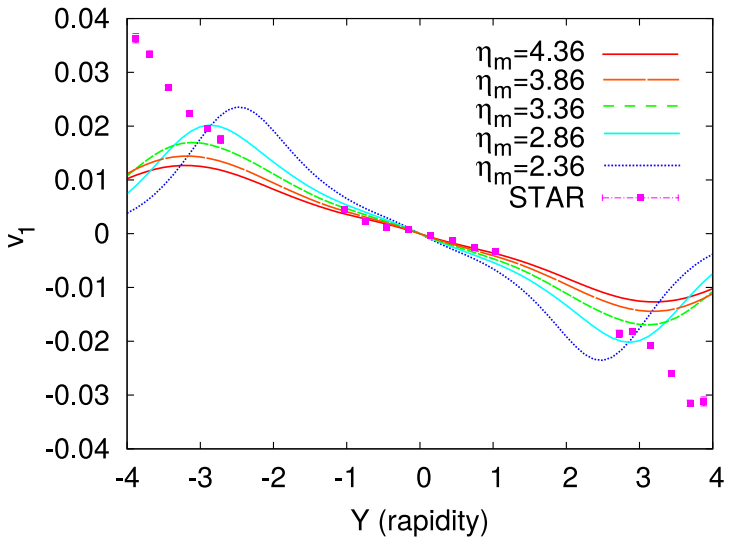

Figure 3.5: *Directed flow of pions for different values of η_m parameter with $\eta/s = 0.1$ compared with STAR data [134].*

The amount of generated directed flow at the freezeout depends of course on the initial conditions, particularly on the parameter η_m (see Sect. *3.2*), as shown in fig. 3.5. The directed flow also depends on η/s, as it can be appreciated quantitatively in fig. 3.6, and could then be used to measure the viscosity of the QCD plasma along with other azimuthal anisotropy coefficients. The dependence on η_m and η/s makes it possible to fit the best η_m parameter for a given η/s value. We have carried out a physical ECHO-QGP run with a fixed $\eta/s = 0.16$, approximately twice the conjectured universal lower bound, with a corresponding $\eta_m \simeq 2.86$. This couple of values results in a very good agreement with the observed v_1 (see fig. 3.7). It is worth discussing more in detail an interesting relationship between the value of the parameter η_m and that of a conserved physical quantity, the angular momentum of the plasma, which, for BIC is given by

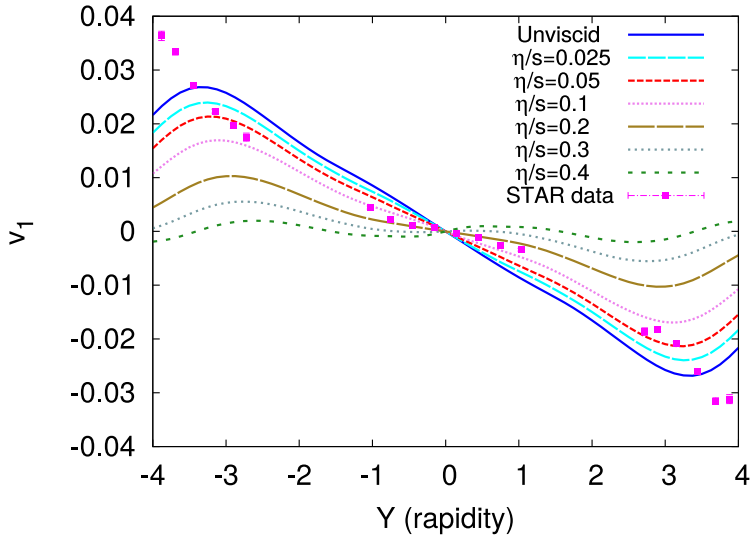

Figure 3.6: *Directed flow of pions for different values of η/s parameter with $\eta_m = 3.36$ compared with STAR data [134].*

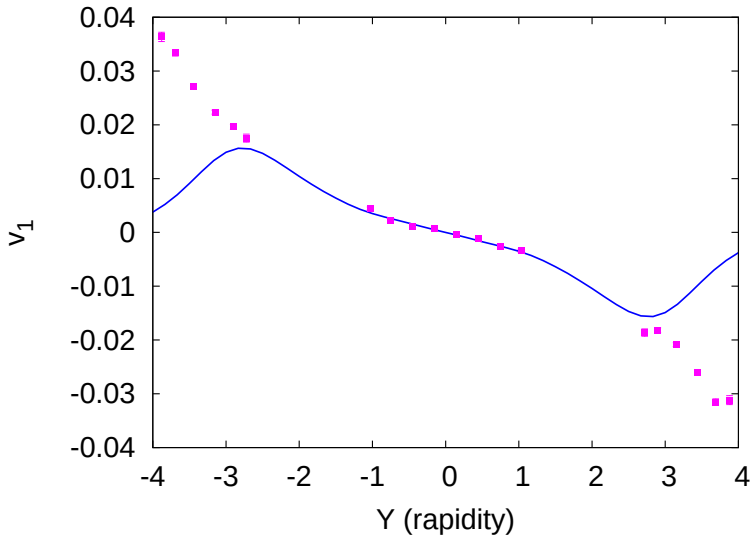

Figure 3.7: *Directed flow of pions at $\eta/s = 0.16$ and $\eta_m = 2.86$ compared with STAR data [134].*

the integral (see A for the derivation):

$$J_y = -\tau_0 \int \mathrm{d}x\mathrm{d}y\mathrm{d}\eta \; x \sinh \eta \, \varepsilon(x, y, \eta) \tag{3.23}$$

Since η_m controls the asymmetry of the energy density distribution in the $\eta - x$ plane, one expects that J_y will vary as a function of η_m. Indeed, if the energy density profile is symmetric in η, the integral in eq. 3.23 vanishes. Yet, for any finite $\eta_m \neq 0$, the profile (3.20) is not symmetric and $J_y \neq 0$ (looking at the definition of f_+ and f_- it can be realized that only in the limit $\eta_m \to \infty$ the energy density profile becomes symmetric). The dependence of the angular momentum on η_m with all the initial parameters kept fixed is shown in fig. 3.8. For the value $\eta_m = 2.86$ it turns out to be around 2.710^3 in $\hbar$ units. It is also interesting to estimate an upper

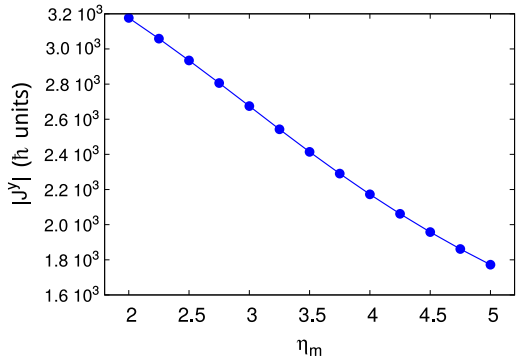

Figure 3.8: *Angular momentum (in $\hbar$ units) of the plasma with Bjorken initial conditions as a function of the parameter η_m.*

bound on the angular momentum of the plasma by evaluating the angular momentum of the overlap region of the two colliding nuclei. This can be done by trying to extend the simple formula for two sharp spheres. In our conventional reference frame, the initial angular momentum of the nuclear overlap region is directed along the y axis with negative value and can be written as:

$$J_y = \int \mathrm{d}x, \mathrm{d}y \; w(x, y)(T_+ - T_-)x\frac{\sqrt{s_{NN}}}{2} \tag{3.24}$$

where $T_\pm$ are the thickness functions like in eq. 3.17 and

$$w(x,y) = \frac{\min(n(x+b/2,y,0), n(x-b/2,y,0))}{\max(n(x+b/2,y,0), n(x-b/2,y,0))}$$

is the function which extends the simple product of two θ functions used for the overlap of two sharp spheres. Note that the $\tilde{\omega}(x,y)$ is 1 for full overlap (b=0) and implies a vanishing angular momentum for very large b (see fig. 3.9). At $b = 11.57$ fm the above angular momentum is about

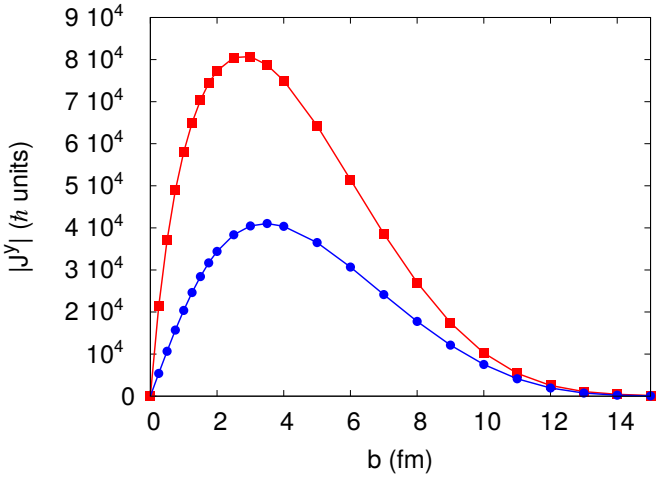

Figure 3.9: *Estimated angular momentum (in $\hbar$ units) of the overlap region of the two colliding nuclei as a function of the impact parameter*

3.510^3 in $\hbar$ units. This means that, with the current parametrization of the initial conditions, for that impact parameter about 77% of the angular momentum is retained by the hydrodynamical plasma while the rest is possibly taken away by the corona particles.

With the final set of parameters, we have calculated the thermal vorticity ϖ. As it has been mentioned in Sect. *3.1*, this vorticity is adimensional and it is a constant in global thermodynamical equilibrium [130], e.g. in a globally rotating fluid with a rigid velocity field. In relativistic nuclear collisions we are far from a such a situation, nevertheless some thermal vorticity can be generated, both in the ideal and viscous case. This is shown in figs. 3.10 and 3.11.

It can be seen that the generated amount of thermal vorticity has a significant dependence on the viscosity in all of his components and generally increases as a function thereof. Moreover, as it is evident from

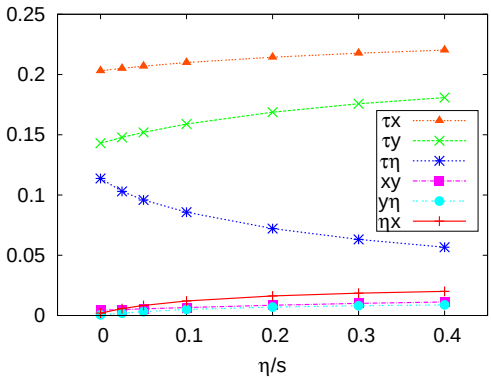

Figure 3.10: *Mean of the absolute value of thermal vorticity covariant components at the freeze-out as a function of η/s. Note that the $\varpi_{x\eta}, \varpi_{y\eta}, \varpi_{\tau\eta}$ have been multiplied by $1/\tau$.*

fig. 3.11, the $\varpi_{x\eta}$ component – which is directed along the initial angular momentum – has a non-vanishing mean value which also significantly depends on the viscosity. Its map at the freezeout is shown in fig. 3.12 where it can be seen that it attains a top (negative) value of about 0.07 corresponding to a kinematical vorticity, at the freezeout temperature of 130 MeV, of about 0.046 $c/\mathrm{fm} = 1.410^{22}\mathrm{s}^{-1}$. In this respect, the Quark Gluon Plasma would be the fluid with the highest vorticity ever made in a terrestrial laboratory. However, the mean value of this component at the same value of $\eta/s = 0.16$ is of the order of $7\,10^{-3}$, that is about ten times less than its peak value, as shown in fig. 3.11. This mean thermal vorticity is consistently lower than the one estimated in ref. [125] (about 0.05) with the model described in refs. [121, 122] implying an initial non-vanishing transverse kinematical and thermal vorticity ϖ^{Δ}. This reflects in a quite low value of the polarization of Λ baryons, as it will be shown in the next section.

3.5 Polarization

As it has been mentioned in the Introduction, vorticity can result in the polarization of particles in the final state. The relation between the polarization vector of a spin 1/2 particle and thermal vorticity in a relativistic

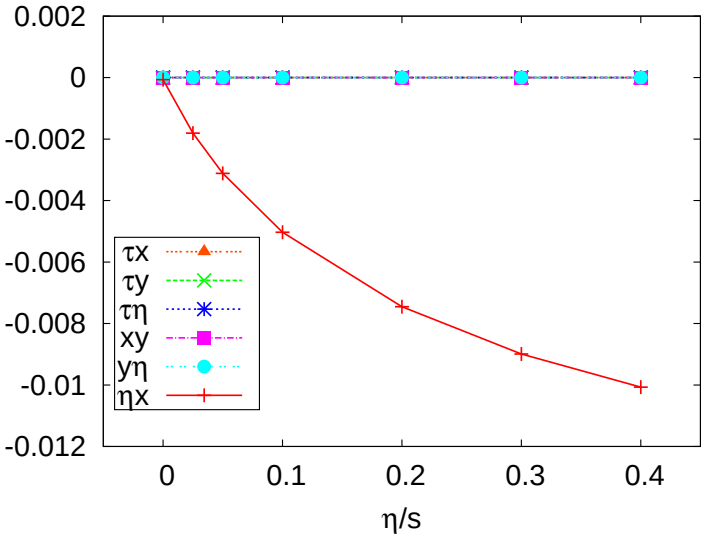

Figure 3.11: *Mean values of thermal vorticity components at the freeze-out as a function of η/s. Note that the $\varpi_{x\eta}, \varpi_{y\eta}, \varpi_{\tau\eta}$ have been multiplied by $1/\tau$.*

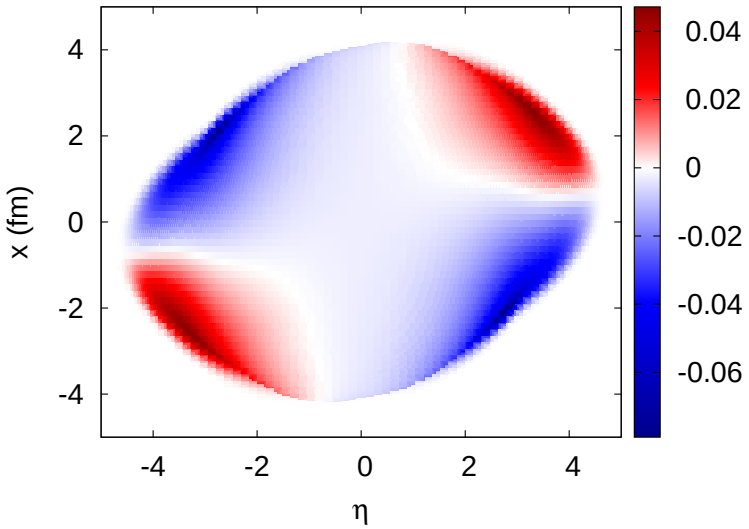

Figure 3.12: *Contour plot of $1/\tau$-scaled ηx covariant component of the thermal vorticity $\varpi_{\eta x}/\tau$ over the freeze-out hypersurface for $y = 0$, η/s=0.16, η_m=2.86.*

fluid was derived in ref. [124] and reads:

$$\Pi^{\mu}(p) = \frac{1}{8m} \frac{\int_{\Sigma} \mathrm{d}\Sigma_{\lambda} p^{\lambda} n_F (1 - n_F)\, p_{\sigma} \epsilon^{\mu\nu\rho\sigma} \partial_{\nu} \beta_{\rho}}{\int_{\Sigma} \mathrm{d}\Sigma_{\lambda} p^{\lambda}\, n_F} \tag{3.25}$$

where n_F is the Fermi-Dirac-Juttner distribution function (3.12) and the integration is over the freeze-out hypersurface Σ. The interesting feature of this relation is that it makes it possible to obtain an indirect measurement of the mean thermal vorticity at the freezeout by measuring the polarization of some hadron. For instance, the polarization of Λ baryons, as it is well known, can be determined with the analysis of the angular distribution of its decay products, because of parity violation. The polarization pattern depends on the momentum of the decaying particle, as it is apparent from eq. (3.25).

The formula (3.25) makes sense only if the components of the integrand are Minkowskian, as an integrated vector field yields a vector only if the tangent spaces are the same at each point. Before summing over the freezeout hypersurface we have then transformed the components of the thermal vorticity from Bjorken coordinates to Minkowskian by using the known rules. The obtained polarization vector $\Pi(p)$ is the one in the collision frame. However, the polarization vector which is measurable is the one in the decaying particle rest frame which can be obtained by means of the Lorentz transformations:

$$\begin{aligned} \Pi_0^0 &= \frac{\epsilon}{m} \Pi^0 - \frac{\mathbf{p} \cdot \mathbf{\Pi}}{m} \\ \mathbf{\Pi_0} &= \mathbf{\Pi} - \frac{\mathbf{p} \cdot \mathbf{\Pi}}{\epsilon(m + \epsilon)} \mathbf{p} \end{aligned} \tag{3.26}$$

In figure 3.13 we show the Λ polarization vector components, as well as its modulus, as a function of the transverse momentum $\mathbf{p}_T$ for $p_z = 0$ expected under the assumptions of local thermodynamical equilibrium for the spin degrees of freedom maintained till kinetic freezeout. It can be seen that the polarization vector has quite an assorted pattern, with an overall magnitude not exceeding 1% at momenta around 4 GeV. As expected, the y component is negative, oriented along the initial angular momentum vector and a magnitude of the order of 0.1%. Indeed, the main contribution to the polarization stems from the longitudinal component Π_0^z, with a maximum and minumum along the bisector $|p^x| = |p^y|$.

The obtained polarization values are – as expected – consistently smaller

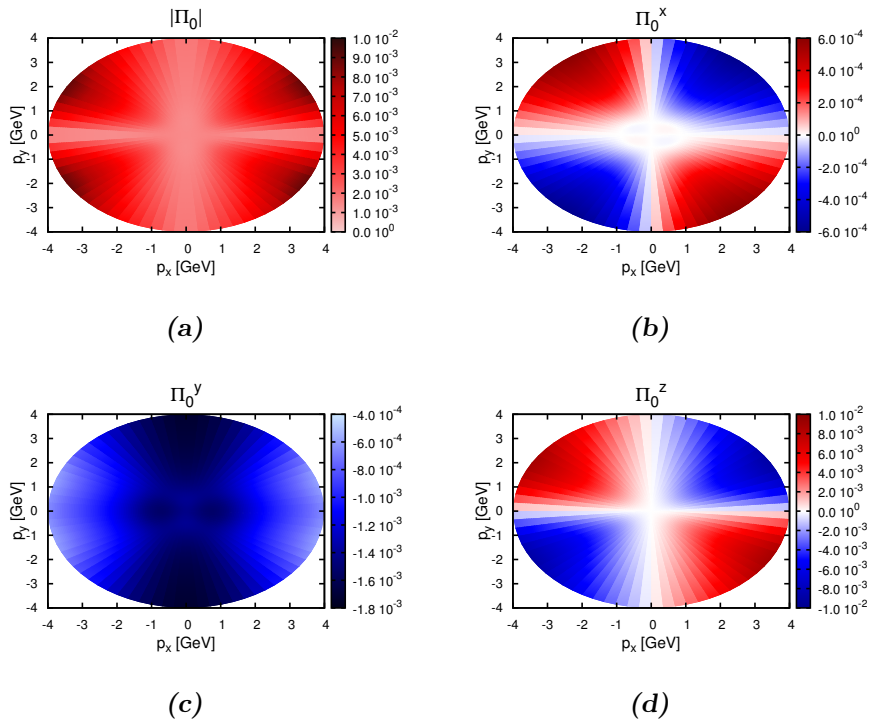

Figure 3.13: *Modulus (panel (a)) and components of the polarization vector of the Λ hyperon in its rest frame.*

than those estimated in ref. [125] (of the order of several percent with a top value of 8-9%) with the already mentioned initial conditions used in refs. [121,122]. This is a consequence of the much lower value of the implied thermal vorticity, as discussed in the previous section.

3.6 Plausibility of the initial conditions for the angular momentum

The fact that in 3+1D the plasma needs to have an initial angular momentum in order to reproduce the observed directed flow raises the question whether the Bjorken initial condition $u^\eta = 0$ is a compelling one or, instead, the same angular momentum can be obtained with a non trivial u^η and with a suitable change of the energy density profile. For a testing purpose, we have run ECHO-QGP with an initial profile:

$$u^\eta = \frac{1}{\tau} \tanh Ax \ \sinh(y_{\rm beam} - |\eta_s|) \tag{3.27}$$

which meets the causality constraint. In fact, the inequality expressing the causality constraint in the hydrodynamical picture of relativistic heavy ion collisions is that the initial longitudinal flow velocity must not exceed the velocity of beam protons $v_z < v_{\rm beam}$ (assuming vanishing initial transverse velocity):

$$|y| = \left|\frac{1}{2}\log\frac{1+v_z}{1-v_z}\right| = |\log(u^0+u^z)| \leq y_{\rm beam} \tag{3.28}$$

By using the transformation rules (A.10):

$$\begin{aligned}
\log(u^0+u^z) &= \log\left[(\cosh\eta_s + \sinh\eta_s)(u^\tau + \tau u^\eta)\right] \\
&= \log\left[\mathrm{e}^\eta(\sqrt{1+\tau^2 u^{\eta 2}} + \tau u^\eta)\right] \\
&= \eta_s + \log(\sqrt{1+\tau^2 u^{\eta 2}} + \tau u^\eta) \\
&= \eta_s + \mathrm{asinh}(\tau u^\eta) \qquad\qquad \leq y_{\rm beam}
\end{aligned} \tag{3.29}$$

the inequality (3.28) becomes:

$$|\eta_s + \mathrm{asinh}(\tau u^\eta)| \leq y_{\rm beam}$$

which can be solved for u^η:

$$-\frac{1}{\tau}\sinh(y_{\text{beam}}+\eta_s) \leq u^\eta \leq \frac{1}{\tau}\sinh(y_{\text{beam}}-\eta_s) \tag{3.30}$$

The form (3.27) fulfills the above inequality.

It is found that even for very small values of the parameter A ($5\cdot10^{-4}$ corresponding to a $J_y = 2.9{\cdot}10^3$ and $-5{\cdot}10^{-4}$ corresponding to $J_y = 2.6{\cdot}10^3$) keeping the other parameters fixed the directed flow exhibits two wiggles around midrapidity (see fig. 3.14) which are not seen in the data. From this very preliminary assessment, we can at least guess that in the Bjorken scheme an initial longitudinal flow velocity is disfavoured.

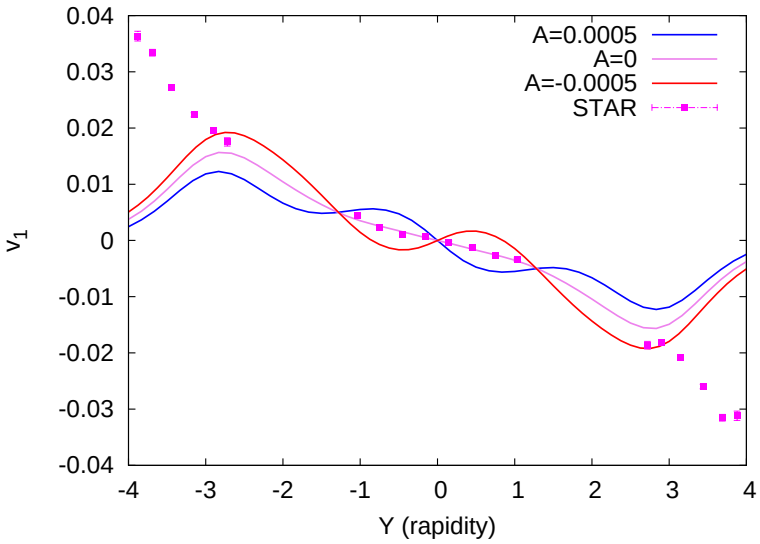

Figure 3.14: *Directed flow of pions at $\eta/s = 0.16$ and $\eta_m = 2.86$ and with the initial u^η in the eq. (3.27) compared with STAR data [134].*

4

A perturbative approach to the hydrodynamics of heavy-ion collisions

In recent years, fluid dynamic simulations of relativistic heavy ion collisions have provided strong evidence that the momentum distributions of soft hadrons is the result of a fluid dynamic evolution of an initial state that includes density fluctuations (see Refs. [6, 138–140] for recent reviews). The research focuses now on understanding in detail the mapping from fluctuations in the initial state, to experimentally accessible observables in the final state [53, 55, 60, 62, 101, 141–147].

The present chapter aims at quantifying to what degree this hydrodynamic mapping is linear in the strength of initial fluctuations around some suitably chosen background, and on what scale non-linearities arise. This is of interest since an *approximately* linear relation would provide a particularly simple, and thus useful, tool for relating experimental observables to the initial conditions of heavy ion collisions and to those properties of matter that govern their fluid dynamic evolution [148]. Note that when we say *linear relation* we mean a mapping in which non-linearities, although unquestionably present, can be understood as small corrections of a predominantly linear mapping.

4.1 Theoretical basis

The fluctuating initial conditions used for the hydrodynamic modeling of heavy ion collisions, are specified in terms of fluid dynamic fields (h_i) slightly varying over a hypersurface at fixed initial time τ_0, and depending on the coordinates $(\tau, x = r\cos\phi, y = r\sin\phi, \eta_s)$

$$h_i(\tau, r, \varphi, \eta) = \Big(w, u^r, u^\phi, u^\eta, \pi_{\rm bulk}, \pi^{\eta\eta}, \dots\Big) \,, \tag{4.1}$$

where we employed a different index i for every independent field. Such fields can possibly be the enthalpy density $h_1 = w$, three independent fluid velocity components, the bulk viscous tensor, the independent components of the shear viscous tensor, etc.
In the following we assume Bjorken boost invariance and drop the rapidity-argument η_s in the hydrodynamical fields. Following Refs. [148, 149], h_i are expressed in terms of a background component h_i^{BG} and an appropriately normalized perturbation $\tilde{h}_i$ (see Appendix **??** for details). The background is taken to be a solution of the non-linear hydrodynamic equations initialized at τ_0 with an azimuthally symmetric average over many events, and it is then evolved with ECHO-QGP. For any sample of events, this background needs to be determined only once. The time evolution of the normalized perturbation $\tilde{h}_i$ is viewed as a perturbative series on top of the background fields, where the kernels $\mathscr{G}_{ij}$, $\mathscr{H}_{ijk}$ (and corresponding terms for higher orders in $\tilde{h}_i$) depend on the time-evolved background h_i^{BG} only. In order to avoid an exceedingly heavy notation, we decide to drop the dependence of the kernels from the coordinates, specifying them here:

$$\begin{aligned} \mathscr{G}_{ij} &= \mathscr{G}_{ij}(\tau, \tau_0, r, r', \varphi - \varphi') \\ \mathscr{H}_{ijk} &= \mathscr{H}_{ijk}(\tau, \tau_0, r, r', r'', \varphi - \varphi', \varphi - \varphi'') \end{aligned} \tag{4.2}$$

Due to the azimuthal rotation symmetry of the background, those kernels depend on the angles φ, φ' , φ'' only via their difference (i.e. $\varphi - \varphi'$).

Making use of this notation, we write down the time evolution of the normalized perturbation $\tilde{h}_i$ as:

$$\begin{aligned} \tilde{h}_i(\tau, r, \varphi) = &\int_{r',\varphi'} \mathscr{G}_{ij}\tilde{h}_j(\tau_0, r', \varphi') \\ &+ \frac{1}{2}\int_{r',r'',\varphi',\varphi''} \mathscr{H}_{ijk}\tilde{h}_j(\tau_0, r', \varphi')\ \tilde{h}_k(\tau_0, r'', \varphi'') \\ &+ \mathcal{O}(\tilde{h}^3)\,, \end{aligned} \tag{4.3}$$

where $\int_r = \int_0^\infty dr\, r$, $\int_\varphi = \int_0^{2\pi} d\varphi$ etc.

We now want to examine the extent of this linearity in the hydrodynamic frame: we ask whether the expansion (4.3) is possible for a suitably chosen background and whether it is dominated by the first linear term. To address this question, we compare in the following numerical results from a full causal dissipative hydrodynamic evolution to expectations based on the structure and on the symmetries of the perturbative series (4.3).

It must be remarked that hydrodynamic evolution is governed by non-linear partial differential equations and it may be chaotic or it may contain terms that are non-analytic in the initial fluid fields $\tilde{h}_j$. Hence, the validity of the expansion (4.3) cannot be guaranteed as true a priori. Also, such expansion depends on the choice of the background h^{BG} and on the strength of the perturbations $\tilde{h}$.

For the initial conditions, we assume once again that the initial transverse velocity components vanish, the longitudinal velocity is Bjorken boost invariant, the shear stress tensor is initialized by its Navier-Stokes value, and the bulk viscous pressure is neglected. Initial fluctuations reside then only in the initial enthalpy density $w(\tau, \vec{r})$, that we parametrize in terms of an *azimuthally averaged background* $w_{BG}(\tau, r)$ and the *weights* $\tilde{w}_l^{(m)}$ of the azimuthal (m) and radial (l) wave numbers of a *discrete orthonormal Bessel-Fourier decomposition* [148]:

$$w(\tau_0, r, \varphi) = w_{BG}(\tau_0, r) \left(1 + \sum_{m=-\infty}^{\infty} \tilde{w}^{(m)}(\tau_0, r)\, e^{im\varphi}\right),$$
$$\tilde{w}^{(m)}(\tau_0, r) = \sum_{l=1}^{\infty} \tilde{w}_l^{(m)}\, J_m\left(k_l^{(m)} r\right). \tag{4.4}$$

Here $k_l^{(m)} = z_l^{(m)}/R$, where $z_l^{(m)}$ is the l-th zero of the modified Bessel function J_m and $R = 8$ fm.
Since $\tilde{w}(\tau, r, \varphi)$ is real, we have $\tilde{w}^{(m)}(\tau, r) = \tilde{w}^{(-m)*}(\tau, r)$. Without loss of generality, we can take the weights with $m \geq 0$ as the independent ones and write

$$\tilde{w}_l^{(m)} = |\tilde{w}_l^{(m)}| e^{-im\psi_l^{(m)}}. \tag{4.5}$$

The corresponding modes with $m < 0$ are then not independent and are defined by the condition

$$|\tilde{w}_l^{(m)}| = |\tilde{w}_l^{(-m)}|$$

η/s	Δx fm	Δy fm	$\Delta\tau$ fm/c	Courant number	algorithmic kernel
$1/4\pi$	0.2	0.2	10^{-3}	0.2	MPE5

Table 4.1: *Setup for the study of the non-linearity of hydrodynamic evolution. The MPE5 scheme is the most accurate one available in ECHO-QGP (fifth order for smooth flows). Following Ref. [150], we use the equation of state s95p-PCE which combines lattice QCD results at high temperatures with a hadron resonance gas at low temperatures.*

with azimuthal angle $\psi_l^{(-m)} = \psi_l^{(m)} \pm \pi$.

4.2 Single mode

We consider first the case for which one single fluctuating basis mode is embedded on top of $w_{BG}(\tau_0, r)$. For example, we specify this mode with the weight $\tilde{w}_1^{(2)}$, so that the initial enthalpy density reads

$$w(\tau_0, \vec{r}) = w_{BG}(\tau_0, r) \left[1 + 2|\tilde{w}_1^{(2)}| J_2\left(k_1^{(2)} r\right) \cos\left(2(\varphi - \psi_1^{(2)})\right)\right] . \quad (4.6)$$

For one single mode, we can set without loss of generality $\psi_1^{(2)} = 0$.

The background w_{BG} used throughout in this work is initialized at $\tau_0 = 0.6$ fm/c with an azimuthally symmetric average of Glauber model initial conditions for Pb+Pb collisions at the LHC, described in Ref. [149]. We assume Bjorken-boost invariance, letting ECHO-QGP evolve this initial profile with the setup in table 4.1 in 2+1 dimension.

The time-evolved fluctuation $\tilde{w}^{(2)}(\tau, r)$ is determined from the full hydrodynamic evolution via Fourier analysis. Results are shown in fig. 4.1 for $\tau = \tau_0 + 5\,\text{fm/c}$ and $\tau = \tau_0 + 10\,\text{fm/c}$ after initialization and for different weights $\tilde{w}_1^{(2)}$. Fluctuations at time τ_0 are cut-off in the region of very low background density, see e.g. $\tilde{w}^{(2)}(\tau_0, r)$ in fig. 4.1 – we have checked that this does not affect our results. This analysis suggests that at all relevant times and even for relatively large initial amplitudes $\tilde{w}_1^{(2)}$, the fluid dynamic response $w_{BG}\tilde{w}^{(2)}(\tau, \vec{r})$ to an initial perturbation scales *approximately linearly* with the weight $\tilde{w}_1^{(2)}$, in fact the perturbation scales as its initial weight (see middle and lowe panel). We observe this linear dependence with similar accuracy also for other basic modes (data not shown).

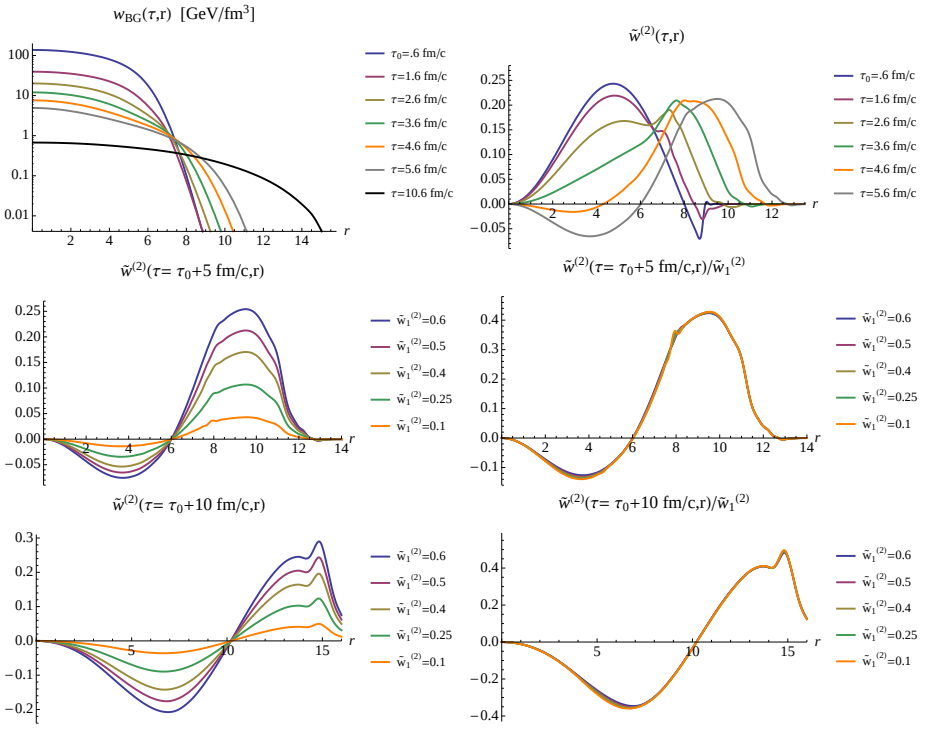

Figure 4.1: *Results for the hydrodynamic evolution of the initial condition (4.6), obtained with ECHO-QGP. Upper row: the time dependence of the enthalpy density is shown separately for the background $w_{BG}(\tau, r)$ and for the perturbation $\tilde{w}^{(2)}(\tau, r)$ initialized with $\tilde{w}_1^{(2)} = 0.5$. Middle row: the dependence of the perturbations $\tilde{w}^{(2)}$ on the initial weight for $\tau = \tau_0 + 5\text{fm}/c$ (left) and scaled by the initial weights, $\tilde{w}^{(2)}(\tau, r)/\tilde{w}_1^{(2)}$ (right). This scaling establishes that the fluid dynamic response to perturbations is approximately linear. Lower row: same results as shown in middle row, but for $\tau = \tau_0 + 10\text{fm}/c$.*

This linear behavior of the response of $\tilde{w}^{(m)}(r, \tau)$ with the initial weights $w_l^{(m)}$, is expected from the linear term in eq. (4.3), but it does not imply that non-linearities are absent. To see that, consider the Fourier series

$$\tilde{h}_i(\tau, r, \varphi) = \frac{1}{2\pi} \sum_{m=-\infty}^{\infty} e^{im\varphi}\, \tilde{h}_i^{(m)}(\tau, r),$$

where $\tilde{h}_i^{(m)}(\tau, r)$ are in general complex expansion coefficients, but $\tilde{h}_i^{(m)}(\tau, r) = \tilde{h}_i^{(-m)*}(\tau, r)$ since $\tilde{h}(\tau, r, \varphi) \in \mathbb{R}$. Since the kernels in (4.2-4.3) depend only on the background field, they are invariant under azimuthal rotation and

their Fourier expansions read[1]

$$\begin{aligned}\mathscr{G}_{ij} &= \frac{1}{2\pi}\sum_{m=-\infty}^{\infty} e^{im\Delta\varphi}\mathscr{G}_{ij}^{(m)}(\tau,\tau_0,r,r')\,,\\ \mathscr{H}_{ijk} &= \frac{1}{(2\pi)^2}\sum_{\substack{m'=-\infty\\ m''=-\infty}}^{\infty} e^{i(m'\Delta\varphi'+m''\,\Delta\varphi'')}\;\mathscr{H}_{ijk}^{(m',m'')}(\tau,\tau_0,r,r',r'')\,,\end{aligned} \tag{4.7}$$

and so on. From $\mathscr{G}_{ij}\in\mathbb{R}$ and $\mathscr{H}_{ijk}\in\mathbb{R}$ one can write

$$\mathscr{G}_{ij}^{(m)}(\dots) = \mathscr{G}_{ij}^{(-m)*}(\dots) \qquad \text{and} \qquad \mathscr{H}_{ijk}^{(m',m'')}(\dots) = \mathscr{H}_{ijk}^{(-m',-m'')*}(\dots)\,.$$

Then from eq. (4.3), one obtains:

$$\begin{aligned}\tilde{h}_i^{(m)}(\tau,r) = &\int_{r'}\mathscr{G}_{ij}^{(m)}(\tau,\tau_0,r,r')\,\tilde{h}_j^{(m)}(\tau_0,r')\\ &+\frac{1}{2}\int_{r',r''}\frac{1}{2\pi}\sum_{\substack{m'\\ m''}}\delta_{m,m'+m''}\mathscr{H}_{ijk}^{(m',m'')}(\tau,\tau_0,r,r',r'')\,\tilde{h}_j^{(m')}(\tau_0,r')\,\tilde{h}_k^{(m'')}(\tau_0,r'')\\ &+\dots\end{aligned} \tag{4.8}$$

Going back to the studied case, in which initial conditions contain only fluctuations of enthalpy density, we have $\tilde{h}_j^{(m)}(\tau_0,r) = \delta_{j1}\;\tilde{w}^{(m)}(\tau_0,r)$. Using the orthonormal expansion (4.4) for $\tilde{w}^{(m)}(\tau_0,r)$, one can write eq. (4.8) as

$$\begin{aligned}\tilde{h}_i^{(m)}(\tau,r) = &\sum_{l'}\mathscr{G}_{i1\,;\,l'}^{(m)}(\tau,\tau_0,r)\,\tilde{w}_{l'}^{(m)}\\ &+\frac{1}{4\pi}\sum_{\substack{m',l'\\ m',l''}}\delta_{m,m'+m''}\mathscr{H}_{i11\,;\,l'l''}^{(m',m'')}(\tau,\tau_0,r)\;\tilde{w}_{l'}^{(m')}\;\tilde{w}_{l''}^{(m'')}\\ &+\dots\end{aligned} \tag{4.9}$$

with

$$\mathscr{G}_{i1\,;\,l'}^{(m)}(\tau,\tau_0,r) = \int_{r'}\mathscr{G}_{i1}^{(m)}(\tau,\tau_0,r,r')\;J_m\left(k_{l'}^{(m)}r'\right), \tag{4.10}$$

and similarly for $\mathscr{H}_{i11\,;\,l'l''}$.

According to (4.8), if one initializes fluctuations with a *single* mode of weight $\tilde{w}_l^{(m)}$, as done in fig. 4.1, then corrections that are quadratic in the

[1] We keep the arguments for the Fourier expansion, in order to make it distinguishable from the kernel itself.

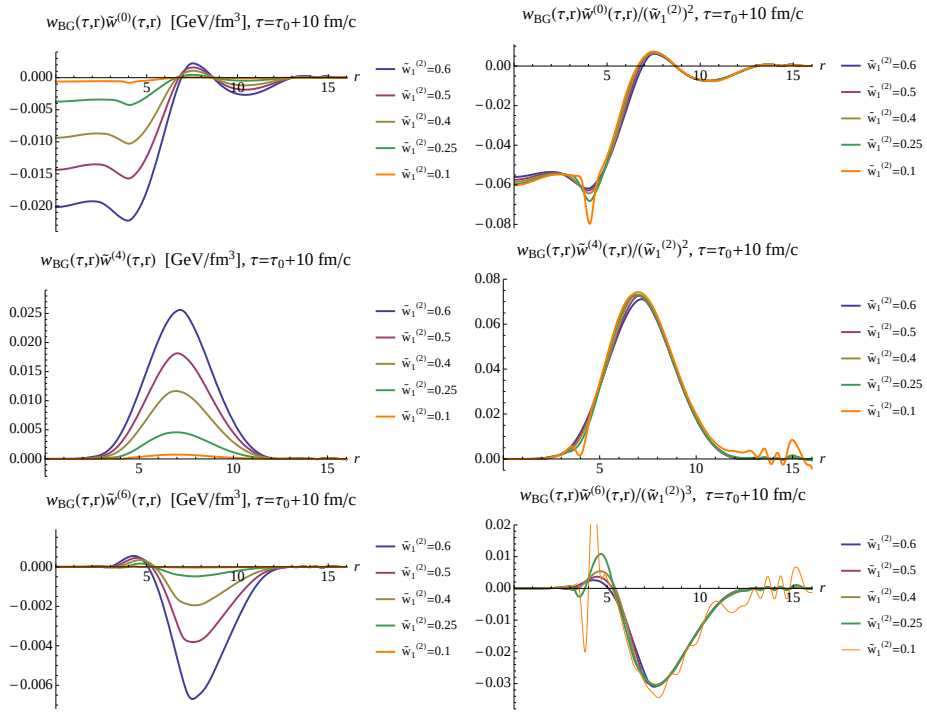

Figure 4.2: *Left column: the zeroth, fourth and sixth harmonic perturbations induced by an initial fluctuation in the second harmonic, shown for different values of the initial weight $\tilde{w}_1^{(2)}$. Right column: Same results but rescaled by the second (third) power of the weight $\tilde{w}_1^{(2)}$. This scaling establishes that $\tilde{w}^{(0)}(\tau,r)$ and $\tilde{w}^{(4)}(\tau,r)$ ($\tilde{w}^{(6)}(\tau,r)$) can be understood as overtones that are induced by the initial second harmonic perturbation as a perturbative second (third) order correction to (4.3). The short-range fluctuations in the rescaled $\tilde{w}^{(6)}(\tau,r)$ result from amplifying the numerical uncertainties of very small number by a large scaling factor $(1/\tilde{w}_1^{(2)})^3 = 1000$.*

fluctuations $\tilde{h}_i(\tau_0)$ will not appear in the time-evolved harmonics $\tilde{h}_i^{(m)}$, but in the harmonics $\tilde{h}_i^{(2m)}$ and $\tilde{h}_i^{(0)}$ instead. Also the third order correction enters the fluctuating fields in $\tilde{h}_i^{(3m)}$ (and it enters in $\tilde{h}_i^{(m)}$ as a correction that is subleading by two orders compared to the leading linear response).

To illustrate this general feature, one can compare the dominant linear response $w_{BG}\,\tilde{w}^{(2)}$ shown in fig. 4.1 with the leading quadratic ($w_{BG}\,\tilde{w}^{(0)}$, $w_{BG}\,\tilde{w}^{(4)}$) and cubic ($w_{BG}\,\tilde{w}^{(6)}$) corrections displayed in fig. 4.2. We observe that quadratic (cubic) corrections scale with the square (the cube) of the initial weight $\tilde{w}_1^{(2)}$, as expected from eq. (4.8). Moreover, even for a weight $\tilde{w}_1^{(2)} = 0.5$, quadratic corrections are approximately a factor 5 smaller than

the linear response, and cubic corrections are another factor 5 smaller than the quadratic ones. From Ref. [149], we know that for realistic initial conditions in heavy ion collisions, the average weights of basis modes are of order $O(0.1)$ and that only the tails of event distributions in $\tilde{w}_l^{(m)}$ may reach values of order 0.5. Fig. 4.2 thus shows that for the studied case, non-linear corrections, while clearly present, could be treated as small perturbations for fluctuations of realistic weight.

4.3 Higher harmonics

So far, we have demonstrated with examples that Eq. (4.9) explains the dominance of linear response and the relative size and ordering of the overtones induced by one basis fluctuation. We have also checked that the same equation explains the structure and the symmetries of the hydrodynamic interactions between initial perturbations, with different wave numbers.

Fig. 4.3 shows a case for which two perturbations $\tilde{w}_2^{(2)}$, $\tilde{w}_1^{(3)}$ are embedded on top of the initial background fields. We have checked that the second and third harmonics of the fluid dynamic response ($\tilde{w}^{(2)}(\tau, r)$ and $\tilde{w}^{(3)}(\tau, r)$) scale linearly with their respective initial weights ($\tilde{w}_2^{(2)}$ and $\tilde{w}_1^{(3)}$). We also cheked (data not shown here) how they agree to high accuracy with the response to an initial configuration in which only one mode ($\tilde{w}_2^{(2)}$ or $\tilde{w}_1^{(3)}$) is embedded on top of w_{BG}. Also, higher even harmonics (like $\tilde{w}^{(4)}(\tau, r)$) scale with the square of $\tilde{w}_2^{(2)}$, similarly to the case shown in fig. 4.2.

In order to study the interactions between different modes, we show in fig. 4.3 the first and fifth harmonics. According to eq. (4.9) such harmonics are the only ones that receive (leading) second order contributions proportional to $\tilde{w}_2^{(2)}\tilde{w}_1^{(3)}$. If $\psi^{(2)} \neq \psi^{(3)}$, then the responses $w_{BG}\tilde{w}^{(1)}$ and $w_{BG}\tilde{w}^{(5)}$ consist of both a real and an imaginary part. Both parts exhibit the expected scaling with $\tilde{w}_2^{(2)}\tilde{w}_1^{(3)}$, as can be seen in fig. 4.3. Also, according to (4.9), the phases of the first and fifth harmonics are determined by the orientations of the initial perturbations. The comparison with the full numerical results in the middle panel of fig. 4.3 shows that this perturbative expectation is realized approximately: strong deviations are seen only for values of the radius r for which either the real part ($\mathrm{Re}\big[\tilde{w}^{(m)}\big]$) or the imaginary part ($\mathrm{Im}\big[\tilde{w}^{(m)}\big]$) is approaching zero, making the orientation ill defined.

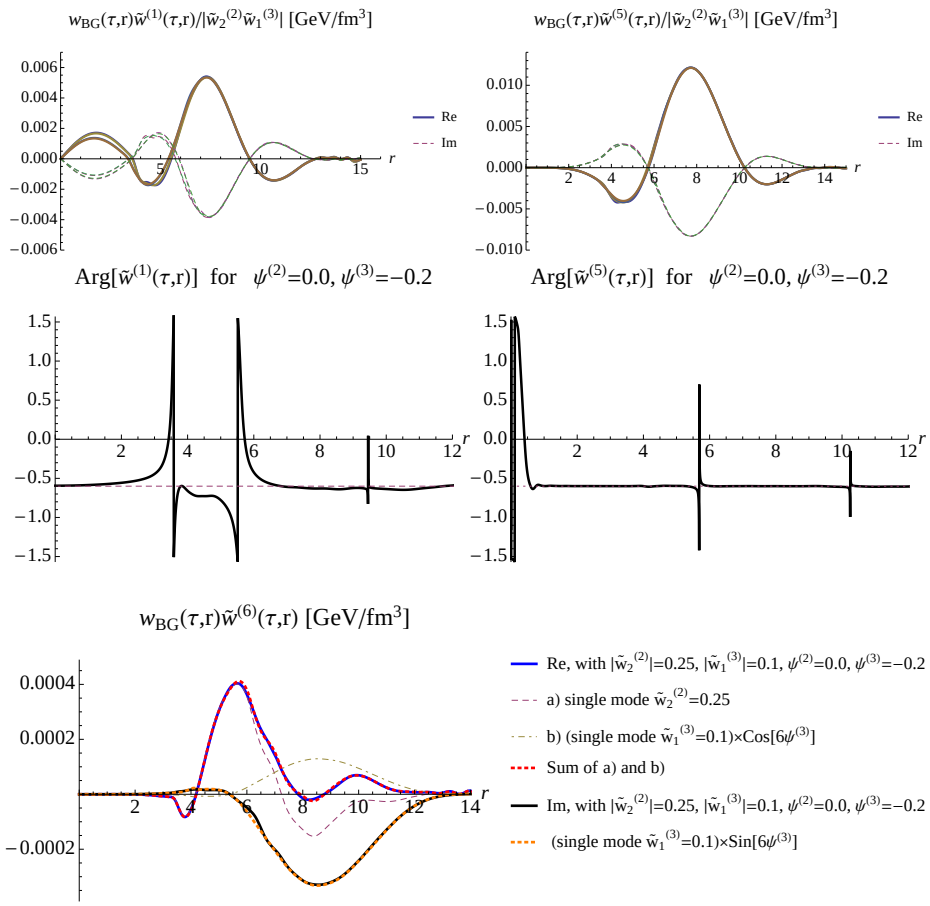

Figure 4.3: *Results from ECHO-QGP for evolving up to $\tau = \tau_0 + 10$ fm/c on top of the background of fig. 4.1 an initial condition composed of two basis modes with weights $\tilde{w}_2^{(2)}$, $\tilde{w}_1^{(3)}$ and angles $\psi^{(2)} = 0$ and $\psi^{(3)} = -0.2$.*
Upper row: Real and imaginary part of the first and the fifth harmonics of the enthalpy. The curves shown are for the four combinations of $\tilde{w}_2^{(2)} = 0.1, 0.25$ and $\tilde{w}_1^{(3)} = 0.1, 0.25$ and illustrate scaling behavior.
Middle row: The phase $\mathrm{Arg}\left[\tilde{w}^{(m)}(\tau, r)\right]$ of the m-th harmonic mode (solid) compared to the perturbative expectation (dashed line) based on Eq. (4.9).
Lower row: Real and imaginary part of the sixth harmonic (solid lines). The dashed and dotted lines show results for the individual contributions of single basis modes. When appropriately weighted with the phase factors according to the perturbative Eq.(4.9), their sum agrees with the full numerical result.

To add one level of complication, we consider finally the sixth harmonics $w_{BG}\tilde{w}^{(6)}$ that, according to (4.9), receives corrections of second order in $\tilde{w}_1^{(3)}$ and of third order in $\tilde{w}_2^{(2)}$. Weighting both contributions with the perturbatively expected information on phases and amplitude, provides a full quantitative understanding of the numerically determined signal $w_{BG}\tilde{w}^{(6)}$ as overtones of the two initial perturbations. This can be appreciated in fig. 4.3. that illustrates that the interaction between initial perturbations of different wave numbers can be understood perturbatively.

4.4 Application to realistic initial conditions

Realistic initial conditions for the fluid dynamic evolution of heavy ion collisions are expected to involve fluctuations on many different length scales and with large amplitudes. It might be argued that the examples discussed so far, although initialized with relatively large amplitudes, are still academic, and that they cannot be extended to deal with the complexity of a realistic heavy ion collision.

In order to address such concerns, we have embedded simple basis modes in realistic initial conditions with many and large fluctuations. Fig. 4.4 shows such an initial distribution. It is constructed by subtracting from an arbitrary initial condition, generated by a Glauber model, the contribution leading to a second harmonic and adding then the perturbation of (4.6). In this way, we have built a state that embeds both an analytically controlled initial perturbation and a realistically fluctuating background. We can extract the form of the initial perturbation and the time dependence of its fluid dynamic response via Fourier analysis. The lower panel of fig. 4.4 shows that this dynamical response in an event with realistic fluctuations is described to high accuracy by the linear response on top of the smooth background that we had established in fig. 4.1.

The evolution of initial anisotropic density perturbations, as determined numerically with ECHO-QGP, seems to follow a pattern that can be understood order-by-order in a perturbative expansion for small deviations from an azimuthally symmetric event-averaged background. The leading order is linear and modes with different azimuthal wave numbers do not mix. Quadratic and higher orders can be seen as next-to-leading order corrections. They influence modes with azimuthal wave numbers that can be written as sums (or differences) of the seed wave numbers. Since the

non-linear couplings are numerically small, the higher harmonics generated by two-mode or three-mode interactions will often be small in comparison to initially present and linearly evolving perturbations. This ordering may be less pronounced for non-central collisions where the elliptic modes (with $m = 2$) have a particularly strong weight such that its overtones with $m = 4, 6$ etc. may dominate over primordial density perturbations with these wave numbers. We also note that the relative importance of linear and non-linear terms depends significantly on the dissipative properties of the medium. In exploratory studies we found that for increasing η/s, the linear

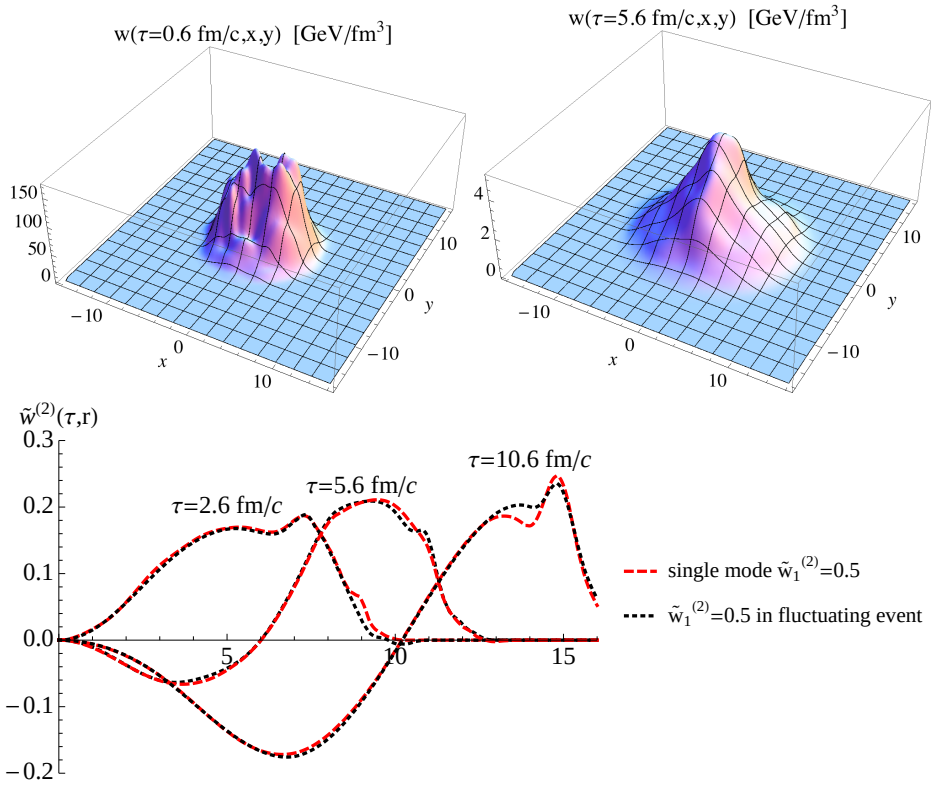

Figure 4.4: *Upper panels: Left: Example of an initial condition with many fluctuating modes $\tilde{w}_l^{(m)}$, $m \neq 2$, and the mode $\tilde{w}_1^{(2)} = 0.5$ on top of the background w_{BG}. Right: The same distribution, evolved up to $\tau = \tau_0 + 5$ fm/c.*
Lower panel: The second harmonics $\tilde{w}^{(2)}(\tau, r)$ extracted for different times τ. Results extracted from the fluctuating event shown in the upper panel are compared to the case shown in fig. 4.1 in which $\tilde{w}_1^{(2)} = 0.5$ is the only mode embedded on top of a smooth background. This illustrates that the assumption of a predominantly linear response on top of a suitably chosen background is applicable for realistic initial conditions that display strong fluctuations.

response is more dominant and the relative weight of higher non-linear orders decreases. Such a more laminar behavior is expected on general grounds. All results shown in this chapter are for a rather minimal value of $\eta/s = 1/4\pi$ which maximizes contributions from non-linear corrections.

Conclusions and Outlook

In this Thesis, ECHO-QGP was presented as a state of the art resource for 3+1-D hydrodynamic simulation of the QGP created during heavy-ion collisions. It features high accuracy methods for time integration, spatial interpolation and reconstruction routines (which are essential to capture small-scale hydrodynamic phenomena and turbulence) together with the inclusion of second-order treatment of dissipative effects through the evolution of the Israel-Stewart equations for the bulk and shear stress tensor components, coupled to hydrodynamical equations. ECHO-QGP is a branch development of ECHO [86], which is used for astrophysical purposes, and as its parent features the same shock-capturing approach, which is essential to treat shocks and other discontinuities that invariably arise due to the intrinsic nonlinear nature of the hydrodynamic equations. Its reliability has been shown in chapter 1, where its response to many of the most common, and nonetheless most stringent, tests was shown. In particular, we showed how ECHO-QGP reproduces with very high accuracy the analytical and semi-analytical solutions of the so-called "Gubser flow" [68, 92, 94, 95], which represent a very stringent test of the quality of the algorithm and the suitability for the applications to the dissipative hydro modeling of the heavy-ion collisions. The discrepancy between the numerical and the analytical solutions is on average of the order of the per mil, and the agreement is still excellent up to late times both for the temperature, and for all the shear-stress tensor components.

We would also like to stress that ECHO-QGP was designed to be publicly released, and for this reason it praises some very useful features: it is user-friendly, well documented and provides a high level of customization of the simulation without any change in the source code. In particular:

- It offers the possibility to perform a simulation both in the simple Minkowski metric, as well as in Bjorken coordinates. In both cases the evolution can be carried out in any dimensionality (1+1D, 2+1D and 3+1D).

- It is possible to use customized any Equation of State, be it tabulated (passing to the code an external table file) or analytical (specific files have been arranged for this kind of usage). In particular we have tested the ideal ultra-relativistic EoS $P = e/3$, a tabulated one arising from weak-coupling QCD calculations often adopted in the literature [102]. Also tabulated hybrid EoS's, obtained by matching those for a hadron resonance gas [35, 151] with lattice-QCD results, have been tested.

- The same level of customization goes with the initializing conditions. Among the available setups, one can find the one specially designed to reproduce the RHIC results: the initial hydrodynamic quantities are computed through the optical or Monte Carlo Glauber model with both participants and binary collisions contributions, and with different choices for the impact parameter b. This initialization can be used both in in 2+1D and 3+1D, and for different colliding nuclei.

- The decoupling routine, based on the Cooper-Frye prescription, is implemented in the ECHO-QGP package. Although the bundle still does not include a kinetic approach to be coupled to the hydrodynamic stage, the output has been designed to handle this matching procedure. The very next step we plan to do towards this direction is to find a suitable candidate for the afterburner, among the ones available [152], and include it in the package. The decoupling procedure has been successfully tested against other available routines in the literature, both in 2+1D and in 3+1D.

Our efforts, so far devoted to the development of the code and to its validation, from now on should be focused on an activity of tuning ECHO-QGP, through a systematic comparison with the experimental data, in order to eventually release a tool for the entire scientific community to address soft-physics studies in heavy-ion collisions.

Given its unique features, ECHO-QGP has been an essential resource for the physics studies of the QGP features. We have in fact derived the

vorticities developed in peripheral nuclear collisions at $\sqrt{s}_{\rm NN} = 200$ GeV, in a model where the most commonly used initial conditions in the Bjorken hydrodynamical scheme were adopted. In such case, the thermal vorticity over the freeze-out hypersurface can be as large as 0.05 c/fm. Yet, its mean value is not large enough to produce a polarization of Λ hyperons larger than 1%, which is a significantly lower estimate in comparison with other recent calculations based on simpler assumptions.

We have found that the magnitude of directed flow, at this energy, has a sizeable dependence on both the shear viscosity and the longitudinal energy density profile asymmetry parameter η_m which in turn governs the amount of initial angular momentum retained by the plasma. We also showed that finding a model for the initial profile of flows that meets causality constraint, and different from the usual Bjorken initial condition, is not trivial: the directed flow in this case proves to be a good discriminating factor.

ECHO-QGP has also been exploited to study the nature of the relation between the initial and final states of the hydrodynamic evolution. In particular it allowed to provide a useful ordering scheme for a more detailed understanding of the evolution of fluctuations in hydrodynamic fields, as discussed in chapter 4. We provided evidence from full numerical solutions that the hydrodynamical evolution of initial density fluctuations can be understood order-by-order in a perturbative series in deviations from a smooth and azimuthally symmetric background solution. To leading linear order, modes with different azimuthal wave numbers do not mix. When quadratic and higher order corrections are numerically sizable, they can be understood as overtones with corresponding wave numbers in a perturbative series.

Having a look to future perspectives, we actually could think of many possible and interesting physics scenarios that can be explored through ECHO-QGP. Here we collect some of them:

- It would be interesting to extend the calculation of the vorticity in order to see how it scales with different centralities and collision energies, and how it affects observables. The directed flow could indeed be another precious constraint for the hydrodynamical modeling of the plasma. It would be also important to perform a more detailed study, including initial state fluctuations, in order to determine the best conditions for vorticity formation in relativistic nuclear collisions.

- The results discussed in chapter 4 offer a motivation for a more formal and thorough development of this kind of perturbation theory, since it is still unclear whether all initial perturbations in hydrodynamic fields follow a similar pattern. In particular, from general fluid dynamic considerations one may expect that non-linear terms are more important for vorticity excitations [153].

  Another open question concerns the freeze-out from hydrodynamic fields to particle spectra. A mode-by-mode treatment of fluid dynamic perturbations to linear order was discussed recently [154], however it was found that non-linear corrections arise there as well. It would be interesting to see how large these non-linearities are, studying the relation between the initial stage and the post-freeze-out stage, and to test scaling laws such as the one proposed in [155], where $v_4 \propto (v_2)^2$ was conjectured.

- The study of higher flow-harmonics and of event-by-event flow measurements of the particle spectra will provide a rich information on the initial state and on the transport coefficients of the medium. Equally interesting will be the application of ECHO-QGP to the case of high-multiplicity p-A collisions, for which recent theoretical [43, 156] and experimental analyses [157, 158] suggest the possibility of formation of a medium with a collective behavior.

- As a further item to address, we would like to include in ECHO-QGP the possibility of dealing with a finite-density EoS (with possibly a first-order phase transition) [159], including the evolution of the baryon density[2], to have a tool able to dynamically explore scarcely known areas of the QGP phase diagram and to provide predictions of interest for the heavy-ion program foreseen at FAIR and NICA.

- It is also our intention to recover in ECHO-QGP the possibility of evolving electric and magnetic fields, either assuming the validity of the ideal MHD approximation [86], or including magnetic dissipation with the resistive term in the Ohm law [45]. The motivation of such studies is that the presence of a strong magnetic field in ultrarelativistic nucleus-nucleus collisions, which in principle could be much higher than the one inferred in *magnetars* ($\sim 10^{11}$ Tesla), is supposed to produce a sizeable separation of positive and negative

[2]ECHO-QGP already solves the evolution equation for the conserved current in the ideal case, and accepts complete EoSs, but particle diffusion flux is still not taken into account.

charges with respect to the reaction plane [160, 161]). Such a tool would be unique among codes for QGP, and it would represent a very promising cross-fertilization opportunity between the astrophysical and high-energy physics communities.

Appendices

A

Initial conditions for the angular momentum

The calculation of the total angular momentum of the plasma can be done provided that initial conditions are such that energy density falls off rapidly at large $|\eta_s|$. This condition, which is met by the profile in eq. (3.20), indeed implies that a boundary exists where the angular momentum density tensor (that is the integrand below) vanishes and the following integral is conserved:

$$J^{\mu\nu} = \int_\Sigma \mathrm{d}\Sigma_\lambda \, (x^\mu T^{\lambda\nu} - x^\nu T^{\lambda\mu}) \tag{A.1}$$

where Σ is *any* spacelike hypersurface extending over the region where the angular momentum density vanishes. The obvious choice for Bjorken-type initial conditions is the hypersurface $\tau = \tau_0$.

It should be stressed that a vector (or tensor) integral is meaningful in flat spacetime only if the components are the cartesian ones. Hence, for the hypersurface $\tau = \tau_0$, the integration variables are conveniently chosen to be the Bjorken ones, but the components of the stress-energy tensor as well as the x vector will be cartesian. Since the only non vanishing component of the angular momentum in our conventional reference frame is J^y, orthogonal to the reaction plane, we can write:

$$J^y = J^{31} = \int_\Sigma \mathrm{d}\Sigma_\lambda \, \left[x^3 T^{\lambda 1} - x^1 T^{\lambda 3}\right]. \tag{A.2}$$

Finding the hypersurface measure $\mathrm{d}\Sigma_\lambda$ in cartesian components, but expressed through Bjorken variable, requires some reasoning. First, one has

to remind that:

$$\mathrm{d}\Sigma_\lambda = \mathrm{d}\Sigma\, n_\lambda \tag{A.3}$$

where n is the unit vector normal to the hypersurface $\tau = \tau_0$ which is readily found to be (cartesian covariant components):

$$n_\mu = (\cosh\eta, 0, 0, -\sinh\eta_s) \tag{A.4}$$

Now, since Bjorken coordinates are time-orthogonal ($g_{\tau i} = 0$) and with $g_{\tau\tau} = 1$, the invariant spacetime measure $\mathrm{d}\Omega$ can be factorized into the product of the infinitesimal "time" $\mathrm{d}\tau$ and the infinitesimal measure of the orthogonal hypersurface $\mathrm{d}\Sigma$:

$$\mathrm{d}\Omega = \mathrm{d}\tau\, \mathrm{d}\Sigma$$

At the same time:

$$\mathrm{d}\Omega = \sqrt{|g|}\mathrm{d}\tau\, \mathrm{d}x\, \mathrm{d}y\, \mathrm{d}\eta_s = \tau\, \mathrm{d}\tau\, \mathrm{d}x\, \mathrm{d}y\, \mathrm{d}\eta_s$$

whence:

$$\mathrm{d}\Sigma = \tau\, \mathrm{d}x\, \mathrm{d}y\, \mathrm{d}\eta_s. \tag{A.5}$$

Using eqs. (A.3), (A.4) and (A.5), eq. (A.2) can be written as:

$$J^y = \tau \int \mathrm{d}x\, \mathrm{d}y\, \mathrm{d}\eta_s \ \left[\cosh\eta_s (x^3 T^{01} - x^1 T^{03}) - \sinh\eta_s (x^3 T^{31} - x^1 T^{33})\right] \tag{A.6}$$

At the time $\tau = \tau_0$, the stress-energy tensor is supposedly the ideal one and there is no transverse velocity, so that:

$$\begin{aligned} T^{01} &= 0 & T^{33} &= (\varepsilon + p) u^z u^z + p \\ T^{31} &= 0 & T^{03} &= (\varepsilon + p) u^0 u^z \end{aligned} \tag{A.7}$$

Pluggin these expressions into the (A.6) along with the transformation equation:

$$t = \tau\cosh\eta_s \qquad x = x \qquad y = y \qquad z = \tau\sinh\eta_s \tag{A.8}$$

one finally gets:

$$J^y = \tau_0 \int \mathrm{d}x\, \mathrm{d}y\, \mathrm{d}\eta_s\; x\{-\cosh\eta_s\,(\varepsilon+p)u^0u^z + \sinh\eta_s\,[(\varepsilon+p)u^zu^z+p)]\} \tag{A.9}$$

where:

$$\begin{aligned} u^0 &= \cosh\eta_s\; u^\tau + \tau\sinh\eta_s\; u^\eta \\ u^z &= \sinh\eta_s\; u^\tau + \tau\cosh\eta_s\; u^\eta \end{aligned} \tag{A.10}$$

being $u^\tau = \sqrt{1+\tau^2u^{\eta 2}}$.

In the case of Bjorken initial conditions with $u^\eta = 0$ and $u^\tau = 1$, the eq. (A.9) reduces to:

$$J^y = -\tau_0 \int \mathrm{d}x\, \mathrm{d}y\, \mathrm{d}\eta_s\; \varepsilon(x,y,\eta_s)\, x\, \sinh\eta_s \tag{A.11}$$

Bibliography

[1] K. Fukushima and T. Hatsuda, *Rept.Prog.Phys.* **74**, 014001 (2011).

[2] Y. Aoki, G. Endrodi, Z. Fodor, S. Katz, and K. Szabo, *Nature* **443**, 675 (2006).

[3] C. Allton, S. Ejiri, S. Hands, O. Kaczmarek, F. Karsch, et al., *Phys.Rev.* **D68**, 014507 (2003).

[4] U. W. Heinz, *J.Phys.Conf.Ser.* **455**, 012044 (2013).

[5] J.-Y. Ollitrault, *J.Phys.Conf.Ser.* **312**, 012002 (2011).

[6] U. Heinz and R. Snellings, *Ann.Rev.Nucl.Part.Sci.* **63**, 123 (2013).

[7] E. Fermi, *Prog.Theor.Phys.* **5**, 570 (1950).

[8] J. Blaizot and E. Iancu, QCD Perspectives on Hot and Dense Matter, NATO science series. Series II, Mathematics, physics and chemistry, Springer, 2002.

[9] A. Monnai, *Relativistic Dissipative Hydrodynamic Description of the Quark-Gluon Plasma*, PhD thesis, 2014.

[10] S. Nagamiya, M. Lemaire, E. Moller, S. Schnetzer, G. Shapiro, et al., *Phys.Rev.* **C24**, 971 (1981).

[11] J. Bjorken, *Phys.Rev.* **D27**, 140 (1983).

[12] G. Baym, B. Friman, J. Blaizot, M. Soyeur, and W. Czyz, *Nucl.Phys.* **A407**, 541 (1983).

[13] P. F. Kolb, J. Sollfrank, and U. W. Heinz, *Phys.Rev.* **C62**, 054909 (2000).

[14] P. F. Kolb and R. Rapp, *Phys.Rev.* **C67**, 044903 (2003).

[15] H. Gustafsson, H. Gutbrod, B. Kolb, H. Lohner, B. Ludewigt, et al., *Phys.Rev.Lett.* **52**, 1590 (1984).

[16] H. Appelshauser et al., *Phys.Rev.Lett.* **80**, 4136 (1998).

[17] P. Huovinen, P. Kolb, U. W. Heinz, P. Ruuskanen, and S. Voloshin, *Phys.Lett.* **B503**, 58 (2001).

[18] P. Kolb, P. Huovinen, U. W. Heinz, and H. Heiselberg, *Phys.Lett.* **B500**, 232 (2001).

[19] S. Soff, S. A. Bass, M. Bleicher, H. Stoecker, and W. Greiner, (1999).

[20] M. Bleicher and H. Stoecker, *Phys.Lett.* **B526**, 309 (2002).

[21] P. F. Kolb, L.-W. Chen, V. Greco, and C. M. Ko, *Phys.Rev.* **C69**, 051901 (2004).

[22] I. Bearden et al., *Phys.Rev.Lett.* **93**, 102301 (2004).

[23] P. F. Kolb and U. W. Heinz, (2003).

[24] U. W. Heinz and P. F. Kolb, *Nucl.Phys.* **A702**, 269 (2002).

[25] M. Gyulassy, p. 159 (2004).

[26] J. Adams et al., *Nucl.Phys.* **A757**, 102 (2005).

[27] P. Huovinen, *Nucl.Phys.* **A761**, 296 (2005).

[28] T. Hirano and K. Tsuda, *Phys.Rev.* **C66**, 054905 (2002).

[29] S. A. Bass and A. Dumitru, *Physical Review C* **61**, 55 (2000).

[30] D. Teaney, J. Lauret, and E. Shuryak, A Hydrodynamic description of heavy ion collisions at the SPS and RHIC, 2001.

[31] T. Hirano, U. W. Heinz, D. Kharzeev, R. Lacey, and Y. Nara, *Phys.Lett.* **B636**, 299 (2006).

[32] H. Song, S. A. Bass, and U. Heinz, *Phys.Rev.* **C83**, 024912 (2011).

[33] R. A. Lacey and A. Taranenko, *PoS* **CFRNC2006**, 021 (2006).

[34] M. Luzum and P. Romatschke, *Phys.Rev.* **C78**, 034915 (2008).

[35] P. Romatschke and U. Romatschke, *Phys.Rev.Lett.* **99**, 172301 (2007).

[36] M. Luzum and P. Romatschke, *Phys.Rev.Lett.* **103**, 262302 (2009).

[37] I. Karpenko, P. Huovinen, and M. Bleicher, *Comput.Phys.Commun.* **185**, 3016 (2014).

[38] C. Gale, S. Jeon, B. Schenke, P. Tribedy, and R. Venugopalan, *Phys.Rev.Lett.* **110**, 012302 (2013).

[39] J. Vredevoogd and S. Pratt, *Phys.Rev.* **C85**, 044908 (2012).

[40] P. Bozek and W. Broniowski, *Phys.Rev.Lett.* **109**, 062301 (2012).

[41] C. Nonaka and M. Asakawa, *PTEP* **2012**, 01A208 (2012).

[42] S. Ryu, S. Jeon, C. Gale, B. Schenke, and C. Young, *Nucl.Phys.* **A904-905**, 389c (2013).

[43] I. Kozlov, M. Luzum, G. Denicol, S. Jeon, and C. Gale, (2014).

[44] U. Heinz, P. Sorensen, A. Deshpande, C. Gagliardi, F. Karsch, et al., Exploring the properties of the phases of QCD matter - research opportunities and priorities for the next decade, 2015.

[45] N. Bucciantini and L. Del Zanna, *Monthly Notices of the Royal Astronomical Society* **428**, 71 (2013).

[46] J.-Y. Ollitrault and F. G. Gardim, *Nucl.Phys.* **A904-905**, 75c (2013).

[47] K. Dusling and T. Schäfer, *Phys.Rev.* **C85**, 044909 (2012).

[48] B. Schenke, S. Jeon, and C. Gale, *Phys.Rev.Lett.* **106**, 042301 (2011).

[49] B. Schenke, S. Jeon, and C. Gale, *Phys.Rev.* **C82**, 014903 (2010).

[50] R. Derradi de Souza, J. Takahashi, T. Kodama, and P. Sorensen, *Phys.Rev.* **C85**, 054909 (2012).

[51] Y.-L. Yan, Y. Cheng, D.-M. Zhou, B.-G. Dong, X. Cai, et al., *J.Phys.* **G40**, 025102 (2013).

[52] A. Chaudhuri, *Phys.Lett.* **B713**, 91 (2012).

[53] H. Petersen, R. La Placa, and S. A. Bass, *J.Phys.* **G39**, 055102 (2012).

[54] C. Shen and U. Heinz, *Phys.Rev.* **C85**, 054902 (2012).

[55] F. G. Gardim, F. Grassi, M. Luzum, and J.-Y. Ollitrault, *Phys.Rev.* **C85**, 024908 (2012).

[56] E. Retinskaya, M. Luzum, and J.-Y. Ollitrault, *Phys.Rev.Lett.* **108**, 252302 (2012).

[57] R. Ryblewski and W. Florkowski, *Phys.Rev.* **C85**, 064901 (2012).

[58] T. Hirano, P. Huovinen, K. Murase, and Y. Nara, *Prog.Part.Nucl.Phys.* **70**, 108 (2013).

[59] L. Pang, Q. Wang, and X.-N. Wang, *Phys.Rev.* **C86**, 024911 (2012).

[60] D. Teaney and L. Yan, *Phys.Rev.* **C86**, 044908 (2012).

[61] H. Holopainen and P. Huovinen, *J.Phys.Conf.Ser.* **389**, 012018 (2012).

[62] H. Niemi, G. Denicol, H. Holopainen, and P. Huovinen, *Phys.Rev.* **C87**, 054901 (2013).

[63] R. Soltz, I. Garishvili, M. Cheng, B. Abelev, A. Glenn, et al., *Phys.Rev.* **C87**, 044901 (2013).

[64] Z. Qiu and U. Heinz, *Phys.Lett.* **B717**, 261 (2012).

[65] M. Luzum and J.-Y. Ollitrault, *Nucl.Phys.* **A904-905**, 377c (2013).

[66] H. Song, *Eur.Phys.J.* **A48**, 163 (2012).

[67] P. Huovinen and D. Molnar, *Phys.Rev.* **C79**, 014906 (2009).

[68] G. S. Denicol, U. W. Heinz, M. Martinez, J. Noronha, and M. Strickland, *Phys.Rev.* **D90**, 125026 (2014).

[69] P. Romatschke, *Int.J.Mod.Phys.* **E19**, 1 (2010).

[70] G. Denicol, H. Niemi, E. Molnar, and D. Rischke, *Phys.Rev.* **D85**, 114047 (2012).

[71] E. Molnár, H. Niemi, G. Denicol, and D. Rischke, *Phys.Rev.* **D89**, 074010 (2014).

[72] W. Israel and J. Stewart, *Annals of Physics* **118**, 341 (1979).

[73] H. Grad, *Communications on Pure and Applied Mathematics* **2**, 331 (1949).

[74] H. J. Müller, *Z. f. Phys.* **198**, 59 (1967).

[75] J. Stewart, Non-equilibrium relativistic kinetic theory, in *Non-Equilibrium Relativistic Kinetic Theory*, volume 10 of *Lecture Notes in Physics*, pp. 1–113, Springer Berlin Heidelberg, 1971.

[76] J. L. Anderson, *Relativity, Plenum Pr.* , 109 (1970).

[77] C. Marle, *Ann. Inst. H. Poicarè* **10**, 127 (1969).

[78] M. Kraniš, *Phys.Lett. A* **33**, 77 (1970).

[79] M. Kraniš, *Nuovo Cimento B* **8** (1972).

[80] M. Kraniš, *Arch. Rational Mech. Anal.* **48**, 274 (1972).

[81] M. Kraniš, *Ann. Inst. H. Poicarè Sect. A* **25**, 197 (1976).

[82] P. Romatschke, *Class.Quant.Grav.* **27**, 025006 (2010).

[83] E. Molnar, H. Niemi, and D. Rischke, *Eur.Phys.J.* **C65**, 615 (2010).

[84] J. Noronha-Hostler, G. S. Denicol, J. Noronha, R. P. G. Andrade, and F. Grassi, *Phys.Rev.* **C88**, 044916 (2013).

[85] L. Del Zanna, V. Chandra, G. Inghirami, V. Rolando, A. Beraudo, et al., *Eur.Phys.J.* **C73**, 2524 (2013).

[86] L. Del Zanna, O. Zanotti, N. Bucciantini, and P. Londrillo, *Astron.Astrophys.* **473**, 11 (2007).

[87] *J. Comput. Phys.* **71** (1987).

[88] M. Takamoto and S. Inutsuka, *J. Comput. Phys.* **230**, 7002 (2011).

[89] A. Muronga, *Phys.Rev.Lett.* **88**, 062302 (2002).

[90] R. Baier, P. Romatschke, D. T. Son, A. O. Starinets, and M. A. Stephanov, *JHEP* **0804**, 100 (2008).

[91] B. K. Patra, V. Agotiya, and V. Chandra, *Eur.Phys.J.* **C67**, 465 (2010).

[92] S. S. Gubser, *Phys.Rev.* **D82**, 085027 (2010).

[93] G. S. Denicol, U. W. Heinz, M. Martinez, J. Noronha, and M. Strickland, *Phys.Rev.Lett.* **113**, 202301 (2014).

[94] H. Marrochio, J. Noronha, G. S. Denicol, M. Luzum, S. Jeon, et al., (2013).

[95] S. S. Gubser and A. Yarom, *Nucl.Phys.* **B846**, 469 (2011).

[96] A. Jaiswal, *Phys.Rev.* **C87**, 051901 (2013).

[97] A. Jaiswal, *Phys.Rev.* **C88**, 021903 (2013).

[98] W. Florkowski, *Phenomenology of Ultra-relativistic Heavy-ion Collisions*, World Scientific, 2010.

[99] H. De Vries, C. De Jager, and C. De Vries, *Atom.Data Nucl.Data Tabl.* **36**, 495 (1987).

[100] A. Adil and M. Gyulassy, *Phys.Rev.* **C72**, 034907 (2005).

[101] H. Holopainen, H. Niemi, and K. J. Eskola, *Phys.Rev.* **C83**, 034901 (2011).

[102] M. Laine and Y. Schroder, *Phys.Rev.* **D73**, 085009 (2006).

[103] S. Borsanyi, G. Endrodi, Z. Fodor, A. Jakovac, S. D. Katz, et al., *JHEP* **1011**, 077 (2010).

[104] F. Cooper and G. Frye, *Phys.Rev.* **D10**, 186 (1974).

[105] J. Sollfrank, P. Koch, and U. W. Heinz, *Phys.Lett.* **B252**, 256 (1990).

[106] J. Sollfrank, P. Koch, and U. W. Heinz, *Z.Phys.* **C52**, 593 (1991).

[107] C. Nonaka and S. A. Bass, *Phys.Rev.* **C75**, 014902 (2007).

[108] H. Petersen, J. Steinheimer, G. Burau, M. Bleicher, and H. Stocker, *Phys.Rev.* **C78**, 044901 (2008).

[109] K. Werner, I. Karpenko, T. Pierog, M. Bleicher, and K. Mikhailov, *Phys.Rev.* **C82**, 044904 (2010).

[110] H. Song, S. A. Bass, U. Heinz, T. Hirano, and C. Shen, *Phys.Rev.Lett.* **106**, 192301 (2011).

[111] I. Karpenko, Y. Sinyukov, and K. Werner, *Phys.Rev.* **C87**, 024914 (2013).

[112] P. Huovinen and H. Petersen, *Eur.Phys.J.* **A48**, 171 (2012).

[113] K. Dusling and D. Teaney, *Phys.Rev.* **C77**, 034905 (2008).

[114] P. Romatschke, *Eur.Phys.J.* **C52**, 203 (2007).

[115] H. Song and U. W. Heinz, *Phys.Rev.* **C78**, 024902 (2008).

[116] D. Molnar and P. Huovinen, *J.Phys.* **G35**, 104125 (2008).

[117] R. Baier and P. Romatschke, *Eur.Phys.J.* **C51**, 677 (2007).

[118] P. Kolb, U. W. Heinz, P. Huovinen, K. Eskola, and K. Tuominen, *Nucl.Phys.* **A696**, 197 (2001).

[119] P. F. Kolb, J. Sollfrank, and U. W. Heinz, *Phys.Lett.* **B459**, 667 (1999).

[120] F. Becattini, F. Piccinini, and J. Rizzo, *Phys.Rev.* **C77**, 024906 (2008).

[121] L. Csernai, V. Magas, and D. Wang, *Phys.Rev.* **C87**, 034906 (2013).

[122] L. Csernai, D. Wang, M. Bleicher, and H. Stöcker, *Phys.Rev.* **C90**, 021904 (2014).

[123] D. E. Kharzeev and D. T. Son, *Phys.Rev.Lett.* **106**, 062301 (2011).

[124] F. Becattini, V. Chandra, L. Del Zanna, and E. Grossi, *Annals Phys.* **338**, 32 (2013).

[125] F. Becattini, L. Csernai, and D. Wang, *Phys.Rev.* **C88**, 034905 (2013).

[126] F. Becattini, G. Inghirami, V. Rolando, A. Beraudo, L. Del Zanna, et al., A study of vorticity formation in high energy nuclear collisions, 2015.

[127] E. Gourgoulhon, *EAS Publ.Ser.* **21**, 43 (2006).

[128] M. Stephanov and Y. Yin, (2014).

[129] F. Becattini, L. Bucciantini, E. Grossi, and L. Tinti, Local thermodynamical equilibrium and the beta frame for a quantum relativistic fluid, 2014.

[130] F. Becattini, *Phys.Rev.Lett.* **108**, 244502 (2012).

[131] P. Bozek and I. Wyskiel, *Phys.Rev.* **C81**, 054902 (2010).

[132] H. Song and U. W. Heinz, *Phys.Rev.* **C77**, 064901 (2008).

[133] M. L. Miller, K. Reygers, S. J. Sanders, and P. Steinberg, *Ann.Rev.Nucl.Part.Sci.* **57**, 205 (2007).

[134] B. Abelev et al., *Phys.Rev.Lett.* **101**, 252301 (2008).

[135] V. Rolando, G. Inghirami, A. Beraudo, L. Del Zanna, F. Becattini, et al., *Nucl.Phys.* **A** (2014).

[136] V. Rolando, *J.Phys.Conf.Ser.* **527**, 012017 (2014).

[137] R. J. LeVeque, *Numerical Methods for Conservation Laws*, Lectures in Mathematics, ETH Zürich, Springer, 1992.

[138] C. Gale, S. Jeon, and B. Schenke, *Int.J.Mod.Phys.* **A28**, 1340011 (2013).

[139] B. Hippolyte and D. H. Rischke, *Nucl.Phys.* **A904-905**, 318c (2013).

[140] D. A. Teaney, Viscous Hydrodynamics and the Quark Gluon Plasma, 2009.

[141] Z. Qiu and U. W. Heinz, *Phys.Rev.* **C84**, 024911 (2011).

[142] B. Schenke, S. Jeon, and C. Gale, *Phys.Rev.* **C85**, 024901 (2012).

[143] R. S. Bhalerao, M. Luzum, and J.-Y. Ollitrault, *Phys.Rev.* **C84**, 034910 (2011).

[144] B. Schenke, P. Tribedy, and R. Venugopalan, *Phys.Rev.Lett.* **108**, 252301 (2012).

[145] D. Teaney and L. Yan, *Phys.Rev.* **C83**, 064904 (2011).

[146] W. L. Qian, P. Mota, R. Andrade, F. Gardim, F. Grassi, et al., *J.Phys.* **G41**, 015103 (2013).

[147] W. Deng, Z. Xu, and C. Greiner, *Phys.Lett.* **B711**, 301 (2012).

[148] S. Floerchinger and U. A. Wiedemann, *Phys.Lett.* **B728**, 407 (2014).

[149] S. Floerchinger and U. A. Wiedemann, *Phys.Rev.* **C88**, 044906 (2013).

[150] Z. Qiu, C. Shen, and U. Heinz, *Phys.Lett.* **B707**, 151 (2012).

[151] M. Bluhm, P. Alba, W. Alberico, A. Beraudo, and C. Ratti, *Nucl.Phys.* **A929**, 157 (2014).

[152] Oscar repository: https://karman.physics.purdue.edu/OSCAR/index.php/Codes.

[153] S. Floerchinger and U. A. Wiedemann, *JHEP* **1111**, 100 (2011).

[154] S. Floerchinger and U. A. Wiedemann, *Phys.Rev.* **C89**, 034914 (2014).

[155] N. Borghini and J.-Y. Ollitrault, *Phys.Lett.* **B642**, 227 (2006).

[156] P. Bozek, *Phys.Rev.* **C85**, 014911 (2012).

[157] G. Aad et al., *Phys.Rev.Lett.* **110**, 182302 (2013).

[158] S. Chatrchyan et al., *Phys.Lett.* **B718**, 795 (2013).

[159] I. Karpenko, M. Bleicher, P. Huovinen, and H. Petersen, *J.Phys.Conf.Ser.* **503**, 012040 (2014).

[160] D. E. Kharzeev, L. D. McLerran, and H. J. Warringa, *Nucl.Phys.* **A803**, 227 (2008).

[161] D. E. Kharzeev and H.-U. Yee, *Phys.Rev.* **D84**, 045025 (2011).

Thanks